

University of Thessaly  
School of Engineering  
Department of Mechanical Engineering

**Simulation and design  
of the homogenization process  
of 6xxx extrudable Aluminum alloys**

*Development of design rules for high extrudability*

*by*

Panagiota I. Sarafoglou  
Dipl. Chemical Engineering, NTUA  
M.Sc. Materials, NTUA

Submitted  
*in partial fulfilment of the requirements of the degree of*  
DOCTOR OF PHILOSOPHY

Supervisor  
Professor Gregory N. Haidemenopoulos

Volos 2016



# Thesis examination committee

---

- |    |                             |   |
|----|-----------------------------|---|
| 1. | Prof. G. N. Haidemenopoulos | University of Thessaly<br><i>Department of Mechanical Engineering</i><br><b>(Thesis advisor)</b>          |
| 2. | Prof. N. Aravas             | University of Thessaly<br><i>Department of Mechanical Engineering</i>                                     |
| 3. | Prof. D. Manolakos          | National Technical University of Athens<br><i>School of Mechanical Engineering</i>                        |
| 4. | Prof. S. Pantelakis         | University of Patras<br><i>Department of Mechanical Engineering<br/>and Aeronautics</i>                   |
| 5. | Prof. D. I. Pantelis        | National Technical University of Athens<br><i>School of Naval Architecture and Marine<br/>Engineering</i> |
| 6. | Prof. E. Pavlatou           | National Technical University of Athens<br><i>School of Chemical Engineering</i>                          |
| 7. | Prof. A. Zavaliangos        | Drexel University<br>Department of Materials Science and<br>Engineering                                   |



# Simulation and design of the homogenization process of 6xxx extrudable Aluminum alloys

## Development of design rules for high extrudability

### Abstract

---

New demanding light-weight applications in the automotive and aircraft sectors require the development of high-strength Al-alloy extrusions based on the Al-Mg-Si system (6xxx series). The increase of strength is possible with higher alloying with Mg and Si, in order to form higher amounts of the strengthening phase  $Mg_2Si$  (e.g. 6061 and 6082 alloys). However increased alloying deteriorates the extrudability, leading to extremely low extrusion speeds for the high-strength alloy systems. In the other end of the spectrum, i.e. low-alloy low-strength applications (e.g. 6060 or 6063 alloys), the main industrial requirement is to increase the extrusion speed, in order to increase production rates. In both cases, it appears that extrudability is the key property that should be controlled and improved through a carefully designed homogenization process. So far the problem has been tackled in a rather empirical way, involving intense trial-and-error laboratory or even industrial experiments to figure out the effect of alloy chemistry and homogenization process parameters such as the homogenization temperature and time and the cooling rate following homogenization. In most cases only individual aspects of the process are considered and the effect of prior processing is often neglected.

The design of new high-strength or high extrudability 6xxx alloys calls for an integrated approach considering all parts of the process chain and their effect on extrudability. The aim of this doctoral thesis has been to apply a simulation-based approach, validated by relevant experimental data, in order to describe the effect of alloy chemistry and homogenization process conditions on the material microstructure prior to extrusion. In this way it was possible to shape design rules (in terms of composition and processing) for the development of either high-strength or high extrudability alloys.

Computational alloy thermodynamics and kinetics were applied to predict the rate of phase transformations, which shape the microstructure across the process chain. This approach is extremely powerful and was used to simulate a wide range of different phenomena such as solidification and microsegregation during casting, dissolution of  $Mg_2Si$ , removal of microsegregation and transformation of iron intermetallics during homogenization and finally re-precipitation during cooling from the homogenization temperature.

More specifically computational alloy thermodynamics, based on the CALPHAD approach, has been applied to perform Scheil-Gulliver solidification simulations. The resulting microsegregation of elements and phases in the as-cast microstructure were calculated as a function of alloy composition. The results of the simulations were confirmed experimentally by quantitative image analysis for the measurement of phase fractions. The variation of the mole fractions of the extrudability-limiting  $\beta-AlFeSi$  phase and the strengthening  $Mg_2Si$  phase with alloying elements has been mapped over the useful range (0-1.2 mass%) in the Mg-Si composition space. The constructed maps indicate that low mole fractions of  $\beta-AlFeSi$  are associated with lower Si and higher Mg compositions. On the other hand, high mole fractions of  $Mg_2Si$  are associated with both higher Si and Mg compositions, with Mg possessing a stronger

effect. Construction of maps for different levels of Mn has shown that addition of Mn could allow for higher alloying with Mg and Si, in order to obtain higher amount of  $\text{Mg}_2\text{Si}$ , without at the same time increasing the  $\beta\text{-AlFeSi}$  intermetallic phase in the as-cast microstructure.

The Dual grain model (DGM) has been developed to treat the homogenization process in multicomponent and multiphase Al-alloys exhibiting a large variability of the as-cast grain size. With the model it has been possible to simulate the temporal and spatial evolution of phase fractions and element concentrations during homogenization. Regarding the evolution of phase fractions during homogenization, the predictions of the DGM model have been validated experimentally with XRD analysis. The evolution of the  $\beta\text{-AlFeSi} \rightarrow \alpha\text{-AlFeSi}$  transformation is predicted by the DGM and is confirmed by XRD in the same time scale. The DGM predictions regarding the evolution of Fe and Mg concentrations with homogenization time are in excellent agreement. There are only some discrepancies in the profiles of Si and Mn. The DGM predicts the fast dissolution of  $\text{Mg}_2\text{Si}$  during homogenization and its re-precipitation during cooling. The DGM can describe the temporal and spatial evolution of the  $\beta\text{-AlFeSi} \rightarrow \alpha\text{-AlFeSi}$  transformation. The spatial evolution exhibits an exact spatial correspondence. Both the  $\text{Mg}_2\text{Si}$  dissolution and the  $\beta\text{-AlFeSi} \rightarrow \alpha\text{-AlFeSi}$  transformation are faster in the smaller grain as predicted by the DGM. In addition the concentration profiles of the elements homogenize faster in the smaller grain, indicating that a fine grain size in the as-cast microstructure accelerates the homogenization process. The DGM predicts correctly the effect of homogenization temperature. The rate of both,  $\text{Mg}_2\text{Si}$  dissolution and  $\beta\text{-AlFeSi} \rightarrow \alpha\text{-AlFeSi}$  transformation increase with the homogenization temperature. A preliminary attempt to develop homogenization process maps has been performed using the DGM. These maps are, at present, based on the  $\beta\text{-AlFeSi} \rightarrow \alpha\text{-AlFeSi}$  transformation and can be used for the design of the homogenization heat treatment. The quantification of the homogenization state was achieved by determine specific microstructural indices, such as the aspect ratio and the circularity of the intermetallic phases. In this way it was possible to quantify the shape evolution of the intermetallic compounds during homogenization.

Precipitation during cooling from the homogenization temperature was simulated with the Kampman-Wagner Numerical (KWN) precipitation model. The relevant particle size distribution (PSD), evolution of volume fraction and particle size during cooling was calculated. The results were introduced in a suitable strength model to calculate the resulting hardness. The simulation results are in satisfactory agreement with experimental data. The hardness of the homogenized billets was investigated experimentally. Regarding the effect of homogenization cooling rate, water quenching results in higher hardness relative to air cooling and forced air cooling. The hardness difference increases with alloying in the order  $6063 \rightarrow 6005 \rightarrow 6082$ . The effect is attributed to the higher amounts of Mg and Si retained in solid solution during cooling. The effect of excess Si on the precipitation of  $\beta'\text{-Mg}_2\text{Si}$  was determined using the KWN precipitation model. The resulting shift in the continuous cooling precipitation (CCP) diagram was calculated. This allows the design of a suitable cooling program in order to avoid the precipitation of  $\beta\text{-Mg}_2\text{Si}$  and allow the precipitation of  $\beta'\text{-Mg}_2\text{Si}$ . This allows the use of a lower preheating temperature prior to extrusion and leads to the use of higher press loads in order to obtain higher extrusion speeds.

Specific design rules were formulated, regarding the as-cast microstructure, the homogenization temperature and time as well as the cooling from the homogenization temperature in order to obtain high extrudability. The microstructure developed during DC casting is affected by the solidification conditions. Grain size and dendrite arm spacing (DAS) are

the most important factors. They can be controlled by the casting speed (solidification rate) and seeding for grain refining. A smaller grain size and DAS improves the strength and also shortens the diffusion distances, leading to a more efficient homogenization for a given homogenization cycle. Phase fraction mapping, developed in this thesis, can be used for the selection of alloy compositions to minimize the undesirable  $\beta$ -AlFeSi intermetallic in the as-cast microstructure, in order to achieve a good starting point for the homogenization to follow. In addition, it has been shown that Mn reduces the amount of  $\beta$ -AlFeSi for a given Mg-Si-Fe combination. With the DGM model developed in this thesis, it is possible to determine the required time for  $\text{Mg}_2\text{Si}$  dissolution and the transformation  $\beta \rightarrow \alpha$ -AlFeSi as a function of homogenization temperature and alloy composition. The DGM model also indicated that a small as-cast grain size accelerates the kinetics of homogenization. Microstructural indices, such as the aspect ratio and the circularity can be used to characterize the homogenization stage quantitatively. A fully homogenized billet, with the potential for high extrudability should have all  $\beta$ -AlFeSi transformed to  $\alpha$ -AlFeSi, with necklace morphology and with aspect ratio and circularity approaching unity. In addition all  $\text{Mg}_2\text{Si}$  should be dissolved and Mg and Si should be distributed as uniformly as possible in the grain interiors. The cooling from the homogenization temperature should be designed so that precipitation of  $\beta$ - $\text{Mg}_2\text{Si}$  is avoided and only precipitation of  $\beta'$ - $\text{Mg}_2\text{Si}$  takes place. A CCP diagram like the one developed in this thesis for a 6060 alloy can be used to design the cooling cycle. Finally it is important to match the preheating conditions to the homogenization cooling conditions in order to get the most benefit of homogenization.  $\beta$ - $\text{Mg}_2\text{Si}$  precipitates require higher temperatures to dissolve (higher solvus) and have a detrimental effect on hot ductility. On the other hand the  $\beta'$ - $\text{Mg}_2\text{Si}$  ppts, are finer, semi – coherent with the matrix and have a lower solvus temperature. Thus a lower preheating temperature can be employed in combination with a high extrusion speed. This will raise the exit temperature from the extrusion press to a value sufficient for complete dissolution of  $\text{Mg}_2\text{Si}$ .

The integrated simulation of microsegregation during casting, dissolution of  $\text{Mg}_2\text{Si}$  and transformation of iron intermetallics during homogenization as well as re-precipitation of  $\text{Mg}_2\text{Si}$  during homogenization cooling, enables the computer-aided development of new alloys and the design of the associated homogenization treatments for high extrudability at a fraction of time and cost associated with empirical development.





# Προσομοίωση και σχεδιασμός της κατεργασίας ομογενοποίησης σε διελάσιμα κράματα αλουμινίου της σειράς 6xxx. Διαμόρφωση κανόνων σχεδιασμού για υψηλή διελασιμότητα Περίληψη

---

Οι σύγχρονες ελαφρές κατασκευές τόσο στην αυτοκινητοβιομηχανία όσο και την αεροπορική βιομηχανία απαιτούν την ανάπτυξη διελάσιμων κραμάτων αλουμινίου υψηλής αντοχής με βάση το σύστημα Al-Mg-Si (σειρά 6xxx). Η αύξηση της αντοχής είναι δυνατή με την αύξηση του επιπέδου κραμάτωσης σε Mg και Si, ώστε να σχηματιστεί μεγαλύτερο ποσοστό από τη φάση ισχυροποίησης  $Mg_2Si$  (π.χ στα κράματα 6061 και 6082). Ωστόσο η αυξημένη κραμάτωση προκαλεί υποβάθμιση της διελασιμότητας και οδηγεί σε εξαιρετικά χαμηλές ταχύτητες διέλασης στα κράματα αυτά. Στην άλλη μεριά του φάσματος, δηλαδή σε εφαρμογές όπου απαιτείται χαμηλή αντοχή (π.χ. κράματα 6060 και 6063), η βασική βιομηχανική απαίτηση είναι η αύξηση της ταχύτητας διέλασης, η οποία με τη σειρά της οδηγεί σε αύξηση της παραγωγικότητας. Και στις δύο περιπτώσεις φαίνεται ότι η διελασιμότητα αποτελεί την «ιδιότητα-κλειδί» που πρέπει να ελεγχθεί και να βελτιωθεί μέσω ενός προσεκτικού σχεδιασμού της κατεργασίας ομογενοποίησης. Μέχρι τώρα το πρόβλημα αυτό έχει αντιμετωπιστεί περισσότερο εμπειρικά, με πειραματικές διαδικασίες σε εργαστηριακή αλλά και σε βιομηχανική κλίμακα, σε μία προσπάθεια να διερευνηθούν τόσο η επίδραση της χημικής σύστασης όσο και οι συνθήκες της κατεργασίας όπως η θερμοκρασία, ο χρόνος και ο ρυθμός ψύξης της ομογενοποίησης. Στις περισσότερες περιπτώσεις έχουν μελετηθεί μεμονωμένες επιδράσεις ενώ συνήθως δεν μελετάται η επιρροή του ιστορικού των κατεργασιών.

Ο σχεδιασμός νέων κραμάτων της σειράς 6xxx με υψηλή αντοχή ή υψηλή διελασιμότητα απαιτεί την εφαρμογή μιας ολοκληρωμένης μεθοδολογίας, η οποία να περιλαμβάνει όλους τους κρίκους της αλυσίδας κατεργασιών και την επίδρασή τους στη διελασιμότητα.

Ο στόχος της παρούσας Διδακτορικής Διατριβής ήταν η εφαρμογή μιας μεθοδολογίας προσομοίωσης, επικυρωμένης με πειραματικά δεδομένα, για την περιγραφή της επίδρασης της χημικής σύστασης και των συνθηκών ομογενοποίησης στην μικροδομή του κράματος πριν τη διέλαση. Με τον τρόπο αυτό διαμορφώθηκαν κανόνες σχεδιασμού, που αφορούν στη σύσταση και τη κατεργασία, για την ανάπτυξη κραμάτων υψηλής διελασιμότητας.

Οι τεχνικές της υπολογιστικής θερμοδυναμικής και κινητικής κραμάτων εφαρμόστηκαν για την πρόβλεψη της ταχύτητας των μετασχηματισμών των φάσεων, που διαμορφώνουν την μικροδομή κατά μήκος της αλυσίδας κατεργασιών στα διελάσιμα κράματα αλουμινίου. Αυτή η μεθοδολογία είναι πολύ αποτελεσματική και εφαρμόστηκε για την προσομοίωση διεργασιών όπως η στερεοποίηση και η διαμόρφωση του μικροδιαφορισμού κατά τη χύτευση, η απομείωση του μικροδιαφορισμού, η διαλυτοποίηση του  $Mg_2Si$  και ο μετασχηματισμός των ενδομεταλλικών ενώσεων του σιδήρου κατά την ομογενοποίηση αλλά και η επανακαθίζηση του  $Mg_2Si$  κατά την ψύξη από τη θερμοκρασία ομογενοποίησης.

Πιο συγκεκριμένα, η υπολογιστική θερμοδυναμική, βασισμένη στη μεθοδολογία CALPHAD, εφαρμόστηκε για την διενέργεια προσομοιώσεων στερεοποίησης τύπου Scheil-Gulliver. Με το τρόπο αυτό υπολογίστηκε ο μικροδιαφορισμός των στοιχείων και των φάσεων στη χυτή μικροδομή σε συνάρτηση με τη χημική σύσταση του κράματος. Τα αποτελέσματα των

προσομοιώσεων επικυρώθηκαν με πειραματικά δεδομένα ποσοτικής μεταλλογραφίας, που αφορούσαν στη μέτρηση του ποσοστού των φάσεων. Έτσι διαμορφώθηκαν χάρτες που απεικονίζουν τα ποσοστά της φάσης ισχυροποίησης  $Mg_2Si$  και της φάσης που περιορίζει τη διελασιμότητα, την  $\beta-AlFeSi$ , σε συνάρτηση με τα κραματικά στοιχεία Mg και Si. Οι χάρτες αυτοί υποδεικνύουν ότι χαμηλή κραμάτωση σε Si και υψηλή κραμάτωση σε Mg οδηγεί σε χαμηλά ποσοστά της ανεπιθύμητης φάσης  $\beta-AlFeSi$  και ενδεχόμενη αύξηση της διελασιμότητας. Από την άλλη μεριά, υψηλότερη κραμάτωση τόσο σε Mg όσο και σε Si οδηγεί σε υψηλά ποσοστά της φάσης ισχυροποίησης  $Mg_2Si$  και ενδεχόμενη αύξηση της αντοχής. Η κατασκευή των χαρτών για διαφορετικά ποσοστά Mn έδειξε ότι η προσθήκη Mn επιτρέπει την αύξηση της κραμάτωσης σε Mg και Si για την αύξηση της αντοχής, χωρίς την ταυτόχρονη αύξηση της ανεπιθύμητης φάσης  $\beta-AlFeSi$  στη χυτή μικροδομή.

Για την επίλυση του προβλήματος της ομογενοποίησης σε πολυσυστατικά και πολυφασικά κραματικά συστήματα αλουμινίου, που παρουσιάζουν μεγάλη διασπορά στο μέγεθος του κόκκου, ανπτύχθηκε το μοντέλο ομογενοποίησης διπλού κόκκου (Dual Grain Model, DGM). Με το μοντέλο αυτό προσδιορίστηκε τόσο η χρονική όσο και η χωρική εξέλιξη του ποσοστού των διαφορετικών φάσεων της μικροδομής καθώς και του μικροδιαφορισμού κατά τη διάρκεια της ομογενοποίησης. Τα αποτελέσματα των προσομοιώσεων επικυρώθηκαν με αντίστοιχα δεδομένα από πειραματικές τεχνικές XRD και SEM/EDX. Το DGM περιγράφει την χρονική και χωρική εξέλιξη του μετασχηματισμού  $\beta-AlFeSi \rightarrow \alpha-AlFeSi$ . Η χωρική εξέλιξη παρουσιάζει μια ακριβή αντιστοιχία μεταξύ των ποσοστών της  $\alpha$  και  $\beta-AlFeSi$ . Επίσης το DGM προβλέπει την ταυτόχρονη διαλυτοποίηση της φάσης  $Mg_2Si$  και την επανακαθίζησή της κατά τη ψύξη. Όλοι οι μετασχηματισμοί παρουσιάζουν μεγαλύτερες ταχύτητες στο μικρότερο κόκκο του DGM, γεγονός που υποδεικνύει ότι μία εκλέπτυνση του κόκκου της χυτής μικροδομής μπορεί να επιταχύνει την ομογενοποίηση. Επίσης το DGM προβλέπει σωστά την επίδραση της θερμοκρασίας ομογενοποίησης. Οι ταχύτητες τόσο της διαλυτοποίησης του  $Mg_2Si$  όσο και του μετασχηματισμού  $\beta-AlFeSi \rightarrow \alpha-AlFeSi$  αυξάνονται με την αύξηση της θερμοκρασίας. Τέλος πραγματοποιήθηκε μια αρχική προσπάθεια κατασκευής ενός χάρτη ομογενοποίησης (homogenization process map) με τη χρήση του DGM. Ο χάρτης αυτός, προς το παρόν, βασίζεται στο χρόνο περάτωσης του μετασχηματισμού  $\beta-AlFeSi \rightarrow \alpha-AlFeSi$  και μπορεί να χρησιμοποιηθεί για το σχεδιασμό της κατεργασίας ομογενοποίησης. Ταυτόχρονα πραγματοποιήθηκε και η ποσοτικοποίηση της κατάστασης ομογενοποίησης με τον προδιορισμό μεταλλογραφικών δεικτών όπως η αναλογία πλάτους/μήκος και η κυκλικότητα των ενδομεταλλικών ενώσεων. Με τον τρόπο αυτό ποσοτικοποιήθηκε η εξέλιξη της μορφολογίας των ενδομεταλλικών ενώσεων κατά τη διάρκεια της ομογενοποίησης.

Η καθίζηση κατά τη διάρκεια της ψύξης από τη θερμοκρασία ομογενοποίησης προσομοιώθηκε με το μοντέλο Kampman-Wagner-Numerical (KWN). Έτσι προσδιορίστηκε η κατανομή μεγέθους σωματιδίων και η εξέλιξη του κλάσματος όγκου και του μεγέθους των σωματιδίων. Τα αποτελέσματα της προσομοίωσης επιβεβαιώθηκαν από πειραματικές μετρήσεις της σκληρότητας.

Η επίδραση του πρόσθετου Si (Excess Si) στην διαμόρφωση του διαγράμματος καθίζησης υπό συνεχή ψύξη (CCP diagram) που αφορά στη καθίζηση της μετασταθούς φάσης  $\beta'-Mg_2Si$  πραγματοποιήθηκε με το KWN. Αυτό επέτρεψε τον σχεδιασμό ενός προγράμματος ψύξης για την αποφυγή σχηματισμού της φάσης ισορροπίας  $\beta-Mg_2Si$  και τον σχηματισμό της επιθυμητής φάσης  $\beta'-Mg_2Si$ . Αυτό οδηγεί στην εφαρμογή χαμηλότερης θερμοκρασίας προθέρμανσης πριν

τη διέλαση και επιτρέπει την εφαρμογή μεγαλύτερων φορτίων στην πρέσσα διέλασης με σημαντική αύξηση της ταχύτητας διέλασης.

Διαμορφώθηκαν κανόνες σχεδιασμού για την επίτευξη υψηλής διελασιμότητας. Οι κανόνες αυτοί αφορούν στη κραμάτωση, τη χυτή μικροδομή, την ομογενοποίηση και την ψύξη ομογενοποίησης. Μικρότερο μέγεθος κόκκου στη χυτή μικροδομή επιτρέπει την αύξηση της κινητικής κατά την ομογενοποίηση οδηγώντας σε μικρότερους χρόνους ομογενοποίησης. Το μέγεθος του κόκκου μπορεί να ελεγχθεί μέσω της ταχύτητας στερεοποίησης και του εμβολιασμού του υγρού μετάλλου για ετερογενή πυρήνωση κατά τη στερεοποίηση. Οι χάρτες του ποσοστού των φάσεων στη χυτή μικροδομή επιτρέπουν την επιλογή της κραμάτωσης σε Mg και Si για την μείωση της ανεπιθύμητης β-AlFeSi. Αυτό αποτελεί ένα καλό αρχικό σημείο για την ομογενοποίηση που ακολουθεί. Με το DGM είναι δυνατόν να υπολογιστεί ο απαιτούμενος χρόνος ομογενοποίησης. Με την ποσοτικοποίηση της κατάστασης ομογενοποίησης μέσω μεταλλογραφικών δεικτών φαίνεται ότι μια πλήρως ομογενοποιημένη κολώνα αλουμινίου για να έχει υψηλή διελασιμότητα πρέπει οι ενδομεταλλικές φάσεις να είναι σφαιροποιημένες και να παρουσιάζουν την μορφολογία neckless. Η ψύξη από τη θερμοκρασία ομογενοποίησης πρέπει να σχεδιαστεί ώστε να αποφευχθεί ο σχηματισμός της β-  $Mg_2Si$  και αντ' αυτής να σχηματιστεί η μετασταθής φάση β'-  $Mg_2Si$ . Αυτό οδηγεί σε χαμηλότερες θερμοκρασίες προθέρμανσης και επιτρέπει την επιβολή μεγαλύτερων φορτίων στη πρέσσα για την επίτευξη υψηλής ταχύτητας διέλασης.

Η ολοκληρωμένη προσομοίωση του μικροδιαφορισμού κατά τη στερεοποίηση, της διαλυτοποίησης του  $Mg_2Si$  και του μετασχηματισμού των ενδομεταλλικών ενώσεων του σιδήρου β-AlFeSi→α-AlFeSi κατά την ομογενοποίηση καθώς και της επανακαθίζησης του  $Mg_2Si$  κατά την ψύξη επιτρέπει τον σχεδιασμό τόσο νέων διελάσιμων κραμάτων αλουμινίου αλλά και της αντίστοιχης κατεργασίας ομογενοποίησης για την επίτευξη υψηλής διελασιμότητας, σε κλάσμα μόνο του χρόνου και κόστους, που απαιτείται για τον αντίστοιχο εμπειρικό σχεδιασμό.



## *Acknowledgements*

The completion of this dissertation would not have been possible without the help of several people whom I would like to thank;

I am grateful to my advisor Prof. G.N. Haidemenopoulos for trusting me and providing me this opportunity to work on his *alloyneering* concept and for his encouragement and guidance both personally and professionally. I owe him many thanks for his friendship and teaching during these years.

I am very grateful to Prof. N. Aravas for serving in my thesis advisory committee and Prof. D. Manolakos for serving in my thesis advisory committee and for providing guidance during my years at NTUA.

I would like to acknowledge Professors D. Pantelis, E. Pavlatou, S. Pantelakis and A.Zavaliangos for serving in my thesis examination committee.

I would like to express my gratitude to the Aluminium of Greece for providing the materials for my thesis and especially El. Grigoriou, A. Triantafyllou and K. Liapis for the fruitful discussions regarding the thesis.

I would like to thank the staff of the Laboratory of Materials of the University of Thessaly but especially Eleni Kamoutsi and Eleana Pappa. During my thesis I had a great support from them.

I am also glad to have worked with undergraduate students but also friends Spyros – Alexandros Tousias, Margianna Tzini, John Aristeidakis and John Fanikos. They have been great partners for me and I wish the best for them.

I would like to thank Lin Shang and Andreas Stieben (RWTH- Aachen) as well as Helen Rosolymou (Chemical Engineering, NTUA) for their assistance with XRD measurements and Dr. Ch.Sarafoglou (Naval Architecture & Marine Engineering) for her assistance with SEM/EDX.

Living in Volos has been exciting and I would like to thank my special friends:

The very first person I met here and best friend since then, Dimitra for just being who she is.

My amazing road-trip friends, Latharo, Vagner and Apostolis for their long *coffee hours*. Their unconditional support has been essential all these years in many ways. My dear lawyer and friend Helen and Dimitris for his music. I am not sure I would have done my thesis without them.

My friends from my NTUA years, Antonis Stefanidis, Kostas Ntaskas, Giorgos Chortis, for being by my side.

I am grateful to my unique in many ways big perfect family. They have cherished with me every great moment and supported me whenever I needed it. And I need to thank them in Greek now,

*Ευχαριστώ την οικογένειά μου. Πρώτα από όλους τους γονείς μου Ιωακείμ και Άννα Σαράφογλου καθώς τους θαυμάζω ξεχωριστά σαν ανθρώπους αλλά και για την ανιδιοτελή τους αγάπη και στήριξη των σπουδών μου. Υπήρξαν το μεγαλύτερο κίνητρο για μένα όλα αυτά τα χρόνια. Ευχαριστώ την αδερφή μου Χαρά γιατί είναι αυτή που είναι και γιατί υπήρξε για μένα το πρότυπο ανθρώπου και επιστήμονα και μου δίνει το κουράγιο να συνεχίζω. Το Σταύρο που χωρίς αυτόν δεν θα ήμουν εδώ σήμερα καθώς πρώτος αυτός πίστεψε σε μένα. Τον αδερφό μου Κώστα και την Αμαλία για την μουσική παιδεία που έχω σήμερα. Τον αδερφό μου Μπάμπη και τη Λέττα για την μαθηματική μου περιέργεια. Τους ευχαριστώ για τα θαυμάσια αντίψια μου !*

*Την Άννα, τον Ιωακείμ, το Στράτο, τη Ζωή μου, το Στράτο και εσένα που έρχεσαι σύντομα!!*

*Αυτό που είμαι σήμερα οφείλεται στους γονείς και τα αδέλφια μου.*

Last but not least my beloved Apostolis for all laughing, crying, travelling, fishing and finally living...I would like to dedicate this thesis to him.

Gioula Sarafoglou  
Volos 2016

# Contents

|        |  |    |
|--------|--|----|
| 1      | Introduction .....   | 9  |
| 1.1.   | Problem statement and aim of the thesis .....                            | 9  |
| 1.2.   | State-of-the-art .....   | 11 |
| 1.3.   | Methodology .....  | 12 |
| 1.4.   | Innovative aspects of the thesis .....                                   | 16 |
| 1.5.   | Structure of the thesis .....  | 17 |
| 2.     | Microsegregation and Phase Fraction Mapping .....                        | 19 |
| 2.1.   | Introduction and literature review .....                                 | 19 |
| 2.2.   | Computational methodology .....  | 21 |
| 2.2.1. | Computational Alloy Thermodynamics .....                                 | 21 |
| 2.2.2. | Amendments in COST507 Al database .....                                  | 27 |
| 2.2.3. | Simulation of microsegregation .....                                     | 27 |
| 2.3.   | Experimental procedures for model validation .....                       | 31 |
| 2.4.   | Results and Discussion .....   | 33 |
| 2.4.1. | Equilibrium calculations .....   | 33 |
| 2.4.2. | Scheil microsegregation simulations .....                                | 35 |
| 2.4.3. | Parametric study on 6060 alloy .....                                     | 37 |
| 2.4.4. | Transformation of $\alpha$ to $\beta$ -AlFeSi after solidification ..... | 42 |
| 2.5.   | Experimental validation .....  | 44 |
| 2.6.   | Effect of Mn on $Mg_2Si$ and $\beta$ -AlFeSi phases .....                | 53 |
| 2.7.   | Mapping of intermetallic phases .....                                    | 55 |
| 2.8.   | Conclusions .....  | 58 |
| 2.9.   | References .....   | 59 |
| 3.     | Simulation of Homogenization .....                                       | 61 |
| 3.1.   | Introduction .....   | 61 |
| 3.2.   | Literature review .....  | 62 |
| 3.3.   | Methodology .....  | 66 |
| 3.3.1. | Computational Method .....   | 66 |
| 3.3.2. | Experimental procedures .....  | 72 |

|         |   |     |
|---------|---|-----|
| 3.4.    | Results and Discussion .....  | 74  |
| 3.4.1.  | Dual Grain Model.....   | 74  |
| 3.4.2.  | Mg <sub>2</sub> Si dissolution.....   | 76  |
| 3.4.3.  | $\beta$ -AlFeSi $\rightarrow\alpha$ -AlFeSi transformation .....              | 77  |
| 3.4.4.  | The effect of temperature and grain size .....                                | 79  |
| 3.4.5.  | Removal of the microsegregation of the alloying elements.....                 | 81  |
| 3.4.6.  | Homogenization Process Map of extrudable 6xxx alloys .....                    | 82  |
| 3.4.7.  | Experimental validation .....   | 83  |
| 3.4.8.  | Transformation $\beta$ -AlFeSi $\rightarrow$ $\alpha$ -AlFeSi.....            | 88  |
| 3.4.9.  | Evolution of elemental profiles during homogenization .....                   | 89  |
| 3.4.10. | Profile and mapping for Mg .....  | 90  |
| 3.4.11. | Profile and mapping for Si .....  | 91  |
| 3.4.12. | Profile and mapping for Mn .....  | 92  |
| 3.5.    | Conclusions .....   | 94  |
| 3.6.    | References .....  | 95  |
| 4.      | Quantification of Homogenization state .....                                  | 97  |
| 4.1.    | Introduction .....  | 97  |
| 4.2.    | Literature review .....   | 97  |
| 4.3.    | Methodology .....   | 98  |
| 4.3.1.  | Quantitative metallography .....  | 99  |
| 4.3.2.  | Image analysis .....  | 100 |
| 4.3.3.  | Statistical Analysis .....  | 102 |
| 4.4.    | Results and Discussion .....  | 103 |
| 4.4.1.  | Metallographic Investigation.....   | 103 |
| 4.4.2.  | Characterization of the particles .....                                       | 104 |
| 4.5.    | Results and discussion.....   | 106 |
| 4.6.    | Conclusions .....   | 108 |
| 4.7.    | References .....  | 108 |
| 5.      | Precipitation during Cooling from the Homogenization Temperature .....        | 109 |
| 5.1.    | Introduction .....  | 109 |
| 5.2.    | Precipitation and hardening during cooling from the homogenization state..... | 111 |



|        |  |     |
|--------|--|-----|
| 5.2.1. | Simulations with the KWN and Strength models ..... | 111 |
| 5.2.2. | Experimental validation .....                      | 115 |
| 5.3.   | Hardening potential of homogenized billets .....   | 115 |
| 5.3.1. | Introduction .....                                 | 115 |
| 5.3.2. | Experimental procedures .....                      | 116 |
| 5.3.3. | Results .....                                      | 117 |
| 5.4.   | Effect of excess-Si on the CCP diagram.....        | 127 |
| 5.4.1. | Introduction .....                                 | 127 |
| 5.4.2. | Methodology .....                                  | 128 |
| 5.4.3. | Results .....                                      | 130 |
| 5.5.   | Design rules for high extrudability .....          | 134 |
| 5.6.   | Conclusions .....                                  | 137 |
| 5.7.   | References .....                                   | 138 |
| 6.     | Conclusions .....                                  | 139 |
| 7.     | Proposal for further research .....                | 145 |

## List of Figures

|   |    |
|---|----|
| Figure 1.1: The process chain of extrudable Al-alloys .....   | 10 |
| Figure 2.1: The three stages during solidification of a binary alloy .....  | 28 |
| Figure 2.2: The composition of the solid at the interface $C_s$ as a function of the fraction<br>solid $f_s$ that has formed, by considering a mass balance .....   | 29 |
| Figure 2.3: Transverse cross sections along the billet diameter .....   | 31 |
| Figure 2.4:(a) Si isopleth for 0.45Mg, 0.03Mn and 0.2 Fe (mass%) and (b) Mg isopleth for<br>0.4Si, 0.03Mn and 0.2 Fe (L=liquid, F=FCC, $\alpha$ = $\alpha$ -AlFeSi, $\beta$ = $\beta$ -AlFeSi, M=Mg <sub>2</sub> Si)..... | 34 |
| Figure 2.5: Isothermal section of Al-Mg-Si with 0.2Fe-0.03Mn (mass %) at 300°C,<br>(L=liquid, F=FCC, $\alpha$ = $\alpha$ -AlFeSi, $\beta$ = $\beta$ -AlFeSi, M=Mg <sub>2</sub> Si) .....                                  | 34 |
| Figure 2.6: Typical solidification paths for a)6082, b)6063, c)6005, d)6060.....  | 35 |
| Figure 2.7: Calculated Solidus temperatures.....  | 36 |
| Figure 2.8: Mole fraction of phases as a function of temperature during solidification of Al-<br>0.38Mg-0.4Si-0.2Fe-0.03Mn (mass%) .....  | 36 |
| Figure 2.9: Microsegregation of phases (a) and microsegregation of alloying elements (b)<br>of Al-0.38Mg-0.4Si-0.2Fe-0.03Mn (mass%) alloy during solidification .....   | 37 |
| Figure 2.10: Segregation of phases for 6060_1 and 6060_3 a) $\alpha$ -AlFeSi, b) $\beta$ -AlFeSi, c)<br>Mg <sub>2</sub> Si, d) Si (Diamond).....  | 38 |
| Figure 2.11: Segregation of phases in 6060-2 and 6060_4 alloys, a) $\alpha$ -AlFeSi, b) $\beta$ -AlFeSi, c)<br>Mg <sub>2</sub> Si, d) Si (Diamond).....   | 39 |
| Figure 2.12: Segregation of elements in 6060_1 and 6060_3 alloys a) Si, b)Mg, c)Fe, d)Mn ...  | 40 |
| Figure 2.13: Segregation of elements in 6060_2 and 6060_4 alloys a) Si, b)Mg, c)Fe, d)Mn ...  | 41 |
| Figure 2.14: The geometric model for the kinetic simulation using the DICTRA<br>computational kinetics software performed for the 6082 alloy.....   | 43 |
| Figure 2.15: The position of fcc/ $\beta$ -AlFeSi interface as a function of simulation (cooling)<br>time.....  | 43 |
| Figure 2.16: The as-cast microstructure of 6082 alloy as observed in the SEM.....   | 44 |
| Figure 2.17: Elemental area mapping (SEM/EDS) in 6082 alloy a) Al, b)Si, c)Mg, d)Fe,<br>e)Mn .....  | 46 |
| Figure 2.18: Matrix composition adjacent to boundary intermetallics: (a) SEM micrograph,<br>(b) Scheil microsegregation profile and (c) EDS signal .....  | 47 |
| Figure 2.19: Typical microstructure of alloys (a) 6082, (b)6063 and (c)6060 .....   | 49 |
| Figure 2.20: Typical morphology of intermetallic $\alpha$ -AlFeSi in 6082 known as “Chinese-<br>script” .....   | 50 |
| Figure 2.21: The (a) quaternary eutectic structure and spherical Mg <sub>2</sub> Si and eutectics of<br>6082 alloy in as-cast condition.....  | 50 |
| Figure 2.22: Microstructures (left) and corresponding Image-J displays used for the<br>measurement of phase fractions.....  | 52 |
| Figure 2.23: Mn-induced reduction of $\beta$ -AlFeSi phase as a function of Si alloy content for<br>various levels of Mg in the alloy .....   | 54 |
| Figure 2.24: Mn-induced reduction in Mg <sub>2</sub> Si phase as a function of Si alloy content for (a)<br>0.4-0.6 and (b) 0.8 1.2 Mg (mass %) in the alloy .....   | 55 |

|   |    |
|---|----|
| Figure 2.25: Contour plots (maps) of fixed mole fractions of (a) $\beta$ -AlFeSi and (b) $Mg_2Si$ phases in the as-cast microstructure of Al-Mg-0.2Fe-Mn alloys (full lines 0.03 Mn, dotted lines 0.45 Mn, mass%) .....   | 56 |
| Figure 2.26: Contour plots (maps) of fixed mole fractions $\beta$ -AlFeSi (solid lines) and $Mg_2Si$ (dotted lines) in as-cast microstructure of Al-Mg-Si-0.2Fe-Mn alloys for (a) 0.03 Mn and (b) 0.45 Mn, mass%. Compositions for alloys 6060, 6063 and 6082 are indicated on the maps. .... | 57 |
| Figure 3.1: The Dual Grain Model considering the different grain sizes between neighboring grains .....   | 67 |
| Figure 3.2: Dispersed Phase model in DICTRA .....   | 68 |
| Figure 3.3: The temperature – time profile of the homogenization process.....   | 72 |
| Figure 3.4 Temporal evolution of phase transformations during the homogenization process a) Isothermal holding at 540°C for 32 h and b) holding at 540° C for 32h cooling down (500°C/2h), preheating 500°C/1h.....   | 75 |
| Figure 3.5: The spatial evolution of the $Mg_2Si$ phase from the grain boundaries and its re-precipitation in the grain interiors .....   | 76 |
| Figure 3.6: The spatial evolution of the $\beta$ -AlFeSi $\rightarrow\alpha$ -AlFeSi transformation a) the initial profiles of $\beta$ -AlFeSi and $\alpha$ -AlFeSi in the as-cast structure, b) the final profiles after the completion of the transformation .....                          | 77 |
| Figure 3.7: Spatial evolution of $\beta\rightarrow\alpha$ -AlFeSi transformation during homogenization for times a) 15 b) 45min c) 1h d)1 ½ h.....  | 79 |
| Figure 3.8: The weight fraction of a) $Mg_2Si$ phase and b) $\beta$ -AlFeSi phase for 3 different homogenization temperatures, 540, 560 and 580°C for homogenization time t=2sec and 500sec respectively.....   | 80 |
| Figure 3.9: The evolution of the concentration profiles of Mg, Si, Fe and Mn in the FCC phase during homogenization at 540°C .....  | 82 |
| Figure 3.10: Homogenization process map of 6082 alloy based on the $\beta$ -AlFeSi $\rightarrow\alpha$ -AlFeSi transformation .....   | 83 |
| Figure3.11: The effect of the homogenization time of the 6082 aluminum alloy for 30min 2,4 and 8h.....  | 85 |
| Figure 3.12: SEM micrographs of 6082 alloy a) as- cast condition b) 0.5, c) 4h, d)8h, e)32h.....  | 86 |
| Figure 3.13: The homogenized microstructure of the 6060 aluminum.....   | 87 |
| Figure 3.14: a)Rounded $\alpha$ -AlFeSi particles and b) neckless morphology in SEM micrographs .....   | 87 |
| Figure 3.15: XRD spectrum of the $\beta$ -AlFeSi $\rightarrow\alpha$ -AlFeSi transformation of 6082 alloy .....   | 88 |
| Figure 3.16: The XRD spectrum for the 6060 alloy homogenized at 560°C for 0.5h .....  | 89 |
| Figure 3.17: a) Simulation results and experimental for Fe element, b)profile mapping in as – cast condition, c)0.5, d) 4h, e) 8h, f) 32h homogenization time.....  | 90 |
| Figure 3.18: a) Simulation results and experimental for Mg element, b)profile mapping in as – cast condition, c)0.5, d) 4h, e) 8h, f) 32h homogenization time.....  | 91 |
| Figure 3.19: a) Simulation results and experimental for Si element, b)profile mapping in as–cast condition, c)0.5, d) 4h, e) 8h, f) 32h homogenization time.....  | 92 |
| Figure 3.20: a) Simulation results and experimental for Mn element, b)profile mapping in as – cast condition, c)0.5, d) 4h, e) 8h, f) 32h homogenization time.....  | 93 |

|  |     |
|--|-----|
| Figure 4.1: SEM image used for the measurement of indices: (a) Low magnification image, (b) high magnification isolation of the group of particles, (c) image J display used for the measurement of the indices .....  | 101 |
| Figure 4.2: Metallographic images, (a) as-cast, (b) homogenized at 540°C, (c) 560°C and (d) 580°C .....  | 104 |
| Figure 4.3: Images indicating the rounding of the edges of the particles during homogenization .....   | 105 |
| Figure 4.4: Images revealing the pinching process during homogenization.....   | 105 |
| Figure 4.5: Images revealing the spherical shape at the third stage .....  | 106 |
| Figure 4.6: The values of indices for the as-cast and homogenized alloys: (a) aspect ratio, (b) feret, (c) circularity and (d) circularity of edges .....  | 107 |
| Figure 5.1: Measured cooling profiles used in simulations and in the experimental validation, (a) natural cooling, (b) forced cooling.....   | 112 |
| Figure 5.2: Simulation results for the 6063 alloy: (a) evolution of Mg <sub>2</sub> Si volume fraction during cooling for three homogenization temperatures 540, 560 and 580°C and (b) evolution of particle size during cooling for natural and forced cooling from 580°C homogenization temperature..... | 113 |
| Figure 5.3: Particle size distribution (PSD) predicted by the KWN model for the 6063 alloy for the two cooling profiles, natural and forced cooling for the 580°C homogenization temperature .....   | 114 |
| Figure 5.4: Evolution of hardness during cooling of the 6063 alloy for natural and forced cooling and for three homogenization temperatures 540, 560 and 580°C.....  | 114 |
| Figure 5.5: Homogenization cooling profiles.....   | 117 |
| Figure 5.6: Brinell hardness of alloy 6082 immediately after cooling from the homogenization temperature .....   | 118 |
| Figure 5.7: Brinell hardness of alloy 6005 immediately after cooling from the homogenization temperature .....   | 119 |
| Figure 5.8: Brinell hardness of alloy 6063 immediately after cooling from the homogenization temperature .....   | 120 |
| Figure 5.9 Brinell hardness immediately after cooling from 540°C homogenization temperature .....  | 121 |
| Figure 5.10: Brinell hardness immediately after cooling from 560°C homogenization temperature .....  | 121 |
| Figure 5.11: Brinell hardness immediately after cooling from 580°C homogenization temperature .....  | 121 |
| Figure 5.12: Brinell hardness after homogenization and natural aging for the 6082 alloy.   | 123 |
| Figure 5.13: Brinell hardness after homogenization and natural aging for the 6005 alloy.   | 123 |
| Figure 5.14: Brinell hardness after homogenization and natural aging for the 6063 alloy.   | 123 |
| Figure 5.15: Hardening potential Hp for the 6082 alloy at (a) 540, (b) 560 and (c) 580°C homogenization temperatures .....   | 124 |
| Figure 5.16: Hardening potential Hp for the 6005 alloy at (a) 540, (b) 560 and (c) 580°C homogenization temperatures .....   | 125 |
| Figure 5.17: Hardening potential Hp for the 6063 alloy at (a) 540, (b) 560 and (c) 580°C homogenization temperatures. ....   | 126 |
| Figure 5.18: DSC spectra for 6005 alloy (0.57Mg-0.68Si) for cooling rates from 0.1 to 375 K/min [18] .....   | 129 |

|   |     |
|---|-----|
| Figure 5.19: CCP diagram for 6060, 6063, 6005 and 6082 alloys [18] .....  | 130 |
| Figure 5.20: Arrhenius fitting of the data of Table 2 a) Fitting the $\beta$ -nose, b) fitting $\beta'$ - nose .....  | 131 |
| Figure 5.21: Effect of excess Si on the precipitation of $\beta'$ -Mg <sub>2</sub> Si.....  | 133 |
| Figure 5.22: CCP diagram of the 6060_3 alloy (red lines). The dotted $\beta'$ line is shifted by taking into account only the Mg effect. The $\beta'$ nose (full line) is shifted by taking into account the effect of excess Si in the 6060_3 alloy..... | 134 |

## List of Tables

|  |     |
|--|-----|
| Table 1.1: Methodology of the present Thesis .....   | 15  |
| Table 2.1: Chemical composition of alloys 6082, 6063, 6005, 6060 (in mass %) .....   | 31  |
| Table 2.2: Metallographic procedure for 6060, 6082 and 6063 alloys .....   | 32  |
| Table 2.3: Segregation index for the 6060 alloy variants .....   | 42  |
| Table 2.4: Chemical composition of $\alpha$ -AlFeSi phase (mass %) .....   | 45  |
| Table 2.5: Comparison between calculated and measured (EDS) matrix composition<br>adjacent to boundary intermetallics .....                  | 48  |
| Table 2.6: Comparison between calculated and measured phase fractions in the as-cast<br>6082 alloy .....                                     | 53  |
| Table 3.1: Eutectic melting temperatures in Al-Mg-Si alloys [10] .....   | 64  |
| Table 4.1 Homogenization heat treatments .....   | 99  |
| Table 4.2: Number of images analyzed and number of particles measured per billet for the<br>quantification of the homogenization state ..... | 99  |
| Table 4.3: The indices employed for the quantification of the homogenization state .....   | 100 |
| Table 4.4: Respective measurements for each particle referring to Figure 4.1 .....   | 102 |
| Table 5.1: Microhardness ( $HV_{0.3}$ ) as a function of cooling profile .....   | 115 |
| Table 5.2 Position of $\beta$ and $\beta$ noses from the CCP diagrams of Fig.2 .....   | 131 |
| Table 5.3: Calculation of excess Si of the alloys (compositions in wt%) .....  | 132 |

# Introduction

## 1.1. Problem statement and aim of the thesis

Extrudable aluminum alloys of the 6xxx series are heat-treatable alloys based on the Al-Mg-Si system. These alloys find significant applications in the building, construction and transportation sectors due to the excellent strength/ductility properties combined with reduced weight and oxidation resistance. Large scale ingots or billets, suitable for hot extrusion, are produced with the direct-chill casting method. The as-cast material exhibits low formability due to microstructural inhomogeneities, arising from the solidification process and the alloy chemistry. Major inhomogeneities in the as-cast material include: elemental microsegregation in the level of the secondary dendrite arms, grain boundary segregation and the formation of several low-melting eutectics and intermetallic compounds such as the iron-containing  $\alpha$ -AlFeSi and  $\beta$ -AlFeSi, which degrade the extrudability of the as-cast billet.

These effects can be partially or completely eliminated with the application of a homogenization treatment of the as-cast billets. The benefits of this treatment include the following: removal of elemental microsegregation, dissolution of low melting eutectics, transformation of the iron-containing intermetallic compounds, shape control (round-off) of hard particles with sharp edges, dissolution of the grain-boundary  $\text{Mg}_2\text{Si}$  phase and re-precipitation (during cooling) with a more homogeneous in-grain distribution. All these effects improve the extrudability and increase the response of the material to natural or artificial aging.

New demanding light-weight applications in the automotive and aircraft sectors require the development of high-strength alloy extrusions. Such applications include pillar and chassis structural parts in vehicles and wing or fuselage reinforcement parts in aircrafts. The increase of strength is possible with higher alloying with Mg and Si, in order to form higher amounts of the strengthening phase  $\text{Mg}_2\text{Si}$  (e.g. 6061 and 6082 alloys). However increased alloying deteriorates the extrudability, leading to extremely low extrusion speeds for the high-strength alloy systems. In the other end of the spectrum, i.e. low-alloy low-strength applications (e.g. 6060 or 6063 alloys), the main industrial

requirement is to increase the extrusion speed, in order to increase production rates. In both cases, it appears that extrudability is the key property that should be controlled and improved through a carefully designed homogenization process.

So far the problem has been tackled in a rather empirical way, involving intense trial-and-error laboratory or even industrial experiments to determine the effect of alloy chemistry and homogenization process parameters such as the homogenization temperature and time and the cooling rate following homogenization. In most cases only individual aspects of the process are considered and the effect of prior processing is often neglected.

The process chain of extrudable Al-alloys is depicted in Figure 1.1. . The design of new high-strength 6xxx alloys, exhibiting adequate extrudability, as well as the design of low-strength alloys with high extrudability, calls for an *integrated approach* considering all parts of the *process chain* and their effect on extrudability.

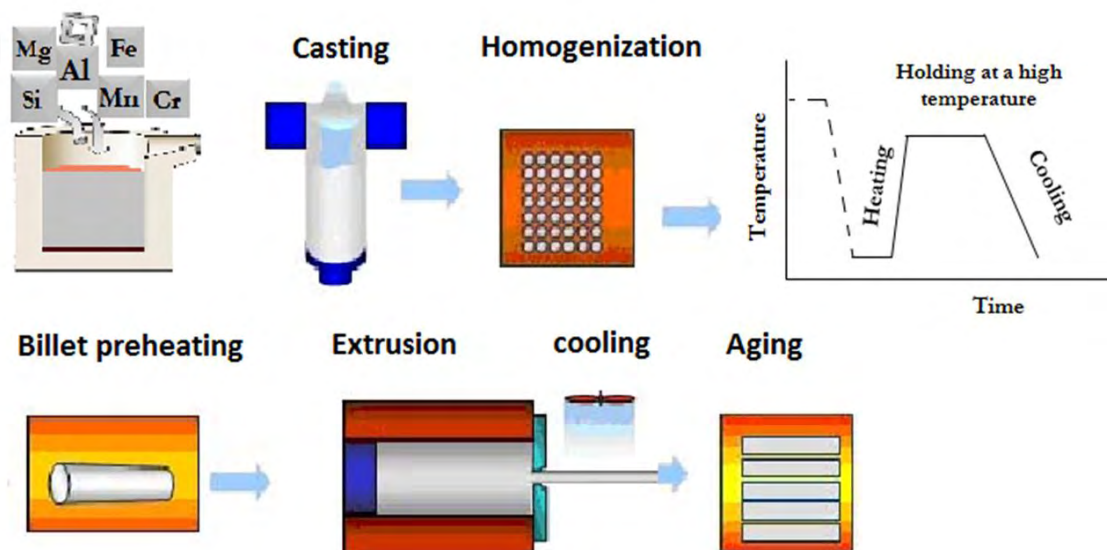


Figure 2.1: The process chain of extrudable Al-alloys

By this it is meant that not only processing steps prior to extrusion are important but steps following the extrusion process should be considered as well, since they set important microstructural requirements to be achieved in the preceding process steps. For example, the homogenization process is carried out in order to eliminate the microsegregation



established in the previous process steps, however it should also aim to prepare the material for best response to the aging treatment, which follows the extrusion and sets the final properties of the extruded profiles.

An even more ambitious approach is to combine the thermodynamic calculations with kinetic models, e.g. diffusion calculations and thereby predict the rate of phase transformations, which shape the microstructure across the process chain. This approach is extremely powerful and may be used to simulate a wide range of different phenomena such as solidification and microsegregation during casting, dissolution of  $\text{Mg}_2\text{Si}$ , removal of microsegregation and transformation of iron intermetallics during homogenization and finally re-precipitation during cooling from the homogenization temperature.

The aim of this doctoral thesis is to apply a *simulation-based approach*, validated by relevant experimental data, in order to describe the effect of alloy chemistry and homogenization process conditions on the material microstructure prior to extrusion. In this way it will be possible to shape *design rules* (in terms of composition and processing) for the development of either high-strength alloys with considerable extrudability or low-strength alloys with high extrudability.

## **1.2. State-of-the-art**

As it will be shown by the literature review in the next sections, the problem of the design of alloy compositions and homogenization treatments for enhanced extrudability has been considered by experimental methods either in the laboratory or by industrial trials. In most cases, parts of the process chain have been considered individually. Most works consider the effect of composition or process parameters such as the homogenization time and temperature or the effect of the cooling rate individually on the outcome of the homogenization process. In this way, 'best-practice' homogenization recipes have been established for certain alloys. For the design of a new alloy composition or the design of a new homogenization treatment for enhanced extrudability, the traditional trial-and-error methodology is still followed.

In terms of process simulation, the work performed so far is rather limited to modeling specific aspects of the process and to the author's knowledge there is no integrated simulation approach that eventually leads to the development of design rules for alloy composition and homogenization treatments of extrudable aluminum alloys. A complete literature review is presented in the following sections of the thesis.

### **1.3. Methodology**

The approach followed in this thesis has both computational and experimental aspects. A flow chart of the methodology is depicted in Table 1.1.

#### **❖ *Computational***

Computational alloy thermodynamics, based on the CALPHAD approach, has been applied for the calculation of equilibrium phase constitution as a function of alloy composition and temperature. Isopleth phase diagrams in multicomponent alloys have been calculated permitting the determination of the stability limits of the various phases in the system. The relevant thermochemical database COST-507 for light alloys has been modified to incorporate Manganese (Mn) in the  $\alpha$ -AlFeSi iron intermetallic. The relevant software used was Thermo-Calc. The program was also applied to carry out Scheil-Gulliver solidification simulations and calculate the resulting microsegregation of elements and phases in the as-cast microstructure. Segregation profiles for elements and phases across the grain were determined as a function of alloy composition. The results were confirmed experimentally.

Computational kinetics, based on the solution of the diffusion equations in multicomponent systems (Onsager principle) was applied in order to calculate the rate of diffusional phase transformations during homogenization. In this way the dissolution of the  $\text{Mg}_2\text{Si}$  phase, the transformation of iron intermetallics ( $\beta$ -AlFeSi to  $\alpha$ -AlFeSi) as well as the reprecipitation during cooling was simulated. This included the development of a dual-grain model (DGM) to take into account the different grain sizes between neighboring grains. The relevant software was DICTRA, which incorporates the so-called sharp interface model for treating diffusion-controlled transformations. The interdiffusion coefficients

were calculated by the program with data from the mobility database MOB2, which contains all the information on the temperature dependence of mobility coefficients. The relevant thermodynamic factors, taking into account the compositional dependence, were calculated by a link to Thermo-Calc. Initial composition profiles of elements and phases were the direct results of the Scheil simulations of the previous step. In this way it was possible to connect the solidification step with the homogenization step.

The Kampmann-Wagner numerical model (KWN), with which precipitation in isothermal conditions can be calculated, was applied under continuous cooling conditions (by a suitable matlab code) in order to evaluate the effect of excess-Si on the precipitation of metastable  $\beta'$ -Mg<sub>2</sub>Si during cooling from the homogenization temperature. This led to the modification of existing CCP diagrams and permits the design of cooling programs to achieve precipitation of the desirable  $\beta'$  instead of the equilibrium phase  $\beta$ -Mg<sub>2</sub>Si. In addition the KWN model was combined with a suitable strength model, involving precipitation strengthening, in order to calculate the strength (hardness) of the alloy following homogenization cooling.

## ❖ *Experimental*

Standard metallographic techniques including optical microscopy and scanning electron microscopy (SEM) were applied to reveal the microstructure of the as-cast and homogenized materials. Phase fractions were measured by applying quantitative image analysis.

Segregation profiles and the evolution of elemental profiles during homogenization was performed by SEM-EDX measurements

Evolution of phase transformation during homogenization was performed with XRD. Characterization of the homogenization state was performed with the measurement of microstructural indices (aspect ratio, feret, circularity, circularity of edges) in a large number of SEM images.

Laboratory homogenization treatments were performed in selected alloys in order to study the progress of homogenization. The hardness after cooling from the homogenization temperature was also determined.

Table 2.1: Methodology of the present Thesis

| PROCESS CHAIN             | METHOD/<br>SIMULATION  | RESULTS   | CONTRIBUTIONS TO<br>DESIGN RULES FOR<br>HIGH EXTRUDABILITY  |
|---------------------------|--|---|---|
| Casting                   | Scheil – Gulliver<br>(CALPHAD – based)<br><i>Ch.2</i>  | Microsegregation<br>Elements/phases   | Mg-Si map of phase fractions in<br>as-cast structure  |
|                           |  |   | Selection of compositions with<br>high Mg <sub>2</sub> Si and low $\beta$ -AlFeSi                   |
| Homogenization            | Dual Grain Model (DGM)<br>Multicomponent Diffusion in<br>multiphase, variable grain<br>system<br><i>Ch.3</i> | Mg <sub>2</sub> Si dissolution<br>$\beta \rightarrow \alpha$ – AlFeSi<br>transformation | 1 <sup>st</sup> process map based on time<br>for $\beta \rightarrow \alpha$ - AlFeSi transformation |
|                           | Quantitative metallography<br>Measurements of indices:<br>aspect ratio and circularity<br><i>Ch.4</i>        | Index – based<br>quantification of the<br>homogenization<br>state                       | Selection of homogenization<br>temperature/time to achieve<br>specific index values                 |
| Homogenization<br>cooling | Kampmann – Wagner<br>Numerical Model (KWN)   | Evolution of PSD of<br>Mg <sub>2</sub> Si during<br>cooling                             | CCP diagram for the design of<br>homogenization cooling   |
|                           | Strength Model<br><i>Ch.5</i>  | Hardness of<br>homogenized billets<br>Effects on CCP<br>diagrams                        |   |

## 1.4. Innovative aspects of the thesis

The thesis provides results leading to progress beyond the state-of-the-art in the area of the computational-based design of the homogenization process of extrudable aluminum alloys. Such innovative aspects are:

- The application of a computational thermodynamics and kinetics approach, for the integrated simulation of the process chain including, solidification-induced microsegregation and subsequent homogenization in multicomponent and multiphase aluminum alloys.
- The development of a homogenization dual-grain model (DGM), for the evaluation of the effect of different grain size between neighboring grains.
- The description of temporal and spatial correspondence, of the  $\beta$ -AlFeSi to  $\alpha$ -AlFeSi transformation during homogenization.
- The evaluation of the effect of excess-Si on the precipitation of metastable  $\beta'$ -Mg<sub>2</sub>Si during cooling from the homogenization temperature by the application of the KWN precipitation model.
- The application of microstructural indices for the characterization of homogenization state of extrudable aluminum alloys by quantitative metallography.
- The development of design rules for the as-cast microstructure in terms of mapping phase fractions of desirable and undesirable phases with respect to alloy composition.
- The development of design rules for selection of alloy compositions and processing conditions for homogenization.

## 1.5. Structure of the thesis

The structure of the thesis follows the process chain, of the extrudable Al-alloys.

**Chapter 2** deals with the evolution of the as-cast microstructure and more specifically with the microsegregation of elements and phases as a result of solidification. The mapping of phase fraction in the Mg-Si composition space is also presented in this chapter.

The simulation of homogenization with the DGM is described in **Chapter 3**. The DGM deals with the temporal and spatial evolution of the  $\beta$  to  $\alpha$  – AlFeSi transformation. A process map based on the time for the completion of the  $\beta$  to  $\alpha$ -AlFeSi transformation is presented.

The index-based quantification of the homogenization state is presented in **Chapter 4**.

Precipitation of the  $\text{Mg}_2\text{Si}$  during homogenization cooling with the KWN model is presented in **Chapter 5**. The development of design rules for high extrudability is also presented in Chapter 5.

The conclusions of this thesis and proposal for further research are presented in **Chapter 6 and 7** respectively.





## 2. Microsegregation and Phase Fraction Mapping

### 2.1. Introduction and literature review

Extrudable aluminum alloys of the 6xxx series, based on the Al-Mg-Si system, are subjected to a rather complicated process chain involving melt treatment, casting, homogenization, preheating, extrusion, and ageing. The process chain begins with the direct casting (DC casting) of large cylindrical billets. The as-cast microstructure, which depends on composition and casting conditions, influences in a large degree the properties of extrudable 6xxx Al-alloys. The as-cast material exhibits low formability due to microstructural inhomogeneities, arising from the solidification process and the alloy chemistry. Major inhomogeneities in the as-cast material, which degrade the extrudability of the as cast billet include:

- elemental microsegregation in the level of the secondary dendrite arms
- grain boundary segregation and formation of low-melting eutectics
- formation of intermetallic compounds

The research work described in this section focuses on the composition and microstructural evolution of the as-cast billets since these key factors influence not only the extrudability but the product properties of Al-alloys after extrusion has been completed.

The 6xxx series alloys, which are based on the ternary Al-Mg-Si alloy system, contain magnesium (Mg) and silicon (Si) as major alloying elements for the formation of  $\text{Mg}_2\text{Si}$ , which is the major strengthening phase, providing precipitation hardening after aging.

Besides the intentional additions Mg and Si, transition metals and impurities such as Fe, Mn and Cr are present. Even a small amount of these impurities causes the formation of new intermetallic compounds (IMCs). The composition of the alloy as well as casting conditions will influence the exact type and volume fraction of intermetallic phases that will form during casting [1].

Iron (Fe), is the main impurity in these alloys forming intermetallic compounds in combination with Si such as  $\beta\text{-Al}_5\text{FeSi}$  and  $\alpha\text{-Al}_{12}\text{Fe}_3\text{Si}$ . In addition, Mn can substitute for Fe, and promote the formation of  $\alpha\text{-Al}_{12}(\text{FeMn})_3\text{Si}$ . These phases, from now on called  $\beta$ -

AlFeSi and  $\alpha$ -AlFeSi respectively, are mostly located at the grain boundaries in the as-cast microstructure. The  $\beta$ -AlFeSi phase has a monoclinic crystal structure and plate-like morphology, while  $\alpha$ -AlFeSi has a cubic crystal structure and a globular morphology. The plate-like morphology of the  $\beta$ -AlFeSi phase limits the extrudability of the alloy since it induces local cracking and surface defects in the extruded material, while the presence of the more rounded  $\alpha$ -AlFeSi phase has a lesser impact on the extrudability of the alloy [2]. The disadvantage of the high Fe content is the enhanced probability of forming large particles of  $\beta$ -AlFeSi, with a detrimental impact on the extrudability of the alloy [3]. On the other hand, Si has an important role together with magnesium (Mg) in forming  $Mg_2Si$ , or  $\beta$ -phase, the transition phase of which,  $\beta''$ , is the main hardening precipitate in the alloy [4]. Cr may assist in the formation of the AlFeCrSi phase, which has a very important role in the grain size control [5]. Furthermore microsegregation takes place during solidification in the scale of the secondary dendrite arm spacing (SDAS) due to the difference of the thermodynamic equilibrium solubility of alloying elements between the solid and liquid phases. The influence of alloy composition on the formation of intermetallic compounds has been generally studied experimentally [2-4]. Considerably less work has been performed on the formation of intermetallic phases during casting of Al-billets. The main objective of these works has been the study of the morphology and dispersion of IMC's in the as-cast microstructure. The effect of cooling rate on as-cast microstructure formation [6-8] as well as the formation of  $Mg_2Si$  and other intermetallic phases in Al-Mg-Si alloys [9, 10] have been studied experimentally. Finally a thermodynamic description of the Al-Fe-Mg-Mn-Si system and investigations on the microsegregation during directional solidification of alloys based on that system has been presented [11].

Despite the above works, a systematic analysis of the effect of alloying elements on microsegregation and IMC formation in Al-Mg-Si-Fe-Mn alloys does not exist. Such a study would assist the selection of alloy compositions for the minimization of the undesirable  $\beta$ -AlFeSi phase in the as-cast microstructure. With such an optimized as-cast microstructure it would be easier to reach the homogenization target and increase the extrudability without sacrificing strength in these alloys.

## 2.2. Computational methodology

The present work is an effort to present in detail the effect of the major alloying elements Mg and Si on microsegregation and the formation of  $\text{Mg}_2\text{Si}$  and Fe intermetallics during solidification of extrudable 6xxx Al-alloys. Mn is added in these alloys in order to speed up the  $\beta \rightarrow \alpha$  transformation during homogenization. However the effect of Mn on IMC formation in the as-cast microstructure has not been assessed. Therefore in this work the effect of Mn is also quantified. In the first part, a computational thermodynamics-based analysis of equilibrium phase constitution is presented, in order to identify the major phases and their stability limits in the alloys. Solidification of the Al-billets is then modelled by applying Scheil simulations in order to compute the mole fractions of all phases as well as their segregation in the as-cast structure. Computed fractions are validated against experimented measurements. The mole fraction of  $\text{Mg}_2\text{Si}$  and the  $\beta\text{-AlFeSi}$  phase is then mapped over the useful (0-1.2 mass %) Mg-Si composition space for 6xxx extrudable alloys.

### 2.2.1. Computational Alloy Thermodynamics

All necessary thermodynamics calculations for the description of the Gibbs free energy of the various phases in the system were performed with the Thermo-Calc software [12], which is based on the CALPHAD approach [13]. This is a method that overcomes the problem of the multi-dimensionality posed by a system with many components. A thermodynamic description of a system requires assignment of thermodynamic functions for each phase. The CALPHAD method employs a variety of models to describe the temperature, pressure and concentration dependence of the free energy functions of the various phases. The description refers to pure metals, stoichiometric and non-stoichiometric phases and intermetallic compounds as well as substitutional and interstitial solid solutions. It is based on the minimization of the total free energy of the system, comprising of all phases, which take part in equilibrium of a multicomponent system. The total free energy is the sum of the free energies of individual phases

$$G = \sum_{i=1}^p n_i G_i^{\phi} \quad (1)$$

where,

$n_i$  is the number of moles of phase  $i$

$G_i$  is the Gibbs free energy of phase  $i$

For multicomponent systems the Gibbs free energy of a phase is the sum of four contributions:

$$G_i = G^o + G^{id} + G^{xs} + G^{mag} \quad (2)$$

where

$G^o$  is the contribution of the pure components

$G^{id}$  corresponds to the ideal or entropic term

$G^{xs}$  is the excess term corresponding to the deviation from ideality and

$G^{mag}$  is the magnetic contribution to the Gibbs free energy due to magnetic ordering.

The major phases and stability limits for the case of Al-Mg-Si-Fe system are described in the COST507 light alloys database [14]. This is a public domain thermodynamic database created in the course of the European concerted action program “Development of a thermochemical and thermos-physical database for light alloys”. The Laboratory of Materials at the University of Thessaly was a member of this consortium and contributed to the development of the database. The description of the relevant phases of interest in the COST507 database is given in the following sections.

#### ❖ FCC and Liquid

The free energy of the FCC substitutional solid solution phase ( $\alpha$ -Al) as well as the liquid phase are expressed according to equation (2) as:

$$G = \sum_i X_i G_i^o + RT \sum_i X_i \ln X_i + \sum_i \sum_{j \neq i} X_i X_j \sum_p L_{ij}^{(p)} (X_i - X_j)^p + \sum_i \sum_{j \neq k} X_i X_j X_k \sum_p L_{ijk}^{(p)} \quad (3)$$

where,

$R$  is the universal gas constant

$T$  is the temperature (in Kelvin)

$X_i$  are the mole fractions of the elements (i = Al, Mg, Si, Fe, Mn)

$G_i^o$  are the free energies of the elements

The free energy contribution of the pure elements is

$$G^{o,LQ} = X_{Al} G_{Al}^{o,LQ} + X_{Mg} G_{Mg}^{o,LQ} + X_{Si} G_{Si}^{o,LQ} + X_{Fe} G_{Fe}^{o,LQ} + X_{Mn} G_{Mn}^{o,LQ} \quad (4)$$

Where, for example,  $G_{Mg}^{o,LQ}$  is the free energy of Mg, which for 298.15<T<923K is

$$G_{Mg}^{o,LQ} - H_{Mg}(298.15K) = 8202.24 - 8.83T - 8.01 \times 10^{-20} T^7 + G_{Mg}^{SER}(T) \quad (5)$$

and for 923<T<6000K the free energy term is

$$G_{Mg}^{o,LQ} - H_{Mg}(298.15K) = 8690.31 - 9.39T - 1.03 \times 10^{-28} T^9 + G_{Mg}^{SER}(T) \quad (6)$$

$G_{Mg}^{SER}(T)$  is the free energy with respect to the reference state (Stable Element Reference, SER) defined as the enthalpy of the pure metal at 298.15K.

For the Liquid phase, the ideal term  $G^{id}$  can be described as

$$G^{id,LQ} = RT(X_{Al} \ln X_{Al} + X_{Mg} \ln X_{Mg} + X_{Si} \ln X_{Si} + X_{Fe} \ln X_{Fe} + X_{Mn} \ln X_{Mn}) \quad (7)$$

As can be seen from equation (7) the ideal term corresponds to the entropic contribution to free energy.

The third and fourth terms on the right hand side of equation (3) represent the excess term in the form of a Redlich-Kister-Muggianu (RKM) expansion, which takes into account the composition dependence of the interaction between elements, a procedure followed in the CALPHAD approach. The interaction parameters  $L_{ij}^{(p)}$  and  $L_{ijk}^{(p)}$  are the binary and ternary interaction parameters of order p and are temperature dependent. With the use of the interaction parameters, the excess term can be described as follows:

$$\begin{aligned}
G^{XS,LIQ} = & X_{Al}X_{Mg}[L_{Al,Mg}^{(0)} + L_{Al,Mg}^{(1)}(X_{Al} - X_{Mg}) + L_{Al,Mg}^{(2)}(X_{Al} - X_{Mg})^2] + \\
& + X_{Al}X_{Si}[L_{Al,Si}^{(0)} + L_{Al,Si}^{(1)}(X_{Al} - X_{Si}) + L_{Al,Si}^{(2)}(X_{Al} - X_{Si})^2] + \\
& + X_{Al}X_{Fe}[L_{Al,Fe}^{(0)} + L_{Al,Fe}^{(1)}(X_{Al} - X_{Fe}) + L_{Al,Fe}^{(2)}(X_{Al} - X_{Fe})^2] + \\
& + X_{Al}X_{Mn}[L_{Al,Mn}^{(0)} + L_{Al,Mn}^{(1)}(X_{Al} - X_{Mn}) + L_{Al,Mn}^{(2)}(X_{Al} - X_{Mn})^2] + \\
& + X_{Fe}X_{Mg}[L_{Fe,Mg}^{(0)} + L_{Fe,Mg}^{(1)}(X_{Fe} - X_{Mg})] + X_{Fe}X_{Mn}[L_{Fe,Mn}^{(0)} + L_{Fe,Mn}^{(1)}(X_{Fe} - X_{Mn})] + \\
& + X_{Fe}X_{Si}[L_{Fe,Si}^{(0)} + L_{Fe,Si}^{(1)}(X_{Fe} - X_{Si}) + L_{Fe,Si}^{(2)}(X_{Fe} - X_{Si})^2 + L_{Fe,Si}^{(3)}(X_{Fe} - X_{Si})^3] + X_{Mg}X_{Mn}L_{Mg,Mn}^{(0)} \\
& + X_{Mg}X_{Si}[L_{Mg,Si}^{(0)} + L_{Mg,Si}^{(1)}(X_{Mg} - X_{Si}) + L_{Mg,Si}^{(2)}(X_{Mg} - X_{Si})^2 + L_{Mg,Si}^{(3)}(X_{Mg} - X_{Si})^3 + L_{Mg,Si}^{(4)}(X_{Mg} - X_{Si})^4] + \\
& + X_{Mn}X_{Si}[L_{Mn,Si}^{(0)} + L_{Mn,Si}^{(1)}(X_{Mn} - X_{Si}) + L_{Mn,Si}^{(2)}(X_{Mn} - X_{Si})^2 + L_{Mn,Si}^{(3)}(X_{Mn} - X_{Si})^3] + \\
& + X_{Al}X_{Mg}X_{Si}[L_{Al,Mg,Si}^{(0)} + L_{Al,Mg,Si}^{(1)} + L_{Al,Mg,Si}^{(2)}] + X_{Al}X_{Mn}X_{Si}L_{Al,Mn,Si}^{(0)} \quad (8)
\end{aligned}$$

All values of the relevant interaction parameters are stored in the COST507 database.

As mentioned above, an additional term expressing the magnetic contribution to the Gibbs free energy has to be added to equation (1). This term is expressed according to Inden [15] as

$$G^{mag} = RT \ln(\beta + 1) f(\tau) \quad (9)$$

where,

$\beta$  is the magnetic moment in Bohr magnetons. It is composition-dependent and is given by

$$\beta = \sum_i X_i \beta_i^o + \sum_i \sum_{i \neq j} X_i X_j \sum_p [\beta^{(p)} (X_i - X_j)^{(p)}] \quad (10)$$

where

$\tau$  is a normalized temperature,

with  $\tau = T/T_c$  and  $T_c$  being the Curie temperature

which is composition-dependent and is given by

$$T_c = \sum_i X_i T_{c_i}^o + \sum_i \sum_{i \neq j} X_i X_j \sum_p [T_c^{(p)} (X_i - X_j)^{(p)}] \quad (11)$$

The values of  $\beta$  and  $T_c$  are stored for the FCC phase in the COST 507 database.

#### ❖ $\beta$ -AlFeSi phase

The  $\beta$ -AlFeSi phase is treated as a stoichiometric  $\text{Al}_{14}\text{Fe}_3\text{Si}_3$  intermetallic compound.

The Gibbs free energy is then

$$G_{\text{Al}_{14}\text{Fe}_3\text{Si}_3}(T) - 14H_{\text{Al}}(298.15) - 3H_{\text{Fe}}(298.15) - 3H_{\text{Si}}(298.15) = \Delta G_{\text{Al}_{14}\text{Fe}_3\text{Si}_3}^f(T) + 14G_{\text{Al}}^{\text{SER}}(T) + 3G_{\text{Fe}}^{\text{SER}}(T) + 3G_{\text{Si}}^{\text{SER}}(T) \quad (12)$$

As mentioned above, the left hand side in (12) is the free energy relative to the reference state, called stable element reference (SER), with the enthalpies of the elements evaluated at room temperature (298.15K). The term  $\Delta G_{\text{Al}_{14}\text{Fe}_3\text{Si}_3}^f$  is the temperature-dependent energy of formation of the intermetallic compound and is stored together with the free energies of the pure elements  $G_i^{\text{SER}}(T)$  (i=Al, Fe, Si) in the COST 507 database.

#### ❖ $\alpha$ -AlFeSi phase

The  $\alpha$ -AlFeSi phase is treated as a non-stoichiometric intermetallic compound. The free energy description is based on the sublattice model, developed by Sundman and Agren [16]. Four sub lattices are used for the phase description as (Al):(Fe):(Si):(Al,Si) with sites 0.6612:0.19:0.0496:0.0992 respectively. The first three sub lattices are exclusively occupied by a single element while in the fourth sublattice there is partial occupation by Al and Si. The site occupation in the fourth sublattice is expressed by the site fraction  $y_i^{(4)}$  where  $i=Al,Si$ . Considering exclusive occupation by Al or Si in the fourth sublattice, two terminal stoichiometric compounds are defined,  $Al_{0.7604}Fe_{0.19}Si_{0.496}$  and  $Al_{0.6612}Fe_{0.19}Si_{0.1488}$  called G1 and G2 respectively from now on for clarity. Then the free energy of the  $\alpha$ -AlFeSi phase can be described in terms of the free energies of the terminal compounds as

$$G_{\alpha-AlFeSi} = y_{Al}^{(4)}G_1 + y_{Si}^{(4)}G_2 + 0.0992RT(y_{Al}^{(4)} \ln y_{Al}^{(4)} + y_{Si}^{(4)} \ln y_{Si}^{(4)}) \quad (13)$$

where the first two terms correspond to the free energies of the terminal stoichiometric compounds and the third is the entropic term.

The free energies of the terminal compounds are

$$\begin{aligned} G_1(T) - 0.7604H_{Al}(298.15) - 0.19H_{Fe}(298.15) - 0.0496H_{Si}(298.15) = \\ = \Delta G_1^f + 0.7604G_{Al}^{SER}(T) + 0.19G_{Fe}^{SER}(T) + 0.0496G_{Si}^{SER}(T) \end{aligned} \quad (14)$$

and

$$\begin{aligned} G_2(T) - 0.6612H_{Al}(298.15) - 0.19H_{Fe}(298.15) - 0.1488H_{Si}(298.15) = \\ = \Delta G_2^f + 0.6612G_{Al}^{SER}(T) + 0.19G_{Fe}^{SER}(T) + 0.1488G_{Si}^{SER}(T) \end{aligned} \quad (15)$$

The free energies of formation of  $\Delta G_1^f$  and  $\Delta G_2^f$  of the terminal compounds are stored in the COST 507 database.



### ❖ Mg<sub>2</sub>Si strengthening phase

The Mg<sub>2</sub>Si phase is also treated as a stoichiometric phase. The Gibbs free energy is then

$$G_{Mg_2Si}(T) - 2H_{Mg}(298.15K) - H_{Si}(298.15K) = \Delta G_{Mg_2Si}^f(T) + 2G_{Mg}^{SER}(T) + G_{Si}^{SER}(T) \quad (16)$$

### 2.2.2. Amendments in COST507 Al database

In the present study the thermodynamic database for light non-ferrous alloys COST 507 was used [14]. COST-507 database contains thermodynamic data for the 19 elements most commonly encountered in Al alloys (Al, B, C, Ce, Cr, Cu, Fe, Li, Mg, Mn, N, Nd, Ni, Si, Sn, V, Y, Zn, Zr). According to the thermodynamic description in the COST507 database Mn does not enter in the description of the,  $\alpha$ -AlFeSi. Therefore this database was amended by recent thermodynamic descriptions, where a higher number of ternary and quaternary systems have been assessed [17]. In the present work the description of the  $\alpha$ -AlFeSi phase was amended in order to introduce Mn in the iron sublattice. This was accomplished by the introduction of the relevant thermodynamic quantities in the GES module of Thermo-Calc, where the composition and temperature dependence of the various thermodynamic parameters are stored.

### 2.2.3. Simulation of microsegregation

Microsegregation during the complex solidification process of Al-Mg-Si alloys is usually simulated by employing the Scheil-Gulliver model [18, 19] with the main assumption that the diffusion coefficients of the components in the liquid phase are infinitively fast whereas in the solid are zero. The assumption of negligible diffusion in the solid is acceptable due to the short local solidification time encountered in industrial direct-chill casting conditions. Along each step in the cooling process during solidification, local equilibrium is established at the solid/liquid interface and the composition of the solid and

liquid phase is given by the phase diagram. Also along each step the solid phase formed retains its composition and the liquid composition is always homogeneous. The basic derivation of the Scheil-Gulliver equation is presented below.

As mentioned above, the cooling during solidification is so fast that the solid composition cannot be homogenized by diffusion. The opposite is true for the liquid, where the composition is always homogeneous during the course of solidification. Consider Figure 2.1, which depicts three stages during solidification of a binary alloy. At the beginning, solidification starts at the liquidus temperature  $T_L$  and the first solid forms with a composition  $kC_0$ , where  $k$  is the partition coefficient ( $k=C_s/C_L$ ). At an intermediate temperature, the compositions of the solid and liquid phases at the interface are provided by the phase diagram as  $C_s$  and  $C_L$  respectively. While the liquid composition is homogenized to the value  $C_L$ , the solid composition varies from the initial  $kC_0$  to the value  $C_s$  at the interface.

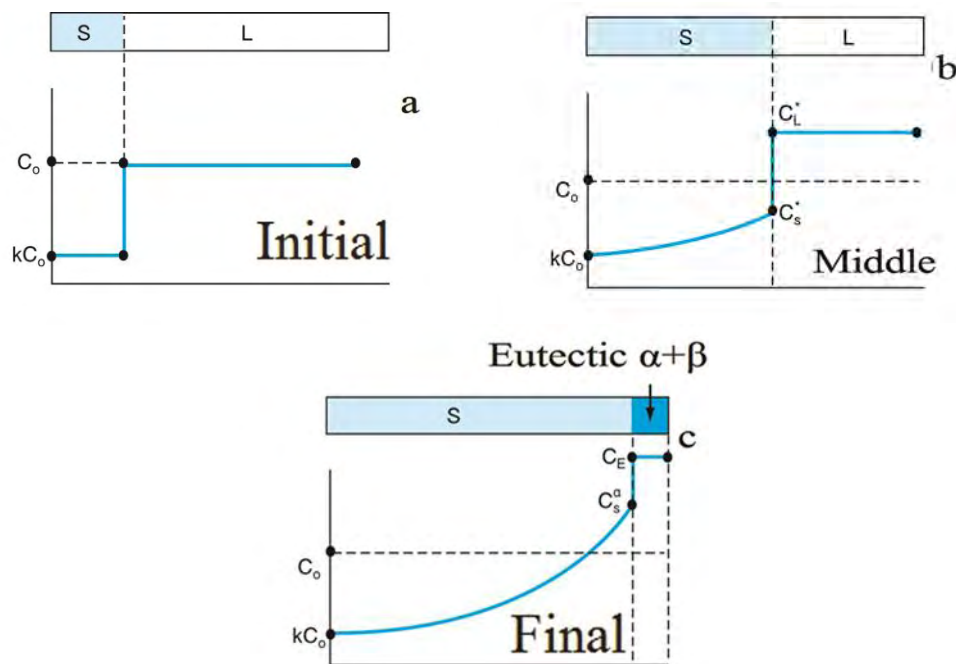


Figure 2.1: The three stages during solidification of a binary alloy

Due to the limited diffusion in the solid the average composition is lower than the composition it would have, if solidification proceeded under global thermodynamic equilibrium. It is possible to calculate the composition of the solid at the interface  $C_s$  as a function of the fraction solid  $f_s$  that has formed, by considering a mass balance in Figure 2.2.

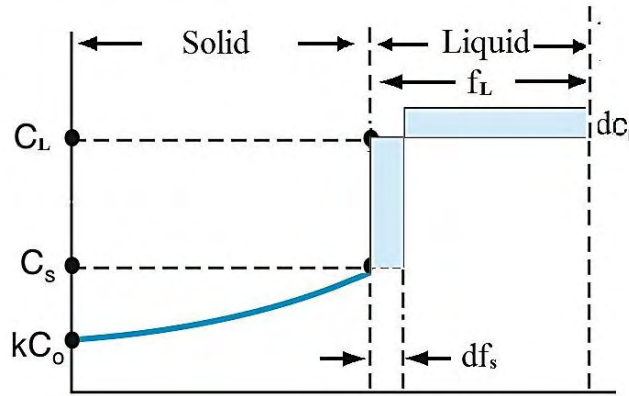


Figure 2.2: The composition of the solid at the interface  $C_s$  as a function of the fraction solid  $f_s$  that has formed, by considering a mass balance

When a small quantity of solid  $df_s$  forms, solute is rejected into the liquid and the liquid composition increases by  $dC_L$ . The mass balance gives

$$(C_L - C_s)df_s = (1 - f_s)dC_L \quad (17)$$

Rearranging terms and integrating we get

$$\int_0^{f_s} \frac{df_L}{(1 - f_s)} = \int_{C_o}^{C_L} \frac{dC_L}{C_L(1 - k)} \quad (18)$$

which leads to the Scheil-Gulliver equation

$$C_s = kC_o(1 - f_s)^{k-1} \quad (19)$$

As mentioned above, equation (19) predicts a lower composition in the solid than the equilibrium prediction, at the same time it predicts a higher fraction of remaining liquid to be solidified. Towards the end of solidification a rapid increase in the solute concentration of the liquid as well as an increase in the concentration of the solid to the value  $C_{sa}$  results in the formation of a non-equilibrium eutectic [20]. Therefore the Scheil-Gulliver equation

predicts a certain amount of eutectic even when the alloy solidifies as a single-phase alloy under thermodynamic equilibrium. This results in an especially complex as-cast microstructure in the 6xxx series alloys, because of the different sets of phases that can form in different areas of the billet due to differences in the cooling rate [21].

The Scheil-Gulliver equation (19) can be generalized to higher order multicomponent systems. The problem is treated with a special module (called the SCHEIL module) in the Thermo-Calc software. A simulation is conducted step by step along the cooling process, by decreasing the temperature (normally by 1°C in each step) below liquidus, and after each step the new liquid composition is used as the local overall composition at the next step. The simulation can handle cases of concurrent precipitation of two or more solid phases, such as eutectic reactions. It should be mentioned that other computational methods, which take into account macroscopic transport phenomena (melt flow and transport of crystals) have been developed for ternary alloys [22-23]. However these methods use locally linearized phase diagrams and do not benefit, at the moment, from the available thermodynamic databases.

With the SCHEIL module it is possible to calculate:

- the solidification path, i.e. the sequence of formation of solid phases during solidification
- the composition of solid as a fraction of solid formed during solidification, corresponding to the microsegregation of elements
- the fraction of solid phases vs fraction solid formed during solidification, corresponding to the microsegregation of phases
- the exact liquidus and solidus temperatures of the alloy

The development of microsegregation has been studied in four different variants of 6060 as well as in 6082, 6063 and 6005 alloys. Emphasis has been given on the effect of Mg and Si. These elements influence the strength properties and extrudability, which are important for the final performance. The chemical compositions of the alloys are listed in Table 2.1

Table 2.1: Chemical composition of alloys 6082, 6063, 6005, 6060 (in mass %)

| Alloy  | Al      | Mg   | Si   | Fe   | Mn   |
|--------|---------|------|------|------|------|
| 6082   | Balance | 0.63 | 0.9  | 0.2  | 0.45 |
| 6063   | Balance | 0.51 | 0.55 | 0.2  | 0.03 |
| 6005   | Balance | 0.48 | 0.68 | 0.15 | 0.2  |
| 6060_1 | Balance | 0.38 | 0.4  | 0.2  | 0.03 |
| 6060_2 | Balance | 0.48 | 0.4  | 0.2  | 0.03 |
| 6060_3 | Balance | 0.38 | 0.47 | 0.2  | 0.03 |
| 6060_4 | Balance | 0.48 | 0.47 | 0.2  | 0.03 |

### 2.3. Experimental procedures for model validation

The experimental procedures employed for the validation of simulation predictions are discussed in this section. Due to the difficulties encountered when measuring low volume fractions, the work was performed mainly on alloy 6082, which because of the higher alloy content, possessed a higher volume fraction of intermetallic phases. However metallographic results are presented for the 6060 and 6063 alloys as well.

The materials were received in the form of as-cast billets prepared with DC casting by the Aluminum of Greece (AoG). The diameter of the billet was 200mm and the solidification rate was  $2\text{mm s}^{-1}$ . The received billets were sectioned in transverse slices as shown in Figure 2.3. Then the samples of 10mm thickness were cut from approximately the middle of the billet's slice radius in order to avoid edge inhomogenities and other casting defects. The surface in a direction transverse to the billet axis was prepared for metallography.

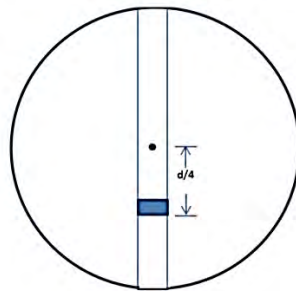


Figure 2.3: Transverse cross sections along the billet diameter

Specimen preparation included cutting and grinding with SiC papers rating 800, 1000, 2400 and 4000 grit for alloy 6063 and grinding on 500 grit SiC water – cooled paper, polish with 3 $\mu$ m and 1 $\mu$ m diamond paste and finally polished with 0.05 $\mu$ m Colloidal Silica for alloys 6060 and 6082. Polishing was performed with 3 and 1 $\mu$ m diamond paste followed by electro-polishing with Barkers reagent consisting of 10 millilitre fluoroboric acid (35 %) and 200 millilitre water. The microstructure was revealed after etching in Keller's solution, consisting of 0.5% HF in 50ml H<sub>2</sub>O in order to reveal and identify the intermetallic phases in the as-cast microstructure. Table 2.2 summarizes the procedure followed for metallographic preparation.

Table 2.2: Metallographic procedure for 6060, 6082 and 6063 alloys

| <b>Stages</b>   | <b>Alloy</b> |      |      |
|---|--------------|------|------|
|   | 6060         | 6082 | 6063 |
| <b>Grinding</b>   |              |      |      |
| SiC Papers (grit)   |              |      |      |
| 320   | x            | x    | x    |
| 500   |              | x    | x    |
| 1000  | x            | x    | x    |
| 2400  | x            | x    | x    |
| <b>Polishing</b>  |              |      |      |
| Diamond Paste   |              |      |      |
| 3 $\mu$ m   | x            | x    | x    |
| 1 $\mu$ m   | x            | x    | x    |
| Colloidal Silica  | x            | x    | x    |
| <b>Electro Polishing</b>  |              |      |      |
| stainless steel for<br>cathode;specimen is anode.<br>Anodize 40-80 s at approximately<br>0.2 A/cm <sup>2</sup> (1.3 A/in. <sup>2</sup> , or about 20<br>V dc). Check results on microscope<br>with crossed polarizers |              | x    | x    |
| <b>Chemical etching</b>   |              |      |      |
| Keller's  | x            |      |      |
| Modified Poultons   |              | x    |      |

The volume fractions of the Mg<sub>2</sub>Si and  $\alpha+\beta$  AlFeSi phases have been measured, through quantitative methods based on point counting, using 1000 grit on 10 sections

according to ASTM E-562 standard [24]. Processing has been performed using Photoshop and Image J image analysis software. The results were then compared with the corresponding results of the Scheil simulation of the solidification process of 6082 alloy. The following methodology was applied: first the phases were identified using SEM combined with EDS analysis and then a correspondence between SEM and optical microscopy was established in order to identify the phases in optical micrographs. This methodology enabled the use of a point counting method in order to determine the volume fractions of phases, using a high number of metallographic sections at the lowest magnification possible in order to get the most representative microstructure. Solute microsegregation has been also experimentally determined by SEM/EDX analysis.

## **2.4. Results and Discussion**

### **2.4.1. Equilibrium calculations**

Equilibrium calculations are presented in this section, which aim at identifying the major phases and their stability limits in the alloys. For the 6060 alloy, the Si isopleth section for composition 0.48Mg, 0.03Mn and 0.2Fe (in mass %), is depicted in Figure 2.4a. Similarly the Mg isopleth for 0.4Si, 0.03Mn and 0.2Fe (in mass %) is depicted in Figure 4b. The  $\text{Mg}_2\text{Si}$  phase is stable bellow 500°C. The  $\alpha\text{-AlFeSi}$  phase is the first phase stabilized bellow the liquidus temperature. The range of stability of  $\alpha\text{-AlFeSi}$  extends to lower temperatures depending on Mg content. On the contrary Si stabilizes the  $\beta\text{-AlFeSi}$  phase. Additionally the isopleths of Figure 2.4 indicate that transformation of  $\alpha$  to  $\beta\text{-AlFeSi}$  takes place as the temperature drops below the solidus. For this reason as mentioned above, a kinetic calculation, described in section 4.4.4, has been performed in order to determine the amount of  $\beta\text{-AlFeSi}$  phase, which forms after solidification.

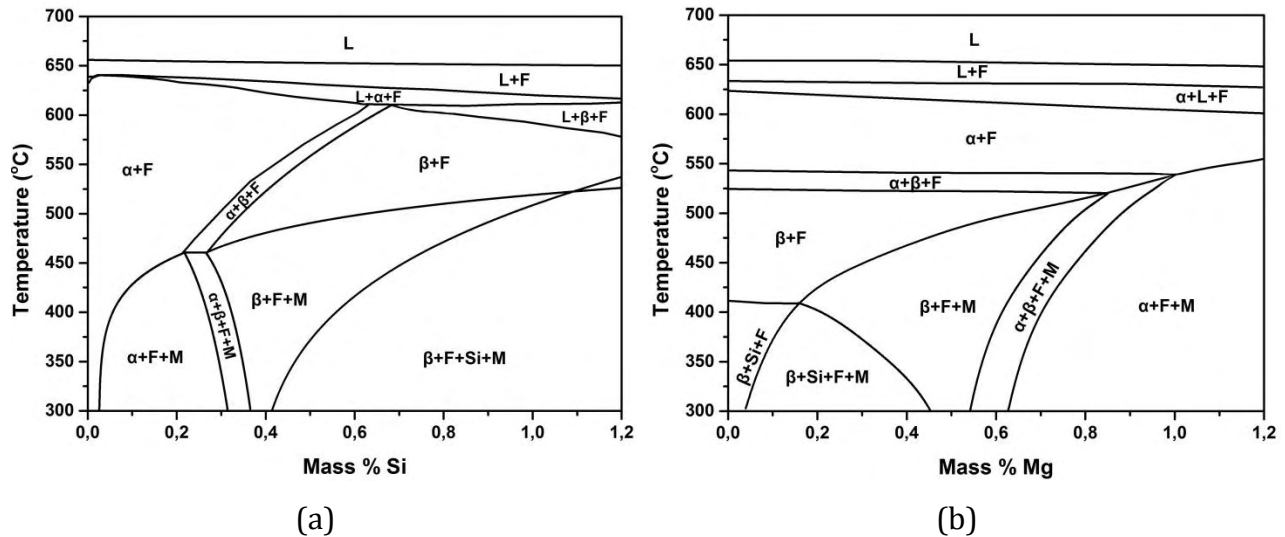


Figure 2.4:(a) Si isopleth for 0.45Mg, 0.03Mn and 0.2 Fe (mass%) and (b) Mg isopleth for 0.4Si, 0.03Mn and 0.2 Fe (L=liquid, F=FCC,  $\alpha$ = $\alpha$ -AlFeSi,  $\beta$ = $\beta$ -AlFeSi, M= $Mg_2Si$ )

An isothermal section of the Al-Mg-Si-Fe-Mn system at 300°C, and for 0.2Fe-0.03Mn (mass %) is shown in Figure 2.5. In agreement to the above observations, Mg stabilizes the  $\alpha$ -AlFeSi phase up to 0.8 mass % Si and Si stabilizes the  $\beta$ -AlFeSi phase, which forms even for low concentrations of Mg and Si.

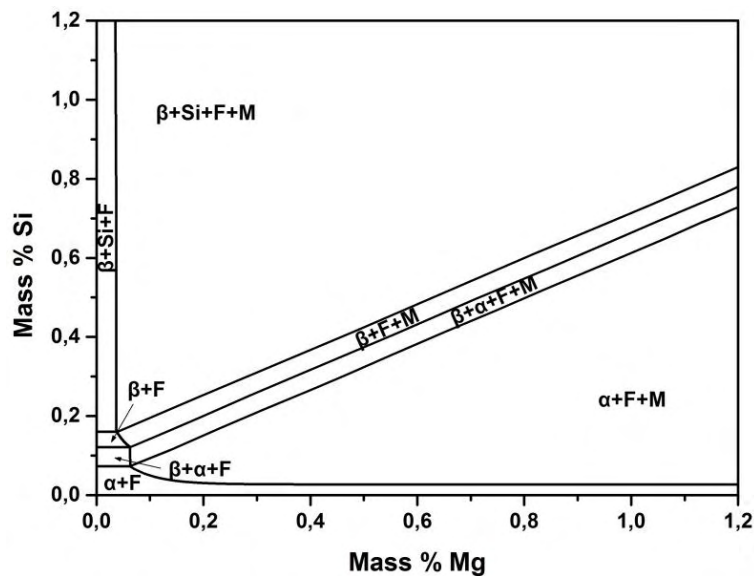


Figure 2.5: Isothermal section of Al-Mg-Si with 0.2Fe-0.03Mn (mass %) at 300°C, (L=liquid, F=FCC,  $\alpha$ = $\alpha$ -AlFeSi,  $\beta$ = $\beta$ -AlFeSi, M= $Mg_2Si$ )



## 2.4.2. Scheil microsegregation simulations

Typical Scheil solidification paths, for the studied alloys are shown in Figure 2.6a-d as temperature vs mass fraction solid. The phase sequence during solidification is FCC→ $\alpha$ -AlFeSi→ $\beta$ -AlFeSi→ $Mg_2Si$ →Si (diamond). The arrows depict the temperature and the mass fraction of solid where each phase starts to form. Solidus temperatures for these alloys were calculated and results are depicted in Figure 2.7.

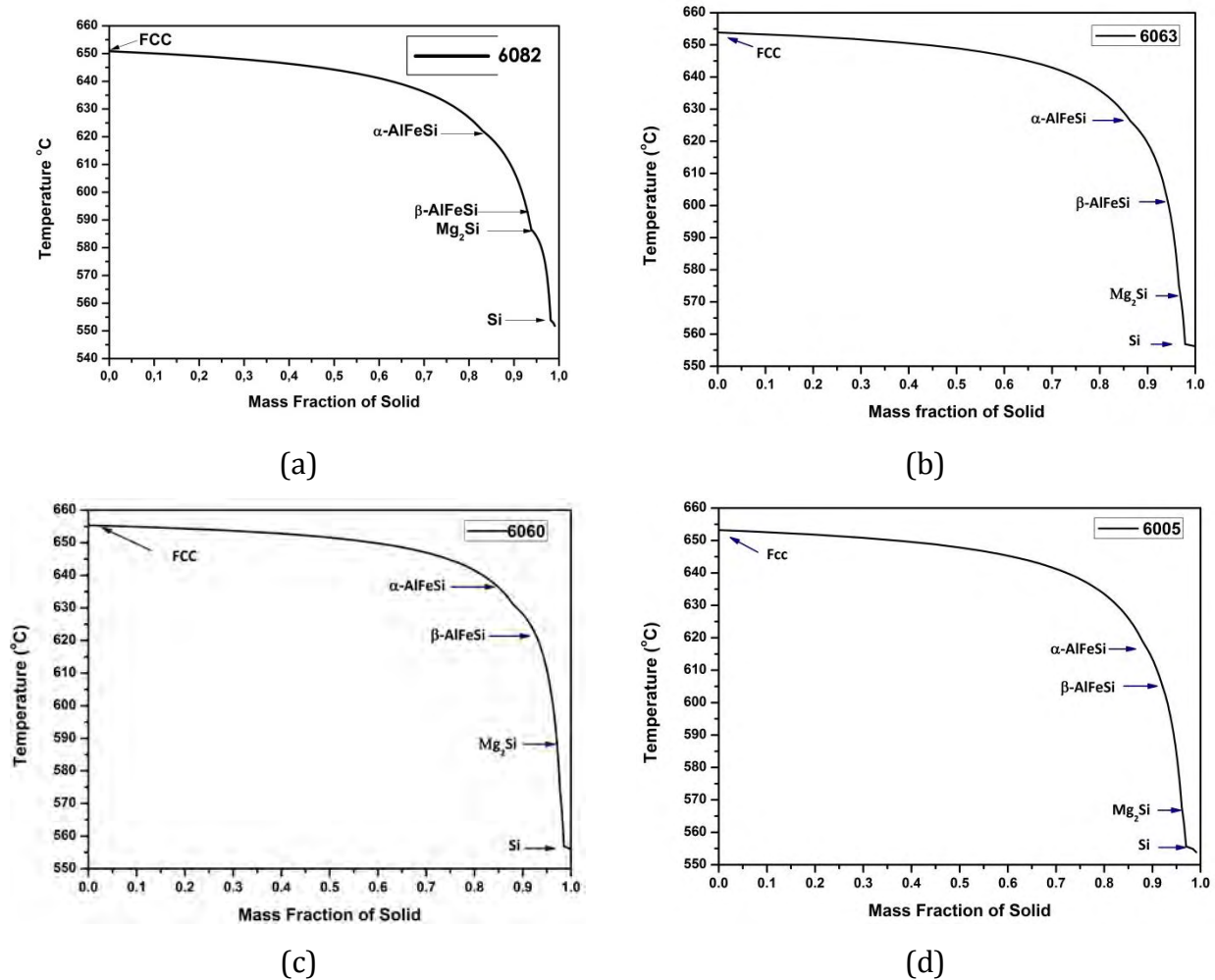


Figure 2.6: Typical solidification paths for a)6082, b)6063, c)6005, d)6060

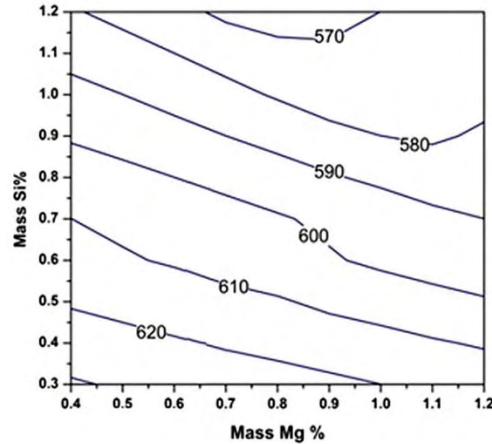


Figure 2.7: Calculated Solidus temperatures

The mole fraction of phases, formed during solidification, was calculated as a function of temperature and is shown in Figure 2.8 for 6082 alloy. Formation of  $\alpha$ -AlFeSi starts at 622°C while further formation of  $\alpha$ -AlFeSi stops, when the  $\beta$ -AlFeSi starts to form at 588°C. The  $\text{Mg}_2\text{Si}$  phase starts to form at 585°C and continuous to grow simultaneously with the  $\beta$ -AlFeSi phase until the quaternary eutectic temperature (554°C) is reached and the remaining liquid transforms to a mixture of FCC,  $\beta$ -AlFeSi,  $\text{Mg}_2\text{Si}$  and Si.

The phase fractions in the as-cast microstructure are  $4.14 \times 10^{-3}$   $\alpha$ -AlFeSi,  $7.16 \times 10^{-4}$   $\beta$ -AlFeSi,  $5.32 \times 10^{-3}$   $\text{Mg}_2\text{Si}$  and  $9.18 \times 10^{-4}$  Si-diamond.

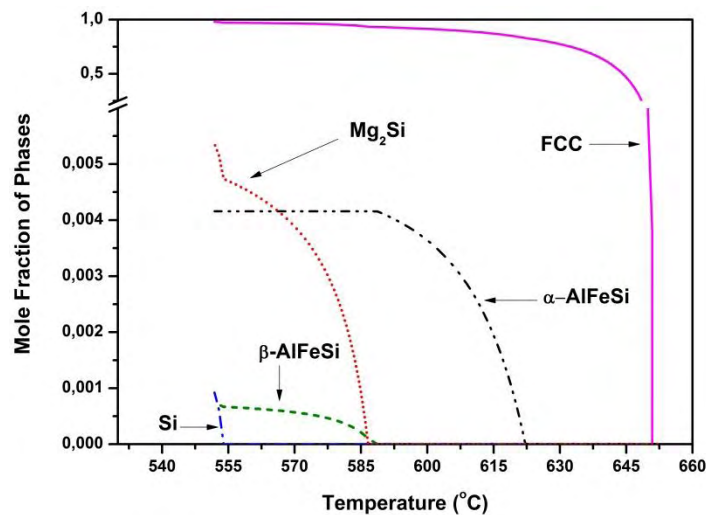


Figure 2.8: Mole fraction of phases as a function of temperature during solidification of Al-0.38Mg-0.4Si-0.2Fe-0.03Mn (mass%)

The above phases are not distributed uniformly in the microstructure but segregate to regions where the liquid solidifies last, i.e. close to grain boundaries. This phase segregation is depicted in Figure 2.9a, which gives the mole fraction of all phases vs fraction solid (FCC matrix is excluded). It is seen that the  $\alpha$ -AlFeSi phase forms above 85 % solidification while all other phases form above 95 % solidification. This means that the intermetallic phases form at the secondary dendrite boundaries towards the end of solidification. Accordingly the microsegregation of the alloying elements in the FCC matrix follows a similar trend, i.e. increase towards the end of solidification as shown in Figure 2.9b. The drop in the concentration profile of Mg and Fe is attributed to the formation of  $Mg_2Si$  and iron intermetallics respectively.

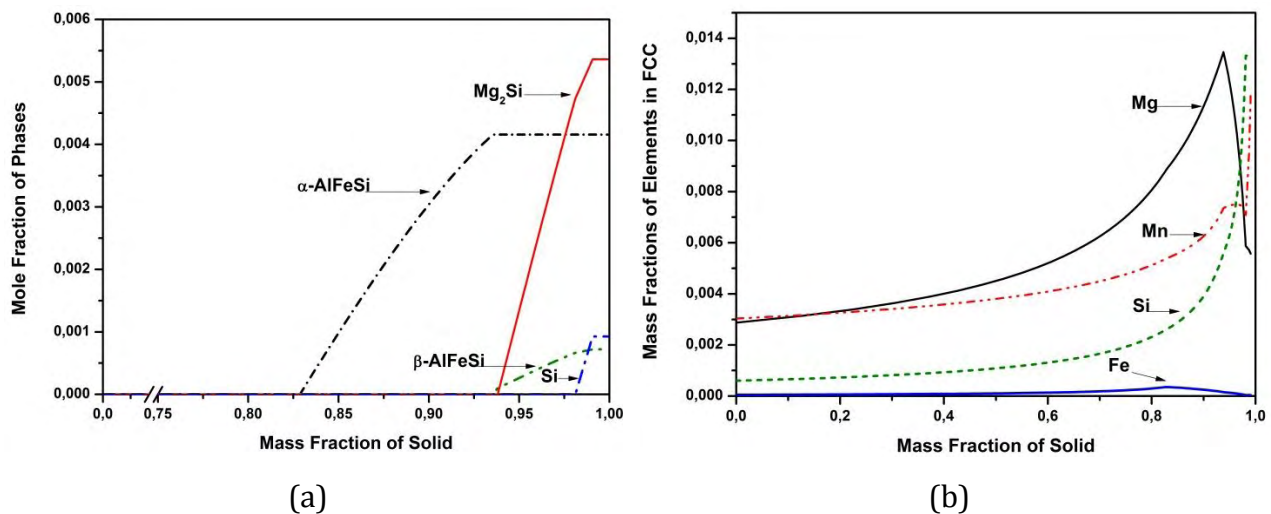


Figure 2.9: Microsegregation of phases (a) and microsegregation of alloying elements (b) of Al-0.38Mg-0.4Si-0.2Fe-0.03Mn (mass%) alloy during solidification

### 2.4.3. Parametric study on 6060 alloy

A parametric study was performed for the four variants of alloy 6060, with the compositions given in Table 1. Both variants, 6060\_1 and 6060\_3, contain 0.38%Mg but with 0.4 and 0.47% Si respectively, while both variants 6060\_2 and 6060\_4 contain 0.48%Mg with 0.4 and 0.47%Si respectively.

Segregation of phases for 6060\_1 and 6060\_3 is depicted in Figure 2.10, while for the 6060\_2 and 6060\_4 in Figure 2.11. The phases depicted are  $\alpha$ -AlFeSi in (a),  $\beta$ -AlFeSi in (b),  $Mg_2Si$  in (c) and Si-diamond in (d).

It is evident that the larger differences appear in the fraction of the  $\beta$ -AlFeSi phase, where a higher fraction is formed in the alloys containing a higher amount of Si, i.e. in alloys 6060\_3 and 6060\_4. This is due to the stabilizing effect of Si on the  $\beta$ -AlFeSi phase. A lower amount of  $\beta$ -AlFeSi is formed in the high Mg alloys 6060\_2 and 6060\_4. At the same time the amount of the strengthening phase is higher in the high Mg alloys 6060\_2 and 6060\_4. Therefore it is concluded that Mg has a destabilizing effect on the extrudability-limiting phase  $\beta$ -AlFeSi, while it increases the amount of the strengthening phase  $Mg_2Si$ .

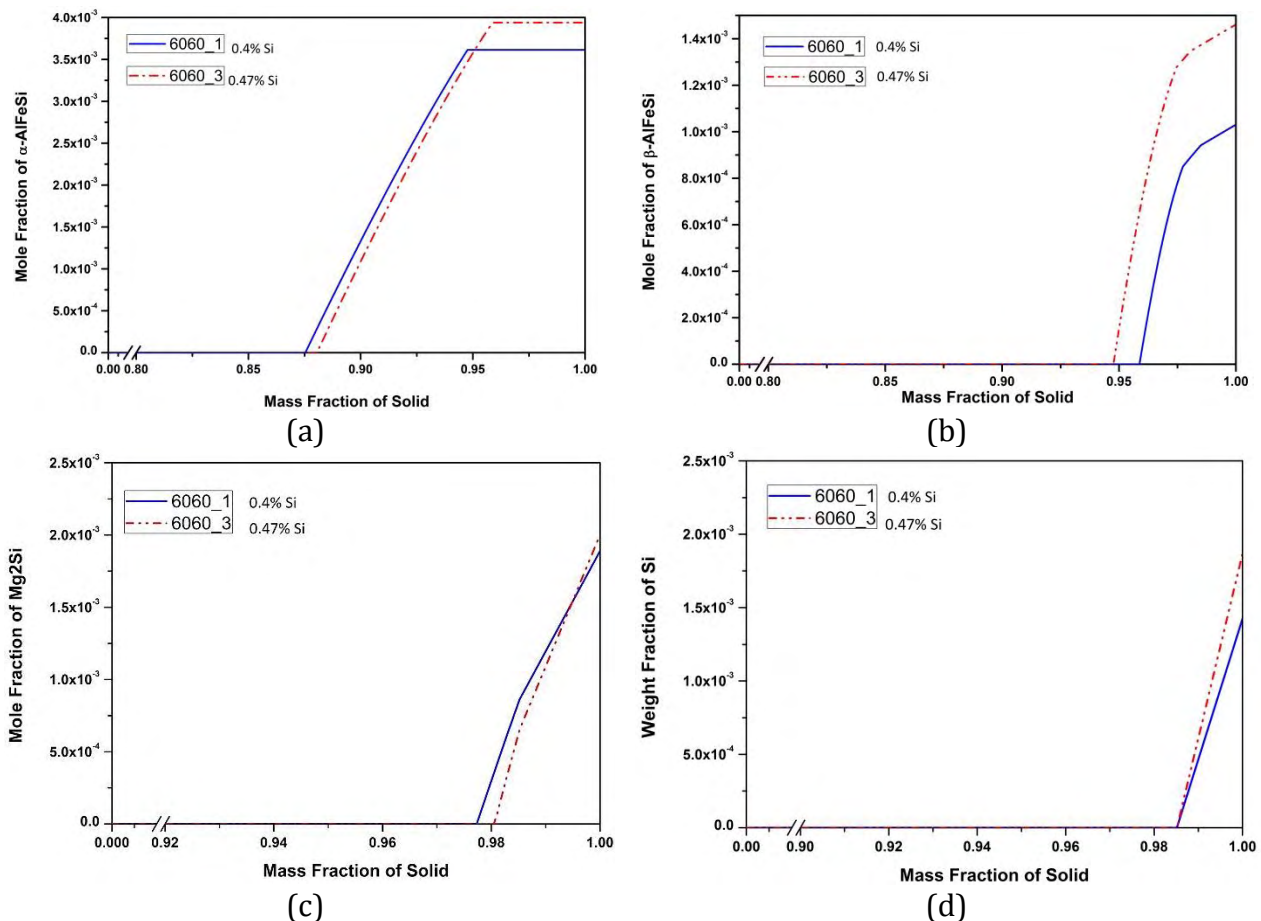
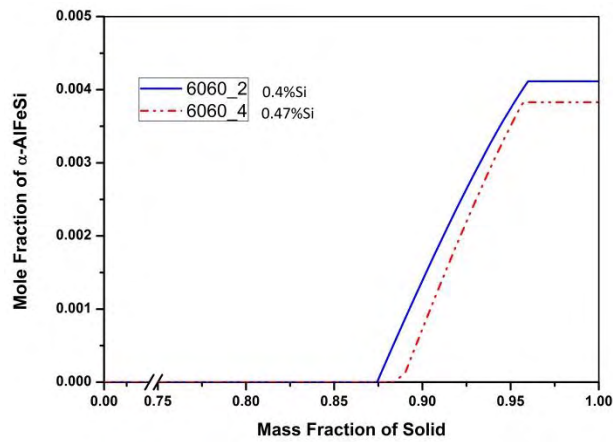
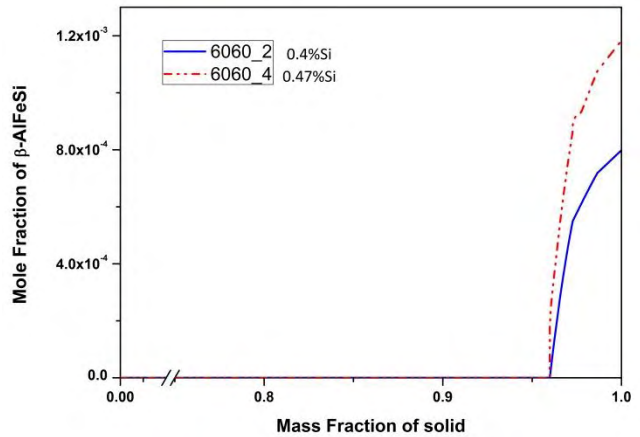


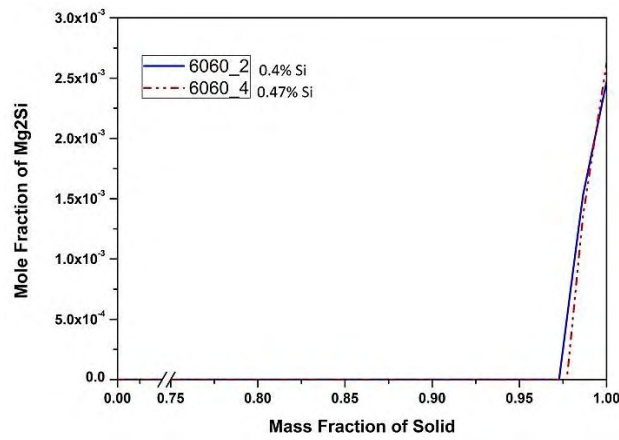
Figure 2.10: Segregation of phases for 6060\_1 and 6060\_3 a)  $\alpha$ -AlFeSi, b)  $\beta$ -AlFeSi, c)  $Mg_2Si$ , d) Si (Diamond)



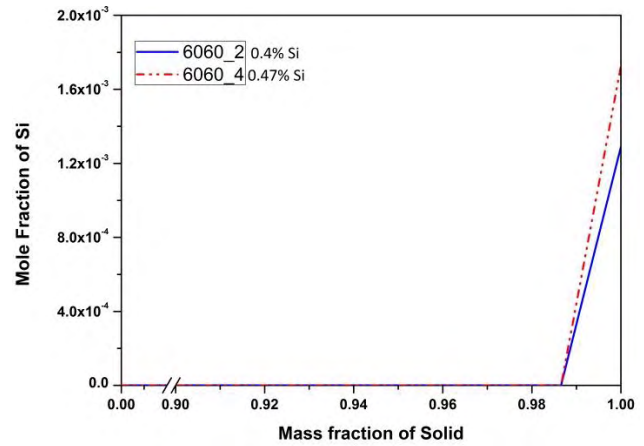
(a)



(b)

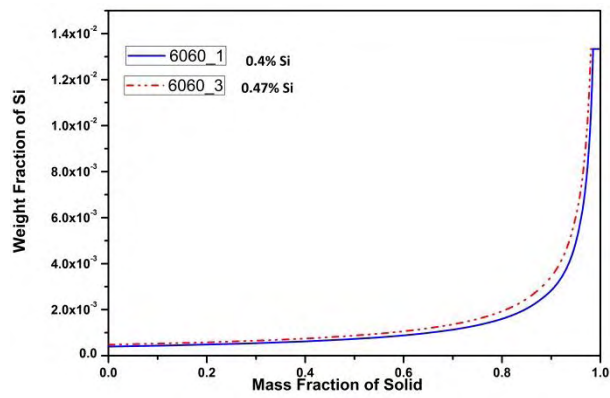


(c)

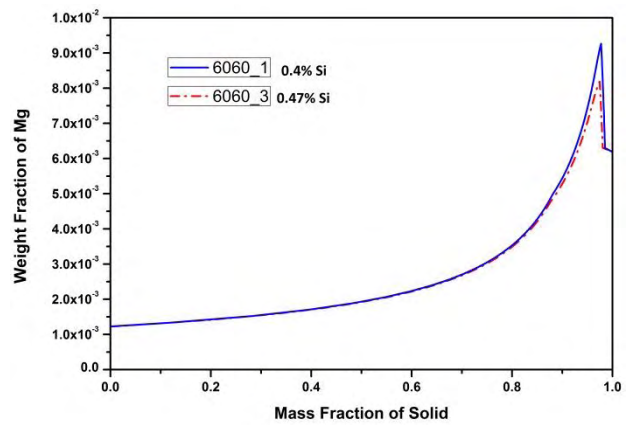


(d)

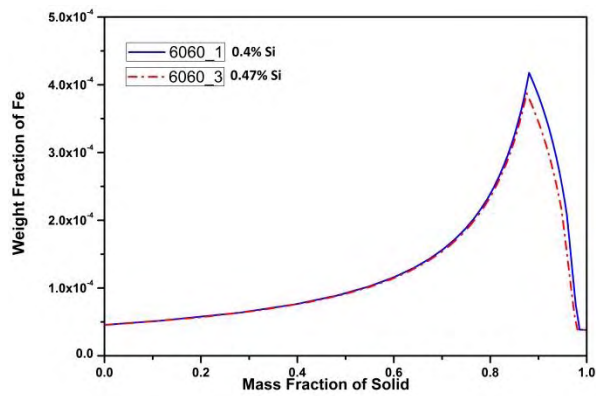
Figure 2.11: Segregation of phases in 6060-2 and 6060\_4 alloys, a)  $\alpha$ -AlFeSi, b)  $\beta$ -AlFeSi, c)  $Mg_2Si$ , d) Si (Diamond)



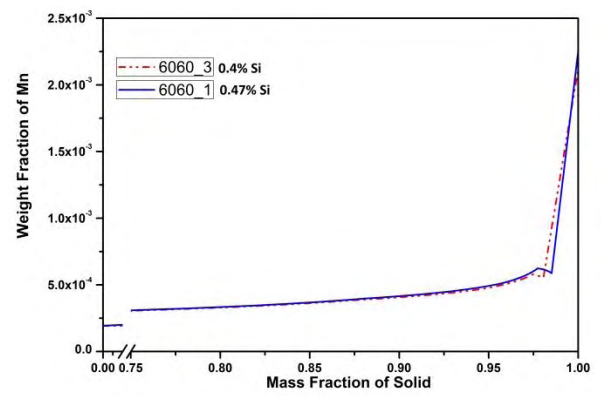
(a)



(b)



(c)



(d)

Figure 2.12: Segregation of elements in 6060\_1 and 6060\_3 alloys a) Si, b)Mg, c)Fe, d)Mn



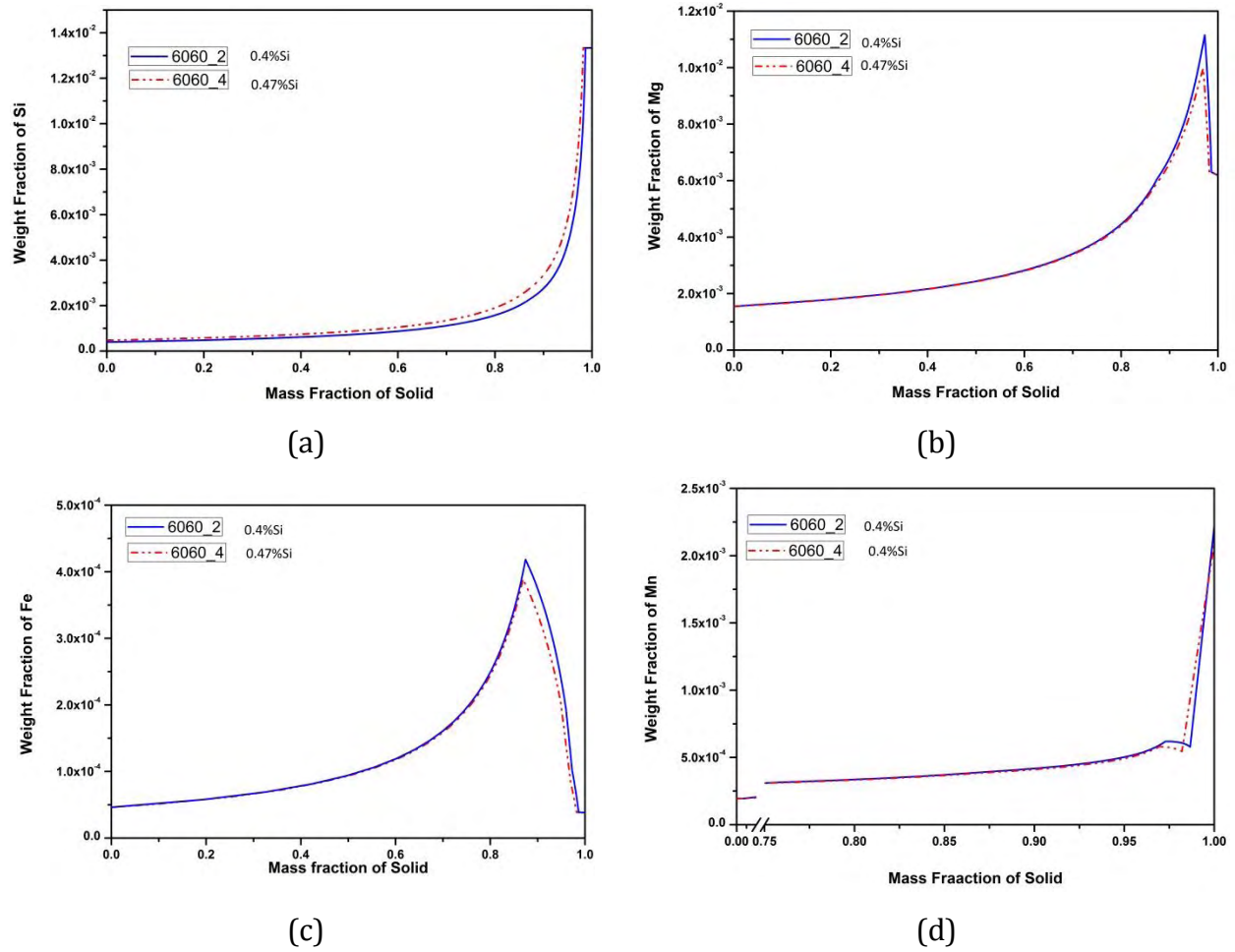


Figure 2.13: Segregation of elements in 6060\_2 and 6060\_4 alloys a) Si, b)Mg, c)Fe, d)Mn

Segregation of elements for 6060\_1 and 6060\_3 is depicted in Figure 2.12, while for the 6060\_2 and 6060\_4 in Figure 2.13. The elements depicted are Si in (a), Mg in (b), Fe in (c) and Mn in (d). Elemental microsegregation is evident in all cases; however the elements do not exhibit the same degree of microsegregation. A microsegregation index  $\delta_i$  is defined as

$$\delta_i = \frac{C_M - C_o}{C_o} \quad (20)$$

where  $C_M$  is the maximum composition in the segregation profile and  $C_o$  is the composition of the first solid to form (at zero weight fraction solid). The calculated values of the segregation index appear in Table 2.3. The element possessing the highest

microsegregation is Mn with larger microsegregation index compared to the other elements. Si and Mg have a higher diffusion coefficient in Al and therefore should homogenize easier than Fe and Mn.

Table 2.3: Segregation index for the 6060 alloy variants

| <b>Alloy</b> | <b><math>\delta_{Fe}</math></b> | <b><math>\delta_{Si}</math></b> | <b><math>\delta_{Mg}</math></b> | <b><math>\delta_{Mn}</math></b> |
|--------------|---------------------------------|---------------------------------|---------------------------------|---------------------------------|
| 6060_1       | 8.08                            | 8.29                            | 7.33                            | 10,7                            |
| 6060_2       | 8.08                            | 8.29                            | 5,45                            | 15,5                            |
| 6060_3       | 6.6                             | 8.29                            | 5,58                            | 10.7                            |
| 6060_4       | 6.6                             | 8.19                            | 4,88                            | 9,84                            |

#### 2.4.4. Transformation of $\alpha$ to $\beta$ -AlFeSi after solidification

The Scheil simulation described above defines the phase fractions present in the microstructure at the end of solidification. According to the isopleth sections in Figure 2.4 transformation of  $\alpha$  to  $\beta$ -AlFeSi takes place below the solidus temperature during equilibrium cooling. However, taking into account the high cooling rates of the solidified ingots, following the direct-chill casting operation, it should be evaluated whether this transformation produces any appreciable amount of  $\beta$ -AlFesi phase. A kinetic simulation using the DICTRA computational kinetics software was performed for the 6082 alloy. The geometric model used in a previous work [25] was employed and is shown in Figure 2.14. The calculation domain consists of two regions. The first region corresponds to the fcc matrix phase while the  $\alpha$ -AlFeSi is taken as a dispersed spheroidal phase. The second region was attached to the right of the first region and corresponds to the  $\beta$ -AlFeSi phase. The width of the fcc region was taken to be one half of the mean secondary dendrite arm spacing (10  $\mu$ m) and the width of the  $\beta$ -AlFeSi corresponded to the mole fraction of the  $\beta$ -AlFeSi as calculated by the Scheil simulation.



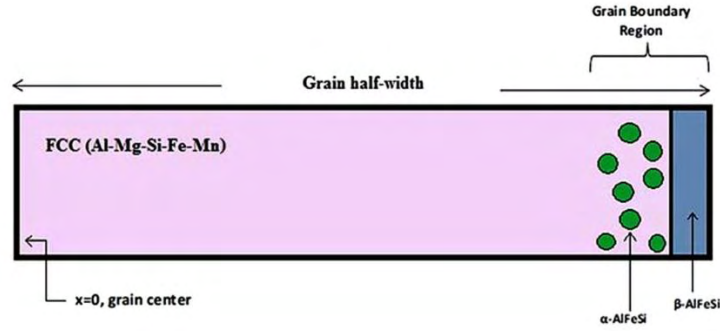


Figure 2.14: The geometric model for the kinetic simulation using the DICTRA computational kinetics software performed for the 6082 alloy

For the composition of the 6082 alloy, the mole fraction of  $\beta$ -AlFeSi corresponds to a width of the  $\beta$ -AlFeSi region equal to  $0.0111 \mu\text{m}$ . The temperature during the simulation was considered to drop from 600 to 200 °C in 1 h corresponding to a cooling rate of  $0.11\text{Ks}^{-1}$ . In order to take into account the impeding effect of the dispersed  $\alpha$ -AlFeSi phase on the diffusivities of the elements in the fcc matrix phase, a labyrinth factor [26], taken equal to the volume fraction of the  $\alpha$ -AlFeSi phase [27] was employed. The result of the simulation is given in Figure 2.15 which shows the position of fcc/ $\beta$ -AlFeSi interface as a function of simulation (cooling) time.

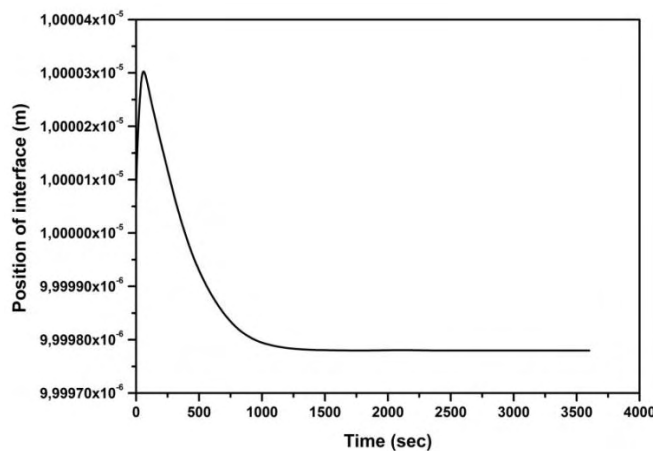


Figure 2.15: The position of fcc/ $\beta$ -AlFeSi interface as a function of simulation (cooling) time

The final position of the interface at  $9.99977 \mu\text{m}$ , to the left of the initial position ( $10\mu\text{m}$ ), corresponds to an increase of the volume fraction of  $\beta$ -AlFeSi phase by 2.07 % of the amount of  $\beta$ -AlFeSi formed during solidification. This value is considered negligible and

therefore the amount of the  $\beta$ -AlFeSi phase, used for the experimental validation and the construction of the maps in Section 4.7, was taken directly from the Scheil simulations.

## 2.5. Experimental validation

The purpose of this section is to provide the necessary experimental data, regarding phase identification and phase fractions, for the validation of the computational methodology used in this work. As mentioned above, the validation was performed on alloy 6082, since it exhibited the largest fraction of intermetallics due to its higher alloy content.

The as-cast microstructure of 6082 is depicted in the SEM micrograph Figure 2.16a-c. The EDS signal from areas 1 and 2 consisted of Mg and Si indicating that this phase is  $\text{Mg}_2\text{Si}$ . The signal from area 3 consisted of Al, Fe, Si and Mn indicating that it is the  $\alpha$ -AlFeSi phase, which contains Mn. The signal from area 4 consisted of Al, Fe and Si (without Mn) and was identified as  $\beta$ -AlFeSi. In order to further verify the phase identification, the composition of the  $\alpha$ -AlFeSi was determined quantitatively.

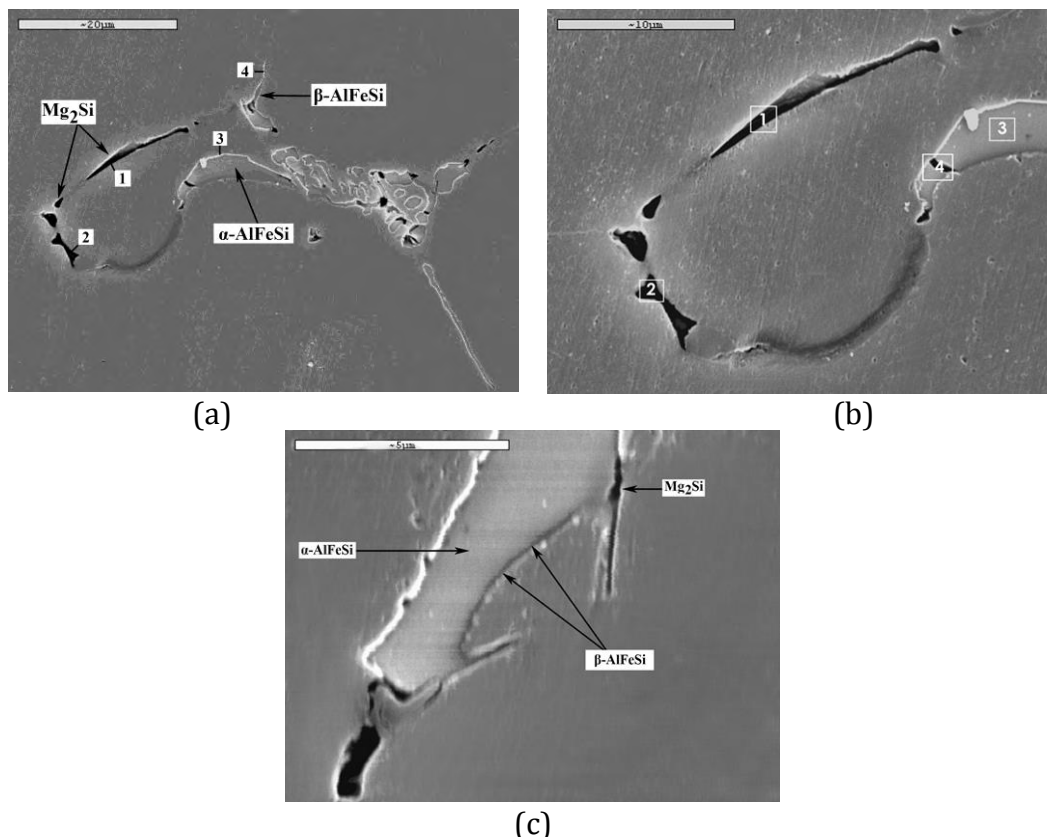


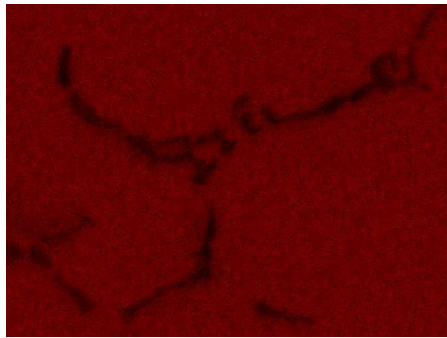
Figure 2.16: The as-cast microstructure of 6082 alloy as observed in the SEM

It should be mentioned that the interaction volume of the EDS measurement performed in this work was about  $1\mu\text{m}^2$  while the average size of  $\alpha\text{-AlFeSi}$  particles on which the EDS signal was taken was  $20\text{-}30\mu\text{m}^2$ . The results are listed in Table 2.4 and compared with measured literature data. The measured composition of  $\alpha\text{-AlFeSi}$  lies within the range reported in the literature and, therefore, the phase can be identified as  $\alpha\text{-AlFeSi}$ .

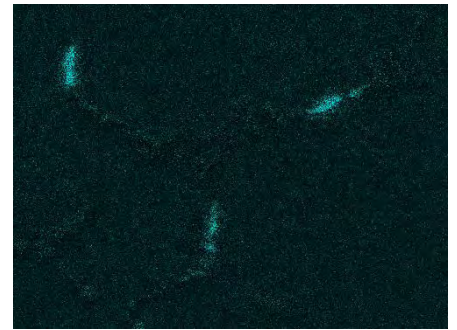
Table 2.4: Chemical composition of  $\alpha\text{-AlFeSi}$  phase (mass %)

| Phase                  | Si       | Fe       | Mn      | Reference |
|------------------------|----------|----------|---------|-----------|
| $\alpha\text{-AlFeSi}$ | 8-12     | 11-13    | 14-20   | [1]       |
|                        | 10 -12   | 10-15    | 15-20   | [28]      |
|                        | 5.5-6.5  | 5.1-27.9 | 14-24   | [29]      |
|                        | 5-7      | 10-13    | 19-23   | [30]      |
|                        | 6.3-11.5 | 7.4-14.3 | 5.5-9.8 | This work |

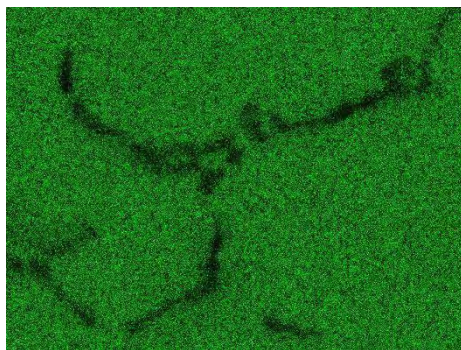
Furthermore elemental area mapping in 6082 alloy was performed in order to identify the presence of the elements in the observed intermetallic phases. The elemental map images in Figure 2.17 depict the spatial distribution of elements, specifically Al, Mg, Si, Fe, and Mn. In this way it is possible to identify phases in the microstructure that would be difficult to identify by optical microscopy. Figure 2.17 depicts a SEM micrograph in the centre with corresponding EDS maps for Al in (a), Si in (b), Mg in (c), Fe in (d) and Mn in (e). The EDS analysis indicates that the black oval particles are  $\text{Mg}_2\text{Si}$  strengthening phase because of the presence of Mg and Si element (Figures 2.17b-c) and absence of Al signal (Figure 2.17a). Besides the  $\text{Mg}_2\text{Si}$  phase other Si containing phases are the intermetallics  $\alpha$  and  $\beta\text{-AlFeSi}$ . The low solid solubility of Fe in aluminum leads to the formation of the above-mentioned intermetallics and this has been confirmed in Figure 2.17d with a strong iron signal. The presence of Mn in Figure 2.17e indicates that this phase is the  $\alpha\text{-AlFeMnSi}$  phase.



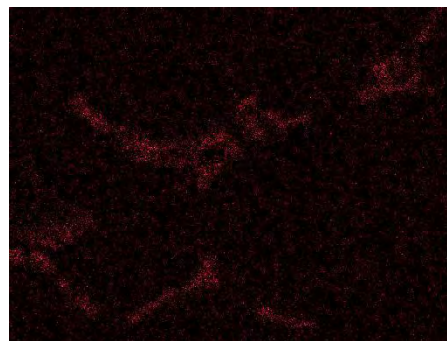
(a)



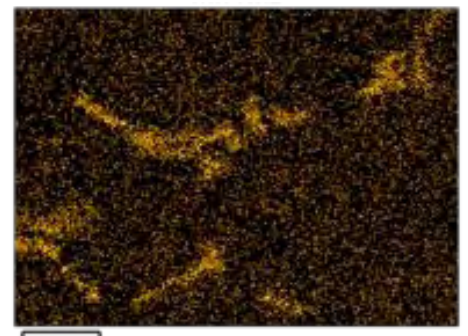
(b)



(c)



(d)



(e)

Figure 2.17: Elemental area mapping (SEM/EDS) in 6082 alloy a) Al, b) Si, c) Mg, d) Fe, e) Mn

Besides the identification of phases in the SEM, it is important to validate the matrix composition, adjacent to the intermetallics, close to the boundary. The results are shown in Figure 2.18, with a SEM microstructure in (a), the Scheil simulation for the microsegregation of elements in (b) and an EDS spectrum from the matrix region adjacent to the boundary in (c). The measured compositions are compared against the calculated data from the Scheil simulation in Table 2.5. The agreement between measured and calculated compositions is considered satisfactory.

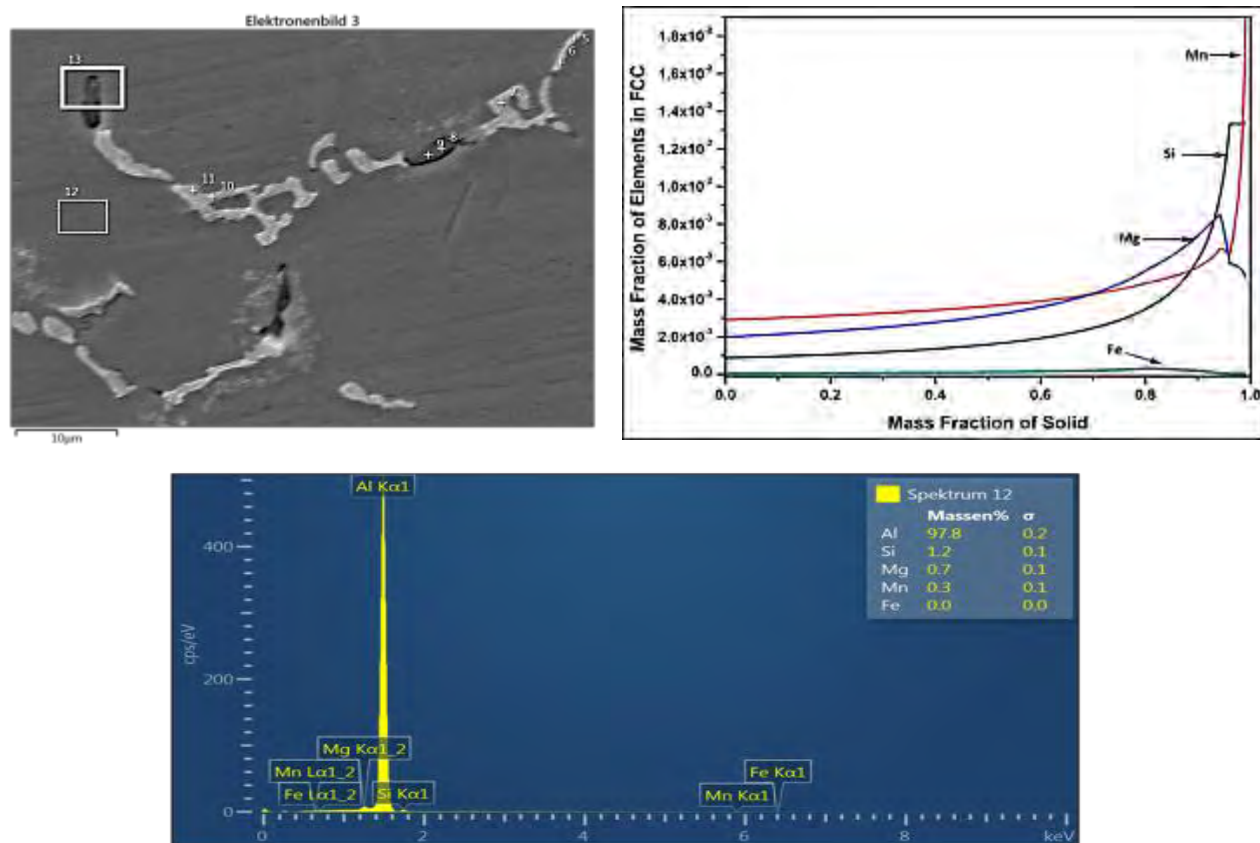


Figure 2.18: Matrix composition adjacent to boundary intermetallics: (a) SEM micrograph, (b) Scheil microsegregation profile and (c) EDS signal

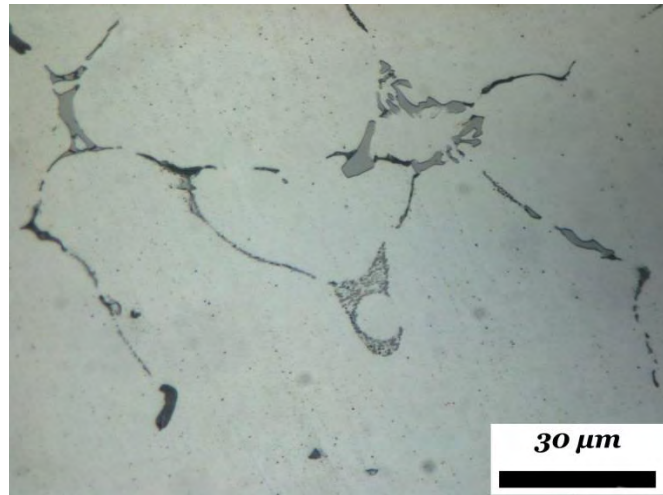
Table 2.5: Comparison between calculated and measured (EDS) matrix composition adjacent to boundary intermetallics

| <b>Matrix composition adjacent to boundary</b> |                      |                   |
|--|----------------------|-------------------|
| <b>Element</b>                                 | Measured Mass<br>(%) | Calculated<br>(%) |
| <b>Al</b>                                      | 97.8                 |                   |
| <b>Si</b>                                      | 1.2                  | 1.32              |
| <b>Mg</b>                                      | 0.7                  | 0.59              |
| <b>Mn</b>                                      | 0.3                  | 0.5               |
| <b>Fe</b>                                      | 0                    | 0                 |

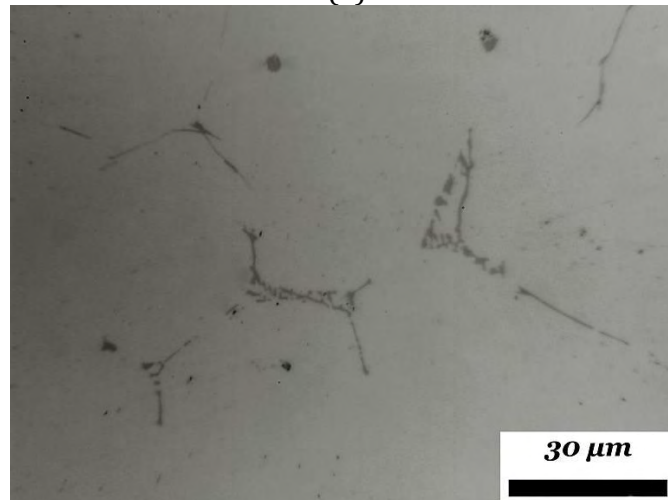
Using the procedure outlined in the experimental procedures section, the SEM phase identification was correlated with optical micrographs. Typical microstructures are depicted in Figure 2.19a-c for 6082, 6063 and 6060 respectively. The microstructure consists of Al-rich solid solution dendrites while the intermetallic phases are segregated at the secondary dendrite arm boundaries. These phases are identified as  $\text{Mg}_2\text{Si}$  (black),  $\alpha\text{-AlFeSi}$  (grey plate-like with rounded edges) and  $\beta\text{-AlFeSi}$  (grey plate-like). These observations are also in very good qualitative agreement with available metallographic observations in the literature [2, 31].

In Figure 2.20 6082 alloy is depicted and the morphology of the intermetallic compound  $\alpha\text{-AlFeSi}$  appears with a typical lamellar morphology known as “Chinese-script” structure.

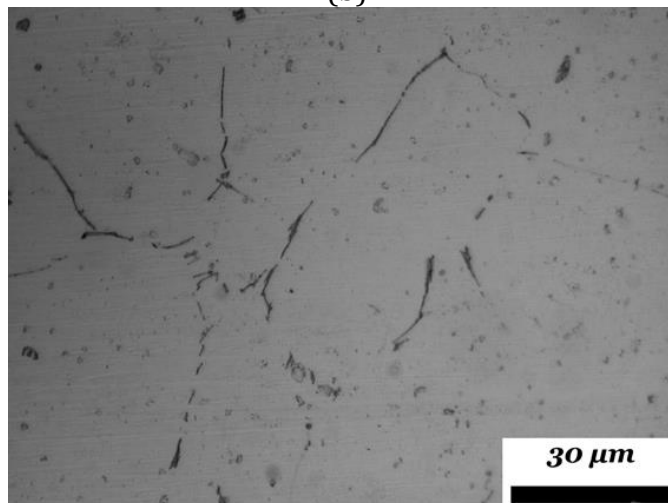




(a)



(b)



(c)

Figure 2.19: Typical microstructure of alloys (a) 6082, (b) 6063 and (c) 6060

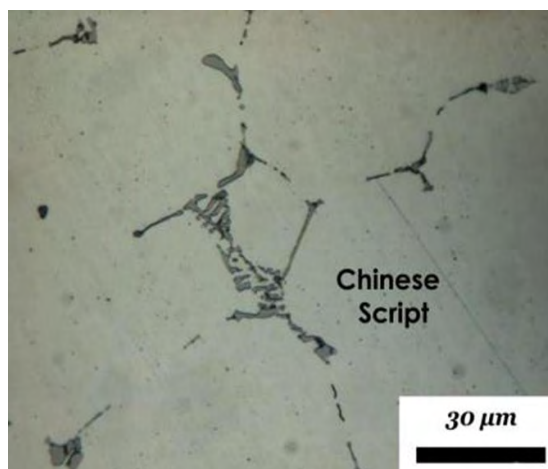


Figure 2.20: Typical morphology of intermetallic  $\alpha$ -AlFeSi in 6082 known as “Chinese-script”

Further metallographic examination has been performed in the 6082 alloy. The Scheil simulation on 6082 (Figure 2.6a) indicated that the last liquid solidifies by a quaternary eutectic consisting of FCC +  $\beta$ -AlFeSi +  $Mg_2Si$  + Si at 544°C. The amount of this quaternary eutectic is small compared with the primary phases and forms when less than 10% liquid remains, in agreement with ref. [31]. The quaternary eutectic constituent is depicted in Figures 2.21a-b.

The presence of spherical  $Mg_2Si$  and eutectic phases are also shown in Figure 2.21b.

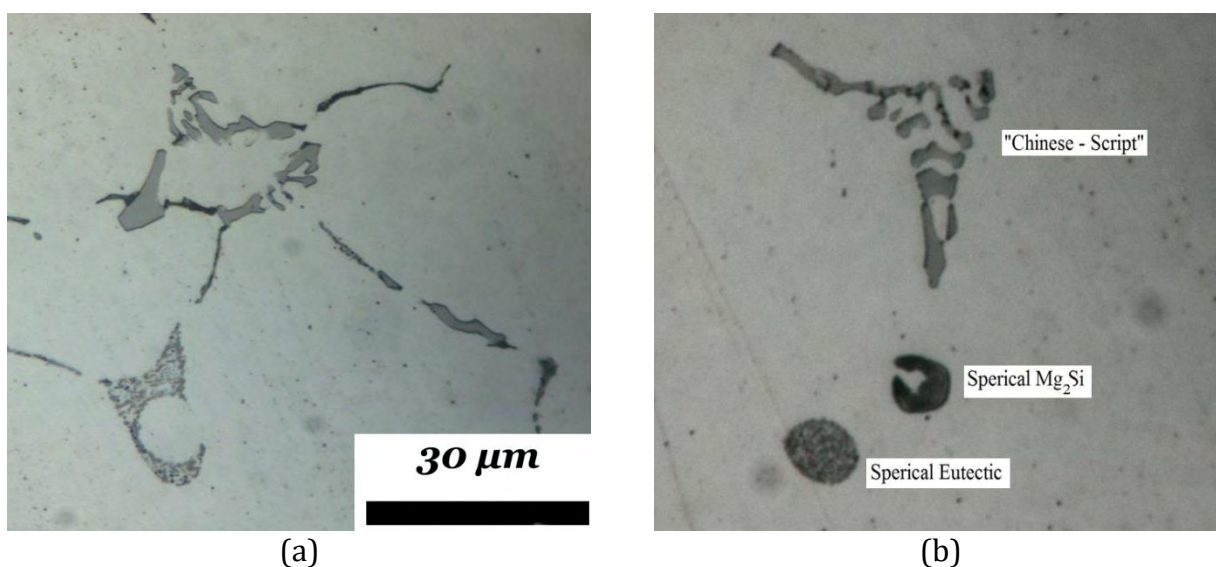


Figure 2.21: The (a) quaternary eutectic structure and spherical  $Mg_2Si$  and eutectics of 6082 alloy in as-cast condition



Following phase identification, the measurement of phase fractions was performed by quantitative metallography using the image analysis software Image –J. Low magnification micrographs were selected in order to have the most representative microstructure. In Figure 2.22, representative pairs of micrographs (left) and Image-J displays (right) are shown.

Scheil calculations of phase fractions are compared with experimental measurements in Table 2.6 for  $\alpha$ -AlFeSi,  $\beta$ -AlFeSi,  $Mg_2Si$  and quaternary eutectic (FCC +  $Mg_2Si$  +  $\beta$ -AlFeSi + Si). For the case of iron intermetallics the sum of  $\alpha$  and  $\beta$ -AlFeSi is compared with experimental data. Taking into account the experimental error involved when measuring low volume fractions, the agreement between the Scheil simulation predictions and the experimental measurements is considered satisfactory. Therefore computed fractions from the Scheil simulations can be used for the phase fraction mapping of intermetallic phases in the as-cast microstructure. This is discussed in the following sections.

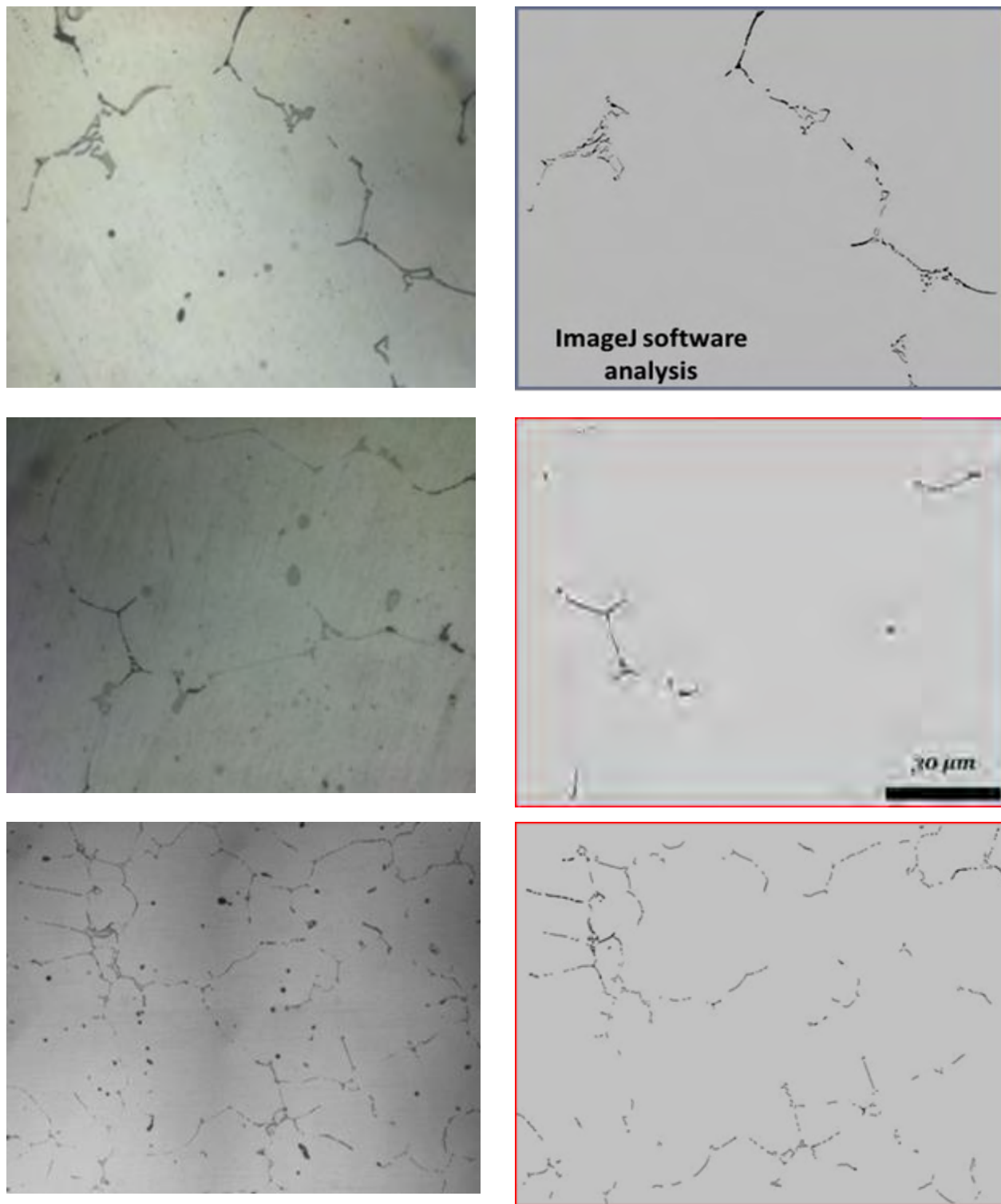


Figure 2.22: Microstructures (left) and corresponding Image-J displays used for the measurement of phase fractions

Table 2.6: Comparison between calculated and measured phase fractions in the as-cast 6082 alloy

|                            | Calculated (x10 <sup>-3</sup> )<br>Scheil simulations |      | Measured (x10 <sup>-3</sup> )<br>Quantitative<br>metallography |
|----------------------------|---|------|--|
| <b>β-AlFeSi</b>            | 2.57  | 6.54 | 6.07   |
| <b>α-AlFeSi</b>            | 3.97  |      |  |
| <b>Mg<sub>2</sub>Si</b>    | 3.81  |      | 3.65   |
| <b>Quaternary eutectic</b> | 3.8   |      | 4.1  |

## 2.6. Effect of Mn on Mg<sub>2</sub>Si and β-AlFeSi phases

The results of the Scheil simulations have shown that increasing the Mn level from a low 0.03% to a high 0.45mass% has two major effects, for the high-strength alloys with more than 0.4mass% Si:

- reduction of β-AlFeSi mole fraction
- reduction of Mg<sub>2</sub>Si mole fraction

These reductions are expressed for β-AlFeSi as

$$\Delta f_{\beta} = \frac{f_{\beta}^{0.2Mn} - f_{\beta}^{0.03Mn}}{f_{\beta}^{0.03Mn}} \quad (21)$$

and for Mg<sub>2</sub>Si as

$$\Delta f_{Mg_2Si} = \frac{f_{Mg_2Si}^{0.2Mn} - f_{Mg_2Si}^{0.03Mn}}{f_{Mg_2Si}^{0.03Mn}} \quad (22)$$

where f, denotes the mole fractions of these phases at the two levels of Mn content 0.03 and 0.2 mass%. These reductions are plotted in Figure 2.23 for the β-AlFeSi phase and Fig.24a, b for the Mg<sub>2</sub>Si phase as a function of Si content (above 0.4mass%) for various levels of Mg ranging from 0.5 to 1.2 mass%. In general the reduction in the β-AlFeSi is up to 15% while the respective reduction in the Mg<sub>2</sub>Si can reach 18%. Regarding the β-AlFeSi phase, with increasing the Si content (for fixed Mg content) the reduction first increases and then decreases. The maximum reduction of β-AlFeSi is located between 0.5-0.6%Si depending on

the Mg level. In this range of Si, the reduction in  $\beta$ -AlFeSi increases with Mg, reaching a maximum 15% for 0.8%Mg and then decreases for higher Mg contents. The maximum reduction in  $\beta$ -AlFeSi is 15% for 0.5Si-0.8Mg (0.2Mn).

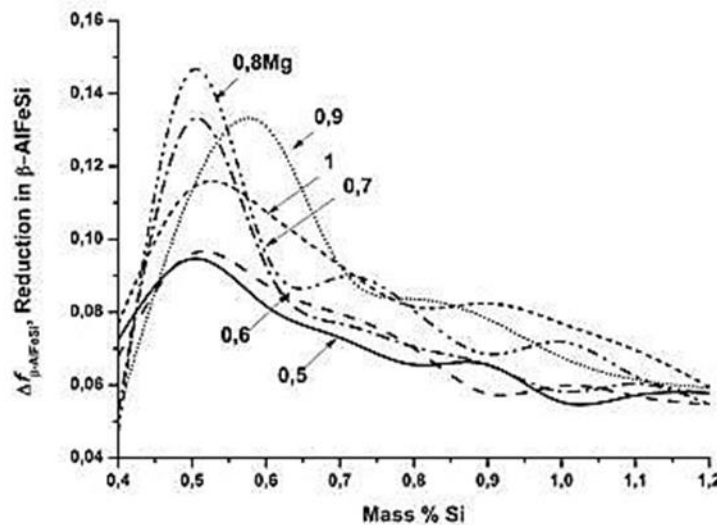
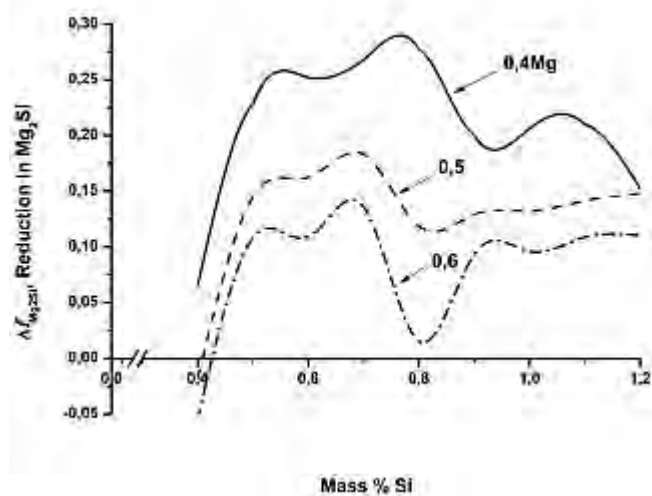
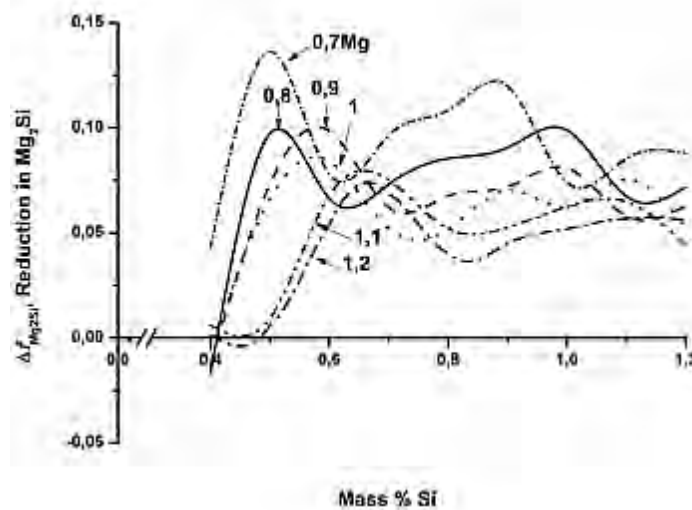


Figure 2.23: Mn-induced reduction of  $\beta$ -AlFeSi phase as a function of Si alloy content for various levels of Mg in the alloy

Regarding the reduction in the  $Mg_2Si$  phase, two behaviours are seen. The first is shown in Figure 2.24a for the 0.4-0.6 Mg level (mass%) where the reductions in  $Mg_2Si$  are higher and can reach values up to 27% depending on the Si level. In this range the lowest reduction in  $Mg_2Si$  (2%) appears for the 0.8Si-0.6Mg composition. The second is shown in Figure 2.24b for the higher level of Mg between 0.7 and 1.2 mass% where the reductions in  $Mg_2Si$  are lower and limited to values up to 13%. Here the minimum reduction (0%) in  $Mg_2Si$  appears for the 0.5Si-1.2Mg composition. It is clear that the Mg-Si compositions for the highest reduction in  $\beta$ -AlFeSi do not coincide with those for lowest reduction in  $Mg_2Si$ .



(a)



(b)

Figure 2.24: Mn-induced reduction in  $\text{Mg}_2\text{Si}$  phase as a function of Si alloy content for (a) 0.4-0.6 and (b) 0.8-1.2 Mg (mass %) in the alloy

## 2.7. Mapping of intermetallic phases

Alloys 6060 and 6063 contain 0.03 mass% Mn while alloy 6082 contains 0.45 mass% Mn. Therefore, Scheil calculations for phase fraction mapping were conducted for these two Mn levels. The mole fraction of  $\beta\text{-AlFeSi}$  and  $\text{Mg}_2\text{Si}$ , is depicted in the contour plots of fixed mole fractions in Figures 2.25 (a) and (b) respectively as a function of Mg and Si content for the two Mn levels of 0.03 and 0.45 mass %. The mole fraction of the  $\beta\text{-AlFeSi}$  phase decreases towards the lower right corner of the contour plot, indicating that low  $\beta\text{-AlFeSi}$  can be obtained at lower Si and higher Mg contents. The 0.45 % Mn iso- $\beta$  lines lie above the respective 0.03 % Mn iso- $\beta$  lines, indicating that for fixed Mg content, higher Mn allows the use of higher Si, without further increase of  $\beta\text{-AlFeSi}$  (Si stabilizes  $\beta\text{-AlFeSi}$ ). The spacing between the iso- $\beta$  lines for the two Mn levels increases towards the upper left corner of the contour plot, indicating that the effect of Mn (in reducing  $\beta\text{-AlFeSi}$ ) becomes stronger at higher Si and lower Mg contents.

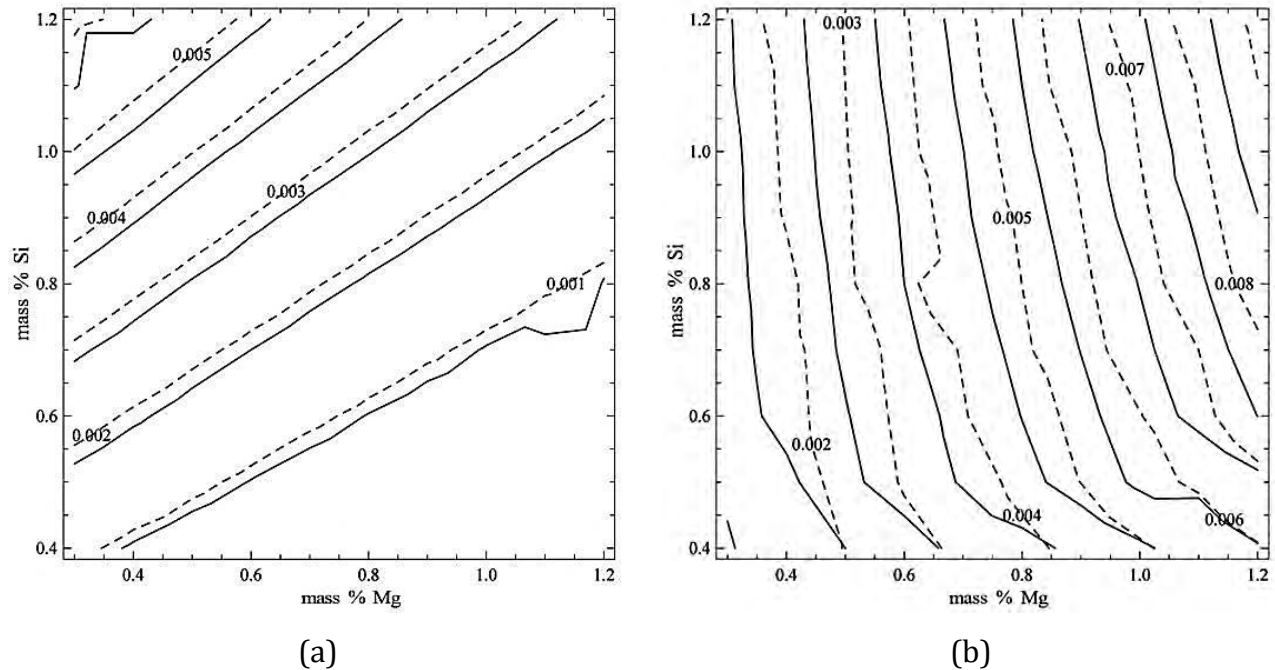


Figure 2.25: Contour plots (maps) of fixed mole fractions of (a)  $\beta$ -AlFeSi and (b)  $\text{Mg}_2\text{Si}$  phases in the as-cast microstructure of Al-Mg-0.2Fe-Mn alloys (full lines 0.03 Mn, dotted lines 0.45 Mn, mass%)

Regarding the  $\text{Mg}_2\text{Si}$  phase (Figure 2.25b) it is clear that the mole fraction increases towards the upper right corner of the contour plot, indicating that an increase of both Mg and Si results in an increase of  $\text{Mg}_2\text{Si}$ , with Mg having a stronger effect. The 0.45 % Mn iso- $\text{Mg}_2\text{Si}$  lines lie above the 0.03 % Mn lines, indicating that a higher Mg content is required to obtain the same  $\text{Mg}_2\text{Si}$  mole fraction in the microstructure.

Mapping of both the  $\text{Mg}_2\text{Si}$  phase and the  $\beta$ -AlFeSi phase across the Mg-Si space can be very useful for alloy design purposes. Such maps are shown in Figure 2.26 (a) and (b) for the two Mn levels of 0.03 and 0.45 % Mn respectively. The mole fractions of the  $\beta$ -AlFeSi phase range from 0.001 to 0.005 while those for the  $\text{Mg}_2\text{Si}$  range from 0.002 to 0.009.

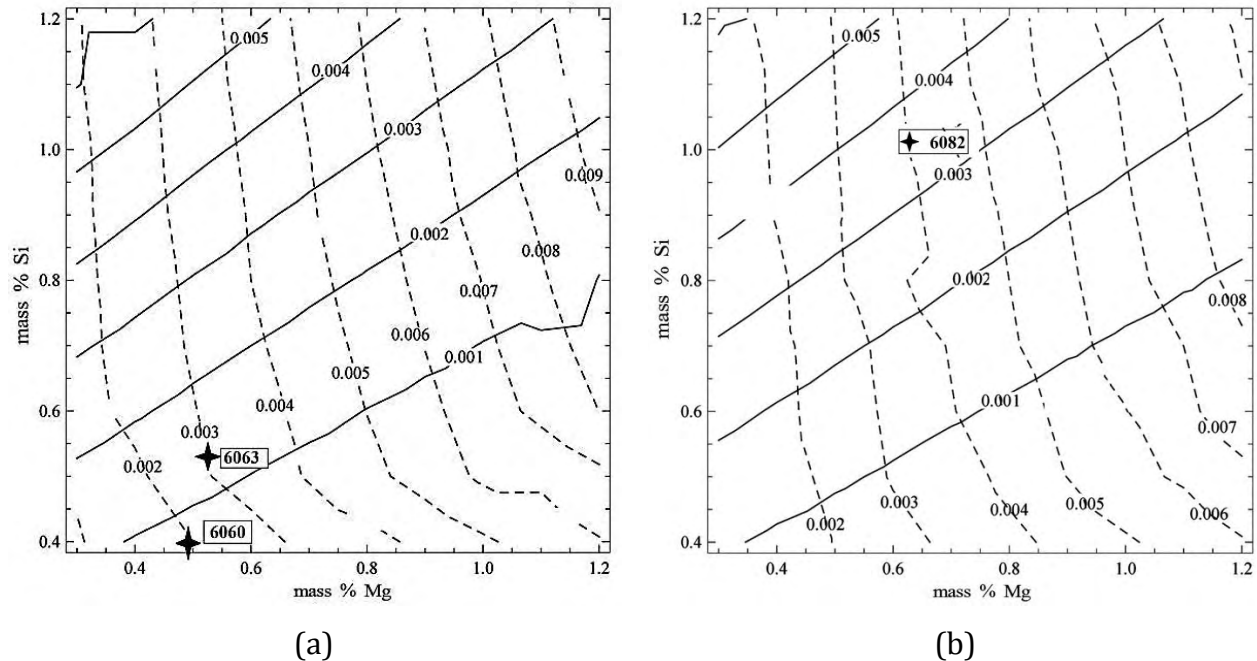


Figure 2.26: Contour plots (maps) of fixed mole fractions  $\beta$ -AlFeSi (solid lines) and  $\text{Mg}_2\text{Si}$  (dotted lines) in as-cast microstructure of Al-Mg-Si-0.2Fe-Mn alloys for (a) 0.03 Mn and (b) 0.45 Mn, mass%. Compositions for alloys 6060, 6063 and 6082 are indicated on the maps.

The position of alloys 6060, 6063 and 6082 is also indicated on the maps. All three alloys possess a low fraction of  $\beta$ -AlFeSi indicating an excellent extrudability potential. In addition, the 6082 alloy possesses a higher fraction of  $\text{Mg}_2\text{Si}$  indicating a higher strength potential compared to 6060 and 6063. The  $\text{Mg}_2\text{Si}$  is maximized towards the upper right corner while the  $\beta$ -AlFeSi phase is minimized towards the lower right corner of the maps. This allows selection of optimum compositions for favourable as-cast microstructures in terms of the two phases. The Mn effect can be summarized as the potential to move to higher Mg and Si compositions in order to obtain higher amount of  $\text{Mg}_2\text{Si}$  without at the same time increasing the  $\beta$ -AlFeSi phase in the as-cast microstructure.

## 2.8. Conclusions

From the results presented in this chapter the following conclusions can be drawn: Computational alloy thermodynamics, based on the CALPHAD approach, has been applied for the calculation of equilibrium phase constitution as a function of alloy composition and temperature. Isopleth phase diagrams in multicomponent alloys have been calculated permitting the determination of the stability limits of the various phases in the system.

This approach was also applied to carry out Scheil-Gulliver solidification simulations and calculate the resulting microsegregation of elements and phases in the as-cast microstructure.

Segregation profiles for elements and phases across the grain were determined as a function of alloy composition.

Standard metallographic techniques including optical microscopy and scanning electron microscopy (SEM) were applied to reveal the microstructure of the as-cast and homogenized materials. Phase fractions were measured by applying quantitative image analysis. The results of the simulations were confirmed experimentally.

The variation of the mole fractions of the extrudability-limiting  $\beta$ -AlFeSi phase and the strengthening  $\text{Mg}_2\text{Si}$  phase with alloying elements can be mapped over the useful range (0-1.2 mass%) in the Mg-Si composition space.

The constructed maps indicate that low mole fractions of  $\beta$ -AlFeSi are associated with lower Si and higher Mg compositions. On the other hand, high mole fractions of  $\text{Mg}_2\text{Si}$  are associated with both higher Si and Mg compositions, with Mg possessing a stronger effect. Construction of maps for different levels of Mn has shown that addition of Mn could allow for higher alloying with Mg and Si, in order to obtain higher amount of  $\text{Mg}_2\text{Si}$ , without at the same time increasing the  $\beta$ -AlFeSi intermetallic phase in the as-cast microstructure



## 2.9. References

- [1] G. Mrowka-Nowotnik, J. Sieniawski, M. Wierzbinska, Arch. Mater. Sci. Eng. 28(2007) 69-76.
- [2] Y.L. Liu, S.B. Kang, J. Mater. Sci. 32 (1997) 1443-1447.
- [3] P. Mukhopadhyay Inter. Sch. Res. Net. ISRN Metallurgy (2012)
- [6] W.D. Fei, S.B. Kang, J. Mater. Sci. Lett. 14 (1995) 1795-1797
- [7] H. Tanihata, T. Sugawara, K. Matsuda, S. Ikeno, J. Mater. Sci. 34 (1999) 1205-1210.
- [8] A. Verma, S. Kumar, P.S. Grant, K.A.Q. O'Reilly, J. Alloys Compd. 55 (2013) 274-282.
- [9] A. Wimmer, J. Lee, P. Schumacher, Berg-und Hutten. Monatshefte 157 (2012) 301-305.
- [10] Y.L. Liu, S.B. Kang, J. Mater. Sci. 32 (1997) 1443-1447
- [11] Y. Du, Y.A. Chang, S.D. Liu, B.Y. Huang, F.Y. Xie, Y. Yang, S.L. Chen, Z. Metallkunde 96 (2005) 1351-1362
- [12] J.O. Andersson, T. Helander, L. Höglund, P. Shi, B. Sundman, Calphad 26 (2002) 273-312.
- [13] H.L. Lukas, S.G. Fries, B. Sundman, Computational thermodynamics, the Calphad method, Cambridge university press, 2007
- [14] J. Ansara, A.T. Dinsdale, M.H. Rand: COST 507: Thermochemical database for light metal alloys, European Community publication, 2, EUR 18449 (1991).
- [15] G. Inden, Physica 103B (1981) 82-100
- [16] B. Sundman, Agren, J., Journal of Physics and Chemistry of Solids 42 (1981) 297-301.
- [17] J. Lacaze, L. Eleno, B. Sundman, Metall. Mater. Trans. A 41A (2010) 2208-2215.
- [18] E. Scheil, E. Metallkde, 34 (1942) 70.
- [19] C.H. Gulliver, J. Inst. Metals, 9 (1913) 120.
- [20] R. W. Balluffi, S. M. Allen, W. G. Carter, "Kinetics of Materials" Wiley- Interscience (2005)
- [21] N. Belov , D. Eskin, A. Aksenov Elsevier (2005) 17-33
- [22] M. Wu, A. Ludwig, Metall. Mater. Trans. A 38A (2007) 1465-1475.
- [23] M. Wu, J. Li, A. Ludwig, A. Kharicha, Comput. Mater. Sci. 79 (2013) 830-840
- [24] ASTM Specification, E-522 (1998)
- [25] Haidemenopoulos, G.N., Kamoutsi, H., Zervaki, A.D., Jour. Mat. Proc. Tech. 212 (2012), 2255-2260
- [26] Rayleigh, J.W, Ph. Mag. 34, (1892) 481-502
- [27] Zhang, W., Du, Y., Peng, Y., Wen, G., Wang, S., In. Jour. R. Met. H. Mat. 104, (2013) 721-735
- [28] Mondolfo L.F., 1976. Aluminum Alloys: Structure and properties. Butterworths, London-Boston
- [29] Warmuzek, M., Rabczak, K., Sieniawski, J., Jour. Mat. Proc. Tech. 175, (2005) 421-426.
- [30] Liu, Y.L., Kang, S.B., Kim, H.W., Mat. Let. 41 (1999), 267-272.
- [31] Mrowka-Nowotnik, G., Sieniawski, J., Wierzbinska, M., Arch. Mat. Sc.Eng. 28 (2007), 69-76.



## 3. Simulation of Homogenization

### 3.1. Introduction

Homogenization is a significant link of the process chain of the extrudable 6xxx Al-alloys. It follows casting and takes place before extrusion. The main purpose of homogenization is, therefore, to remove the detrimental effects of microsegregation left over by the casting process and to “condition” the material for the extrusion process. In that respect, homogenization can be considered as a “key process”, since it controls in a large degree the extrudability of the alloy. The homogenization has received considerable attention, mostly in experimental terms, both in laboratory and industrial scale. There is a large amount of published work, briefly reviewed in the next section, on the effects of the homogenization parameters on the degree of homogenization. However, despite its importance, the work on simulation of the homogenization process is limited. This is due to the complexity of the process, since there is a series of phase transformations, which take place concurrently, in a multiphase and multicomponent system, such as the Al-Mg-Si-Fe-Mn system under consideration. The most important phenomena, which take place during homogenization of the as-cast billets, are the following:

1. Removal of the microsegregation of the alloying elements
2. Removal of non-equilibrium low melting point eutectics, particles and segregation gradients which provide areas with low melting point in order to avoid cracking or tearing during subsequent hot working
3. Shape control (spheroidization) of remaining intermetallics and dispersoids with sharp edges such as Fe-based intermetallics, which give poor workability
4. Formation of secondary particles (dispersoids) for grain size control during extrusion or rolling.
5. The dissolution of the  $\text{Mg}_2\text{Si}$  phase and the reprecipitation during cooling
6. The  $\beta \rightarrow \alpha\text{-AlFeSi}$  transformation.

The homogenization process parameters are the homogenization temperature, homogenization time and the cooling rate from the homogenization temperature. The correct selection of the homogenization temperature ensures that all necessary

transformations are activated and take place in an appreciable rate. The homogenization time should also be selected carefully in order to ensure that the “conditioning” of the billet for extrusion is accomplished. A longer, than necessary, homogenization time usually results in increased costs and loss of productivity in the cast house. The cooling rate after homogenization is also very important, since it controls the precipitation reactions in the billet before extrusion. The cooling after homogenization is treated in Chapter 5. From the above discussion, it is clear that the control of the homogenization parameters is an important issue in the production of extrudable 6xxx Al-alloys.

The aim of the present chapter is to introduce a robust computational methodology for treating the homogenization problem. This methodology constitutes a significant step towards the design of the homogenization process. This is particularly important in the development process of new alloys, since the design of homogenization can lead to significant savings in cost and time for the alloy development.

### **3.2. Literature review**

Current literature is reviewed in this section regarding the effect of homogenization parameters on the removal of microsegregation and on the phase transformations taking place during the homogenization process. As stated above, most of the work up to date is experimental, either on a laboratory or on an industrial scale.

Homogenization comprises of three major steps, heating the as-cast billet with a particular rate, holding at a constant temperature for a certain time, and cooling with a proper cooling rate. The introduction of continuous homogenization lines has significantly improved the temperature uniformity of homogenization allowing the holding times to be minimized. Batch homogenization, however, provides flexibility in practices tailored for different aluminum alloys. Soft 6060 and 6063 alloys are best homogenized at a higher soak temperature than harder alloys such as 6061 and 6082 [1]. After direct chill (DC) casting, the solid solution is supersaturated and the supersaturation increases from the center to the edges of the dendritic branches because of microsegregation.

Major reactions during homogenization involve the dissolution of  $\text{Mg}_2\text{Si}$ , coarsening of dispersoids, spheroidization of undissolved particles and the transformation  $\beta\text{-AlFeSi} \rightarrow \alpha\text{-AlFeSi}$ , which is important due to the low high-temperature ductility of the  $\beta$ -phase [2].

The homogenization practice has been investigated experimentally where both industrial and academic researchers have focused on the influence of temperature and time of the procedure on the microstructure and mechanical properties of the homogenized billets [3-6]. Long-time homogenization treatments at 545 °C for 20 h, indicated that  $\text{Mg}_2\text{Si}$  and Si intermetallic compounds are dissolved into the matrix completely, and the remaining phases were  $\alpha(\text{Al})$  matrix and  $\text{Al}_{15}(\text{FeMn})_3\text{Si}_2$  or  $\alpha\text{-AlFeSi}$  [7].

The controlling factor in the homogenization of an alloy is the diffusivity of the respective alloying elements at the homogenization temperature. The higher the homogenization temperature, the faster the elemental homogeneity can be obtained and, thus, the more efficient this practice becomes in terms of industrial throughput. However there exists an upper limit in the homogenization temperature. It has been found that homogenization of 6082 alloy at temperature close to 540°C leads to partial local melting of dendrite cell boundaries while at even higher temperatures full surface melting and alloy degradation occurs [8]. The homogenization temperature, therefore, should not exceed the solidus temperature in the particular alloy since this could result in localized melting. This melting could cause structural damage of a type that cannot be repaired after homogenization. This damage has been reported as excessive void formation, segregation, blistering and cracking [9]. The exact solidus temperature of the material cannot be predicted from the phase diagram because the microstructure is far from equilibrium. As a result of microsegregation, regions exhibiting high concentration of alloying elements melt at temperatures below the equilibrium solidus temperature. This is especially true for the low-melting eutectics. The eutectic melting temperatures are presented in Table 1 for several reactions.

The  $\beta\text{-AlFeSi}$  to  $\alpha\text{-AlFeSi}$  transformation is probably the most important reaction during the homogenization process. The  $\alpha\text{-AlFeSi}$  has a cubic crystal structure and globular morphology while the  $\beta\text{-AlFeSi}$  possesses a monoclinic structure and a plate-like morphology, limiting the extrudability of the as-cast billet by inducing local cracking and surface defects in the extruded material. The  $\beta$  to  $\alpha\text{-AlFeSi}$  phase transformation

considerably improves the extrudability of the aluminum since the transformed  $\alpha$ -particles in the homogenized material improve the ductility and the surface quality of the extruded material [10, 11].

Additional microstructural changes, such as the dissolution of  $\text{Mg}_2\text{Si}$  or Si particles, also occur during homogenization. However, since the  $\text{Mg}_2\text{Si}$  or Si particles dissolve rather fast, it is the  $\beta$ -to- $\alpha$  transformation kinetics, which determines the minimum homogenization time that is needed to get the material in a suitable state for extrusion.

Table 3.1: Eutectic melting temperatures in Al-Mg-Si alloys [10]

| Melting Temperature      | Reaction  |
|--------------------------|---|
| $\sim 575^\circ\text{C}$ | $\text{Al} + \beta - \text{AlFeSi} + \text{Si} \rightarrow \text{Liquid}$                                     |
| $\sim 576^\circ\text{C}$ | $\text{Al} + \beta - \text{AlFeSi} + \text{Mg}_2\text{Si} \rightarrow \text{Liquid} + \alpha - \text{AlFeSi}$ |
| $\sim 577^\circ\text{C}$ | $\text{Al} + \text{Si} \rightarrow \text{Liquid}$   |
| $\sim 587^\circ\text{C}$ | $\text{Al} + \text{Mg}_2\text{Si} \rightarrow \text{Liquid}$  |
| $\sim 612^\circ\text{C}$ | $\text{Al} + \beta - \text{AlFeSi} \rightarrow \text{Liquid} + \alpha_h - \text{Al(FeMn)Si}$                  |
| $\sim 630^\circ\text{C}$ | $\text{Al} + \alpha - \text{AlFeSi} \rightarrow \text{Liquid} + \text{Al}_3\text{Fe}$                         |

Another transformation that takes place during holding at the homogenization temperature is the spheroidization of the non-dissolvable  $\alpha$ -AlFeSi phase. This issue will be discussed in Chapter 4.

Cooling of the billet after homogenization is very important in order to obtain the suitable microstructure to improve extrudability as well as the final mechanical properties of the extrusion. A fully solutionized billet, as obtained at the end of homogenization holding, is difficult to extrude due to solid solution strengthening. The motivation behind controlled cooling is the establishment of a specific precipitation state [13]. During cooling to room temperature precipitation of  $\text{Mg}_2\text{Si}$  and other Fe, Mn and Cr-containing phases takes place. The size and the density of these particles are crucial because they enhance the recrystallization resistance of the material [13], which is beneficial for the final mechanical properties. Respectively, the size and the density of  $\text{Mg}_2\text{Si}$  particles must be such that they can be dissolved easily before extrusion, leading to improved extrudability [14]. It has been shown that smaller  $\text{Mg}_2\text{Si}$  particles, obtained after cooling, dissolve faster during extrusion [13-15]. The amount of Mg and Si in solid solution, and hence the amount of  $\text{Mg}_2\text{Si}$  precipitated, are highly affected by the cooling rate from the homogenization temperature.

Slow cooling tends to produce coarse  $\text{Mg}_2\text{Si}$  particles while rapid cooling trap the Mg and Si in solution with little or no  $\text{Mg}_2\text{Si}$  precipitation [16,17]. A decrease in the cooling rate increases the  $\text{Mg}_2\text{Si}$  precipitation and decreases the amount of Mg in solid solution. Mn additions up to 0.027% have no effect on  $\text{Mg}_2\text{Si}$  precipitation [17]. However the effect of Mn on the precipitation during cooling has not been investigated extensively. Zajac et al. [14] and Nowotnik et al. [18] investigated the effect of the cooling rate on the final mechanical properties of the 6005, 6082 and 6063 aluminum alloys. Usta et al. [26] and van de Langkruis [15,19] studied the dissolution-coarsening kinetics of the  $\text{Mg}_2\text{Si}$  particles during reheating. Reiso et al. [16] correlated the cooling rate to the maximum extrusion velocity for various chemical compositions of AlMgSi alloys. Birol et al. [20,21] studied the effect of the homogenization temperature and time and the effect of cooling rate and the microstructure of 6063 and 6082 alloys through metallographic techniques.

As mentioned above, most of the published work approaches the homogenization process experimentally. The modelling or simulation work is rather limited. In a previous doctoral thesis [22] at the Laboratory of Materials an attempt to simulate the dissolution of the  $\text{Mg}_2\text{Si}$  was presented. Kuijpers et al. [23] simulated the dependence of the  $\beta\text{-AlFeSi}$  to  $\alpha\text{-Al(FeMn)Si}$  transformation kinetics on the alloying elements and found a significant effect of the Mn concentration as it increases the transformation rate. Haidemenopoulos et al. [24] modeled the transformation of iron intermetallics during homogenization of 6xxx alloys and also reported similar trends. However an integrated model, taking into account the prior microsegregation and, most importantly, taking into account the concurrent  $\text{Mg}_2\text{Si}$  dissolution and  $\beta$  to  $\alpha\text{-AlFeSi}$  transformation, in a multiphase, multicomponent system, exhibiting grain size variations does not exist. It is the aim of this chapter to introduce such a model. The computational methodology is presented in the following section. The experimental validation of the model was performed on alloy 6082.

### 3.3. Methodology

#### 3.3.1. Computational Method

The key elements of the computational approach to simulate the homogenization process are the following:

- The fact that the grain size in the as-cast microstructure is not uniform is incorporated in the model. A Dual-Grain Model (DGM) has been developed to serve as the computational region. The region represents two neighboring grains, in contact, with significantly different grain sizes. In this way the fact that the transformation rate is higher in the smaller grains is taken into account. The DGM region serves as the representative volume element (RVE) for the solution of the homogenization problem.
- The initial conditions in terms of composition and phases present in the DGM correspond to the actual microsegregation of the as-cast microstructure. The composition as well as the phase fractions profiles that were introduced as initial conditions was the Scheil microsegregation profiles, calculated from the relevant Scheil simulations for the specific alloy. The Scheil simulations were presented in Chapter 2.
- Two key phase transformations are treated concurrently in both grains of the DGM. These are the  $\text{Mg}_2\text{Si}$  dissolution and the  $\beta$  to  $\alpha\text{-AlFeSi}$  transformation. Both are diffusional transformations and their rate is controlled by the diffusion of alloying elements. Since the diffusion of Mg and Si is faster than the diffusion of Fe and Mn, it is expected that the dissolution of  $\text{Mg}_2\text{Si}$  is faster than the  $\beta$  to  $\alpha\text{-AlFeSi}$  transformation. In the DGM model, only lattice diffusion through the matrix has been considered. Grain boundary diffusion or dislocation assisted diffusion were not considered, since in the homogenization process the diffusion takes place from the boundaries to the grain interiors in order to eliminate the microsegregation gradients. In addition, the dislocation density of the material has normal values, since the material has not undergone any cold deformation before homogenization.
- The intermetallic phases were treated as non-diffusion phases. This means that they act entirely as sinks or sources of alloying elements. Diffusion is restricted exclusively to the matrix.



- The diffusion problem is one-dimensional and is treated in a multicomponent (Al-Mg-Si-Fe-Mn) and multiphase system. The phases present in the system are the FCC aluminum matrix and the dispersions of  $Mg_2Si$  and the iron intermetallics  $\beta-AlFeSi$  and  $\alpha-AlFeSi$ .

The DGM calculation domain, developed in order to simulate homogenization considering the different grain sizes between neighboring grains is depicted in Figure 3.1.

Following metallographic examination, two sizes of  $90\mu m$  and  $20\mu m$  respectively were selected for the construction of the DGM. The difference between the grain sizes is significant and allows the study of the grain size effect on homogenization.

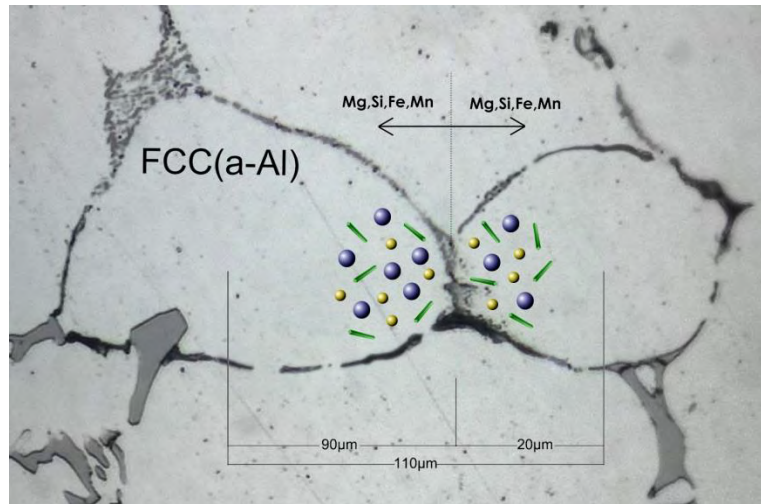


Figure 3.1: The Dual Grain Model considering the different grain sizes between neighboring grains

The total region size is  $110\mu m$  considering the two grains in contact. Due to the symmetry, only half of the grains were considered.

In order to input the concentration profile of alloying elements as well as the phase fractions profiles resulting from the Scheil simulations as initial conditions, the fraction solid axis  $f_s$  was converted to a distance axis via the relation

$$x_s = f_s \frac{d}{2} \quad (1)$$

where  $d$  is the grain size region of the DGM (90 or 20  $\mu\text{m}$ ). Thus the diffusion problem is solved in one direction ( $x$ ). The  $\text{Mg}_2\text{Si}$  phase as well as the intermetallics  $\alpha\text{-AlFeSi}$  and  $\beta\text{-AlFeSi}$  phases are taken as a dispersed phases in the FCC matrix.

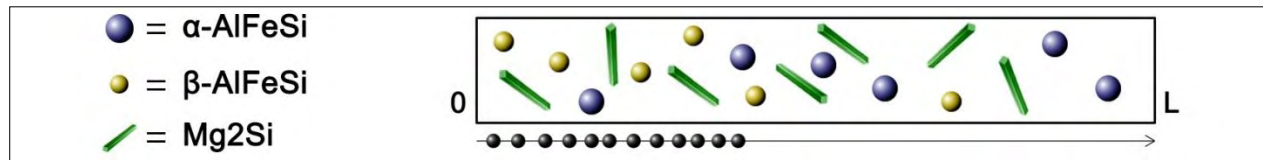


Figure 3.2: Dispersed Phase model in DICTRA

This diffusion problem was solved with the computational kinetics package DICTRA [25]. One basic model assumption is that the growth and dissolution rates of the precipitate phases are very high compared with the diffusion rates in the matrix. Alternatively, the matrix diffusion is the controlling mechanism of the overall kinetics. This assumption is tolerable for the high homogenization temperatures, since the growth-dissolution rates are very high and the particles reach the equilibrium state very fast. Consequently the local conditions are rather concentration dependent than time-dependent. Locally, most of the solute is trapped into the particles, reducing the concentration gradients and the diffusion rate in the matrix. The “Dispersed Phase” module in DICTRA was employed as shown in Figure 3.2. It treats problems involving diffusion through microstructures containing dispersed precipitates of secondary phases. Diffusion is assumed to take place only in the matrix phase. The dispersed phases are considered as “non-diffusion phases”. They act as point sinks or sources of solute atoms in the simulation and their fraction is calculated from the average composition in each node, assuming local equilibrium. The growth or dissolution of phases leads to adjustments in the concentration profiles of the elements to be used in the next time-step of the calculation. What changes during the calculations in each time step is the volume fraction of phases and the local matrix compositions (composition profiles) through the matrix diffusion.

The mathematical formulation of the multicomponent diffusion problem is based on the Onsager principles and is described here briefly. A full description is presented in [26-28].

Following the treatment in [26], the first Onsager principle is

$$T \dot{\sigma} = - \sum_{i=1}^N J_i F_i - \sum_{i=1}^N J_i \frac{\partial \mu_i}{\partial x} \quad (1)$$

stating, that the rate of entropy production (free energy dissipation) is the sum of the products between forces and fluxes. In the diffusion case the “forces” are the chemical potential gradients, which drive diffusion, and “fluxes” are the diffusive fluxes. The second Onsager principle states that the forces are linearly related to the fluxes by the expression

$$J_i = \sum_{k=1}^N L_{ik} F_{kj} \quad (2)$$

In the V-frame, where the volume is fixed, the fluxes of the N components are related with the expression

$$\sum_{i=1}^N \Omega_i J_i = 0 \quad (3)$$

meaning that there are N-1 independent fluxes. The  $\Omega_i$  are the atomic volumes of the elements. This means that the  $N_{th}$  flux is

$$J_N = - \frac{1}{\Omega_N} \sum_{i=1}^{N-1} \Omega_i J_i \quad (4)$$

Using this expression, equation (1) becomes

$$T \dot{\sigma} = - \sum_{i=1}^{N-1} J_i \frac{\partial}{\partial x} \left( \mu_i - \frac{\Omega_i}{\Omega_N} \mu_N \right) \quad (5)$$

and the “forces”  $F_i$  become

$$F_i = - \left( \frac{\partial \mu_i}{\partial x} - \frac{\Omega_i}{\Omega_N} \frac{\partial \mu_N}{\partial x} \right) \quad (6)$$

so that the fluxes of equation (2) become

$$J_i = \sum_{j=1}^{N-1} L_{ij} F_j = - \sum_{j=1}^{N-1} L_{ij} \left( \frac{\partial \mu_j}{\partial x} - \frac{\Omega_j}{\Omega_N} \frac{\partial \mu_N}{\partial x} \right) \quad (7)$$

The fluxes in equation (7) are expressed in relation to the chemical potential gradients. Now the fluxes will be written in the traditional Fick’s 1st law, so that they are related to composition gradients.

The chemical potential of a component i depends on the concentration

$$\mu_i = \mu_i(c_1, c_2, \dots, c_{N-1}) \text{ where } i = 1, 2, \dots, N-1 \quad (8)$$

since there are N-1 independent concentrations. Additionally the Gibbs-Duhem relation imposes an additional constraint that only N-1 chemical potentials can vary independently so that

$$\frac{\partial \mu_i}{\partial x} = \sum_{j=1}^{N-1} \frac{\partial \mu_i}{\partial c_j} \frac{\partial c_j}{\partial x} \quad (9)$$

The fluxes in equation (7) then become

$$J_i = \sum_{j=1}^{N-1} L_{ij} F_j = - \sum_{j=1}^{N-1} L_{ij} \sum_{k=1}^{N-1} \left( \frac{\partial \mu_j}{\partial c_k} - \frac{\Omega_j}{\Omega_N} \frac{\partial \mu_N}{\partial c_k} \right) \frac{\partial c_k}{\partial x} \quad (10)$$

and the interdiffusion coefficient can be identified as

$$D_{ij} = \sum_{k=1}^{N-1} L_{ik} \left( \frac{\partial \mu_k}{\partial c_j} - \frac{\Omega_k}{\Omega_N} \frac{\partial \mu_N}{\partial c_j} \right) \quad (11)$$

The diffusion coefficient can be written as the product of two matrices

$$D_{ij} = \sum_{k=1}^{N-1} L_{ik} Y_{kj} \quad (12)$$

where  $L_{ik}$  are the Onsager coefficients related to the atomic mobilities and  $Y_{kj}$  are the relevant thermodynamic factors which express the dependence of the chemical potential on composition. It is to be noted that in DICTRA, the mobilities are stored in the so-called mobility database, while the thermodynamic factors are calculated via a link to Thermo-Calc. In this way DICTRA takes into account the composition dependence of the diffusion coefficient. The analysis of a N component system requires N-1 independent concentrations and  $(N-1)^2$  independent interdiffusivities. In the Al-Mg-Si-Fe-Mn system considered in this problem, the diffusion matrix contains 16 interdiffusivities.

Coming back to the DGM, the solution of the diffusion equation is performed under the following boundary conditions. Considering a closed system, the boundary conditions are:

$$J_i(0, t) = J_i(L, t) = 0 \quad (13)$$

Or in terms of concentration gradients

$$\frac{\partial c_i}{\partial x} = 0 \text{ at } x=0 \text{ and } x=L \quad (14)$$

The initial conditions for solving the diffusion problem are the results of the Scheil calculations and converted over the diffusion distance for  $t=0$  and can be expressed as follows for the elements:

$$c_i(x, 0) = c_i^s(x) , i=\text{Mg, Si, Fe, Mn} \quad (15)$$

and for the initial fraction of the phases

$$f_k(x, 0) = f_k^{\text{Scheil}} , k=\text{Mg}_2\text{Si, } \alpha\text{-AlFeSi, } \beta\text{-AlFeSi} \quad (17)$$

where  $c_i^s(x)$  and  $f_k^{\text{Scheil}}$  are the compositions and phase fractions respectively resulting from the Scheil simulation presented in Chapter 2.

In DICTRA the mobility parameter,  $M_i$  for an element  $i$  in a given phase can be described by a frequency factor  $M_i^o$  and activation energy  $\Delta G_i^*$  and these are related in equation:

$$M_i = \frac{M_i^o}{RT} \exp\left(-\frac{\Delta G_i^*}{RT}\right) \quad (12)$$

where  $R$  is the gas constant and  $T$  is the absolute temperature. Both  $M_i$  and  $\Delta G_i^*$  are composition dependent. In the spirit of the CALPHAD approach, in a multicomponent system these parameters are expressed with a Redlich-Kister–Muggianu polynomial. It is therefore important to state that the composition dependence of the diffusion coefficients comes not only through the thermodynamic factor but from the mobilities as well.

The thermal cycle obtained for this study consisted of four stages: heating, holding at the homogenization temperature for several hours, cooling to room temperature and pre-heating (before extrusion). Figure 3.3 depicts the temperature – time profile of the homogenization process mentioned above, which includes typical homogenization times and temperatures.

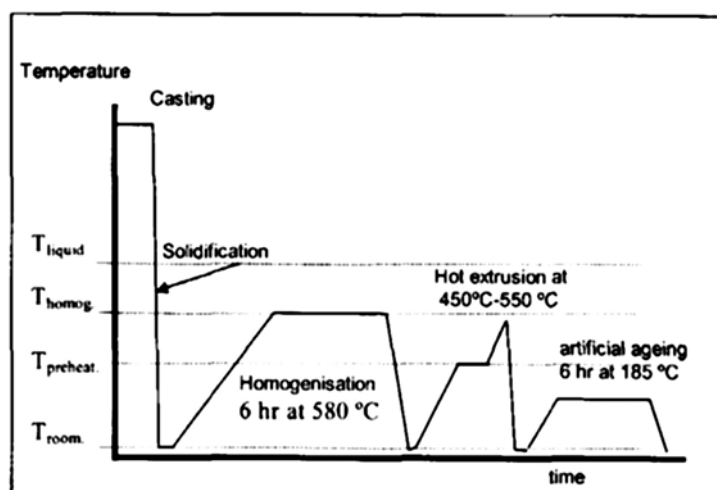


Figure 3.3: The temperature – time profile of the homogenization process

Regarding the time step used in the simulations, the maximum time step allowed, or the highest time step actually taken in the calculation, would affect the final result of the simulation. This effect will be most evident if one or more of the diffusing species have low solubility in the matrix phase. When this is the case, a supersaturation is created in the matrix phase during a diffusion step and if too large a time step is allowed, then too much supersaturation is created. For this reason a time step sensitivity analysis has been performed to assure that there is no time step dependence of the solution.

### 3.3.2. Experimental procedures

In order to validate the results of the computations of the Dual Grain Model, laboratory homogenization treatments were performed in selected alloys listed in Table 2.1 in order to study the progress of homogenization. The homogenization treatments were performed in the temperature range of 540°C-580°C for 30min, 4hr, 6hr and 32 hr. In order to alter the cooling rate, three cooling methods were used: water Quenching (Q), Air cooling (AC) and Forced air cooling (FC). The effect of the cooling rate is discussed in Chapter 5.

After the homogenization heat treatment, the specimens were prepared for standard metallographic examination in order to reveal the microstructure and apply quantitative image analysis. The evolution of the elemental profiles (removal of microsegregation) was performed by SEM-EDX measurements. Phase characterization using EDS elemental

mapping has also been performed in the alloys. The evolution of phase transformation with homogenization time was performed with XRD analysis. Details of the experimental methods are described below.

- **Optical Metallography:** Full metallographic analysis was performed on transverse cross sections (perpendicular to the billet axis) along their diameter according to the marking shown in Figure. 2.3 Specimen preparation included cutting with Struers “Accutom 2”, mounting in resin, The samples were ground on 500 grit SiC water – cooled paper, polish with 3 $\mu$ m and 1 $\mu$ m Diamond paste and finally polished with 0.05 $\mu$ m Colloidal Silica. The microstructure was revealed after etching with the appropriate etchants for each alloy listed in Table 2.2. Examination of the metallographic specimens was carried out on an Optical Metallographic Microscope, Leitz “Aristomet” at magnifications 100 x –1000 x.
- **Scanning Electron Microscopy/EDX analysis:** Further metallographic investigation was carried out on a JEOL SEM at several magnifications. Elemental area mapping and line profiling were also performed for the major alloying elements.
- **X-Ray Diffraction:** X-Ray Diffraction analysis was carried out in order compare the evolution of intermetallic phases after homogenization. The analysis was performed by utilizing a Siemens D-5000 diffractometer operating with a Cu-K $\alpha$  radiation. The time for measurement was 0.008°/sec and t=4020sec.

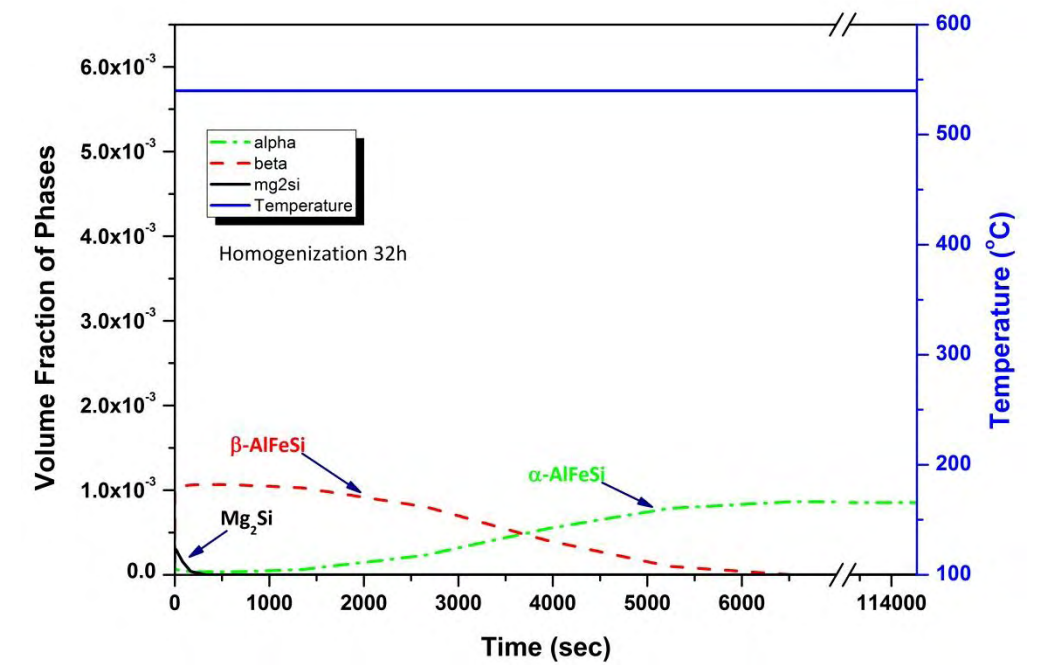
## 3.4. Results and Discussion

### 3.4.1. Dual Grain Model

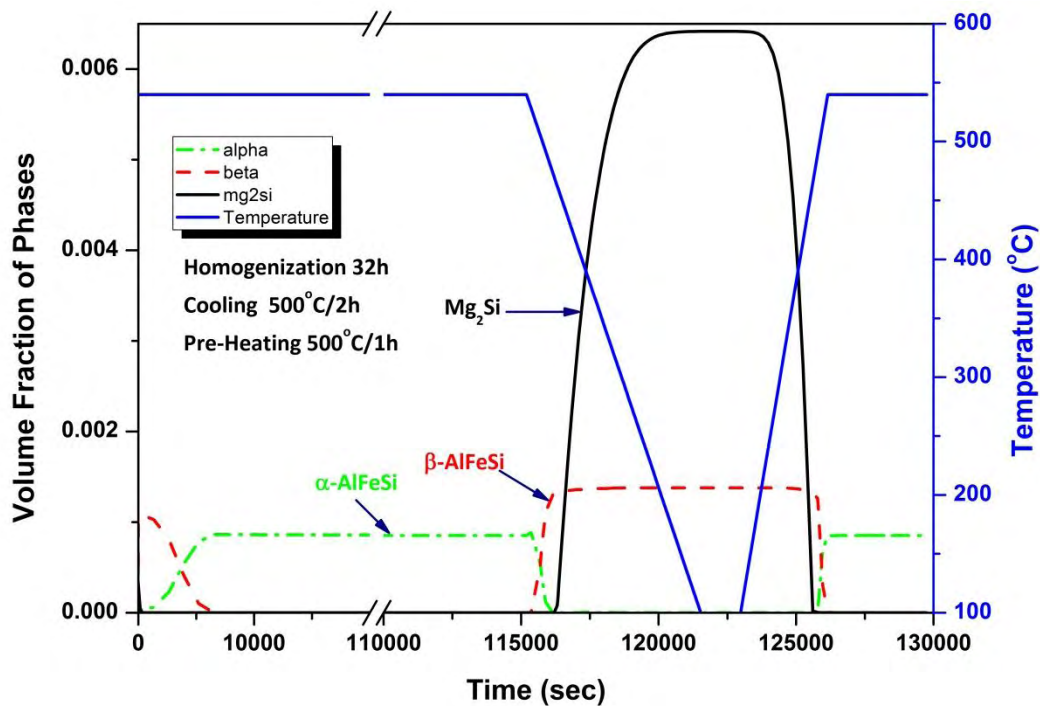
The results of the homogenization Dual Grain Model (DGM) are presented in this section for the 6082 alloy. The evolution of the volume fraction of phases with time is depicted in Figure 3.4a. Figure 3.4a depicts the isothermal holding at 540° C up to 32h (115200 sec). The  $Mg_2Si$  dissolves quickly at the early stages of homogenization (below 500 sec). After an induction period of about 700 sec, the transformation  $\beta-AlFeSi \rightarrow \alpha-AlFeSi$  starts. This is indicated by the reduction of the volume fraction of the  $\beta-AlFeSi$  phase and the corresponding increase of the  $\alpha-AlFeSi$  phase. The  $\beta-AlFeSi$  phase dissolves at a time about 6000 sec (100 min), where the  $\alpha-AlFeSi$  obtains its highest volume fraction and then the volume fraction remains constant in the remaining holding time. In addition to the holding period of 32 h, Figure 3.4b describes the cooling process with a cooling time of 2h and the preheating prior to extrusion to 500°C which is obtained in 1h.  $Mg_2Si$  re-precipitation takes place during cooling from the homogenization temperature and the volume fraction of  $Mg_2Si$  is now much higher than the  $Mg_2Si$  present in the as-cast microstructure (at  $t=0$ ). The respective values are 0.65% and 0.1% respectively. This is attributed to the additional amount of Si coming from the dissolution of the Si-diamond phase and the  $\beta-AlFeSi \rightarrow \alpha-AlFeSi$  transformation during homogenization, since the  $\alpha-AlFeSi$  phase is leaner in Si. Thus there is more Mg and Si available in the matrix to form  $Mg_2Si$  during cooling from the homogenization temperature. This  $Mg_2Si$  dissolves again during pre-heating prior to extrusion. Another interesting effect is depicted in Figure 3.4b.

The reverse transformation  $\alpha-AlFeSi \rightarrow \beta-AlFeSi$  seems to take place during cooling and the direct transformation  $\beta-AlFeSi \rightarrow \alpha-AlFeSi$  takes place during billet preheating. This is in line with phase stabilities since  $\beta-AlFeSi$  is stable at low temperatures. However in the cooling rates encountered in industrial practice, the reverse transformation  $\alpha-AlFeSi \rightarrow \beta-AlFeSi$  does not take place. Therefore after cooling from the homogenization temperature, the iron intermetallic present in the microstructure is the  $\alpha-AlFeSi$  phase, provided that the direct transformation  $\beta-AlFeSi \rightarrow \alpha-AlFeSi$  during homogenization has been completed. The spatial evolution of the  $Mg_2Si$  dissolution and the  $\beta-AlFeSi \rightarrow \alpha-AlFeSi$  transformation are presented below.





(a)



(b)

Figure 3.4 Temporal evolution of phase transformations during the homogenization process a) Isothermal holding at 540°C for 32 h and b) holding at 540°C for 32h cooling down (500°C/2h), preheating 500°C/1h.

### 3.4.2. $\text{Mg}_2\text{Si}$ dissolution

While the temporal evolution of the integrated volume fractions was depicted in Fig.3.4, with the DGM model is possible to monitor the spatial evolution of phase fractions at specific times during homogenization. The dissolution of the  $\text{Mg}_2\text{Si}$  phase from the grain boundaries and its re-precipitation in the grain interiors during cooling from the homogenization temperature has been investigated in this way. The reduction of the mole fraction of  $\text{Mg}_2\text{Si}$  during homogenization at  $540^\circ\text{C}$  is shown in Figure.3.5. The  $t=0$  curve is the  $\text{Mg}_2\text{Si}$  profile at the beginning of homogenization (as-cast condition, Scheil profile). As seen in Figure.3.5, the  $\text{Mg}_2\text{Si}$  phase dissolves rapidly and the complete dissolution of  $\text{Mg}_2\text{Si}$  takes only about 6 min at  $580^\circ\text{C}$  for 6082 alloy.

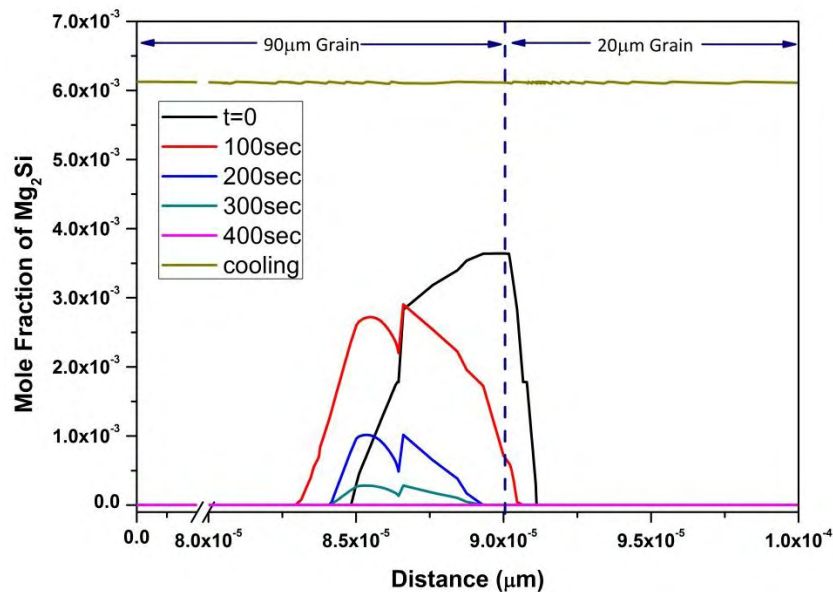


Figure 3.5: The spatial evolution of the  $\text{Mg}_2\text{Si}$  phase from the grain boundaries and its re-precipitation in the grain interiors

The dissolution of the  $\text{Mg}_2\text{Si}$  is faster in the small grain ( $20\mu\text{m}$ ) due to the shorter diffusion distances. In addition the  $\text{Mg}_2\text{Si}$  profile spreads away from the boundary in the large grain. This is due to Mg and Si diffusion towards the grain interior causing precipitation of  $\text{Mg}_2\text{Si}$  in new locations. Then this  $\text{Mg}_2\text{Si}$  also dissolves and in this way the Mg and Si diffuse to the grain interior. Following the complete dissolution of  $\text{Mg}_2\text{Si}$  during isothermal holding at  $580^\circ\text{C}$ , the  $\text{Mg}_2\text{Si}$  phase is re-precipitated during cooling from the

homogenization temperature in the grain interior as shown with the straight line in Figure 3.5. The  $\text{Mg}_2\text{Si}$  fraction after cooling is uniform across both grains.

### 3.4.3. $\beta\text{-AlFeSi} \rightarrow \alpha\text{-AlFeSi}$ transformation

The spatial evolution of the  $\beta\text{-AlFeSi} \rightarrow \alpha\text{-AlFeSi}$  transformation is presented in this section. First in Figure 3.6a the initial profiles of  $\beta\text{-AlFeSi}$  and  $\alpha\text{-AlFeSi}$  in the as-cast structure are depicted. This is to compare with the final profiles after the completion of the transformation in Figure 3.6b, where only the  $\alpha\text{-AlFeSi}$  phase remains with a higher fraction, due to the amount gained by the transformation.

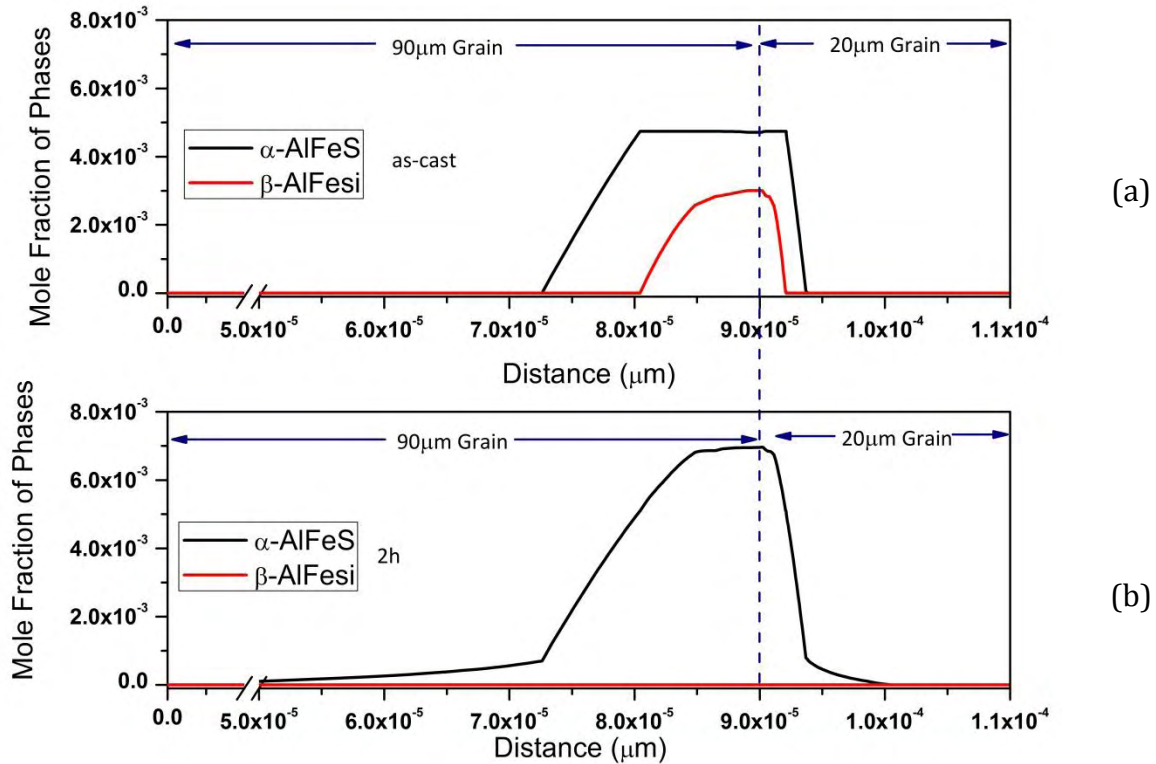
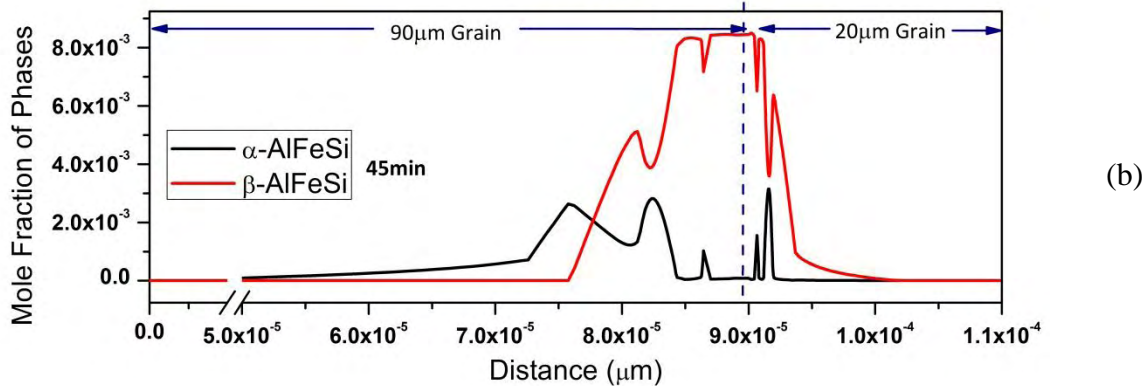
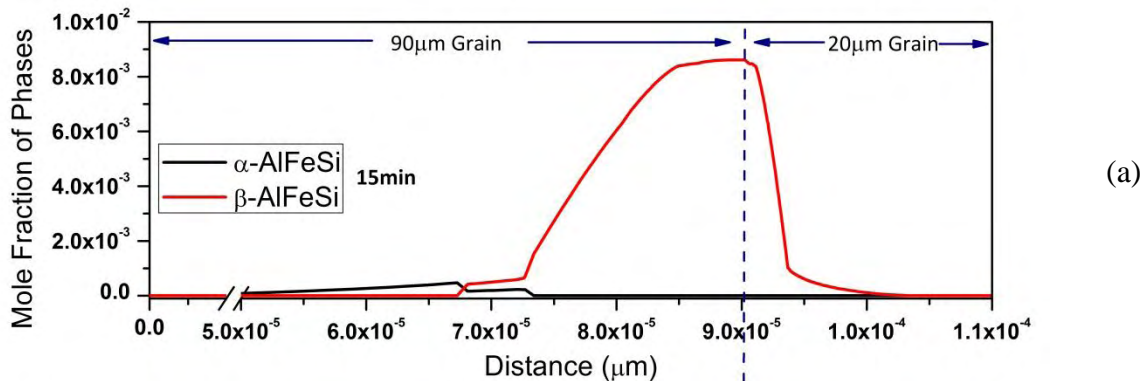


Figure 3.6: The spatial evolution of the  $\beta\text{-AlFeSi} \rightarrow \alpha\text{-AlFeSi}$  transformation a) the initial profiles of  $\beta\text{-AlFeSi}$  and  $\alpha\text{-AlFeSi}$  in the as-cast structure, b) the final profiles after the completion of the transformation

The intermediate stages of the transformation are depicted in Fig. 3.7 (a-d) for times 15, 45min, 1h and 1  $\frac{1}{2}$  hours. The following observations can be made:

- The profiles of  $\alpha$ -AlFeSi and  $\beta$ -AlFeSi exhibit an exact spatial correspondence. Where there is a drop in the fraction of  $\beta$ -AlFeSi, there is a rise in the fraction of  $\alpha$ -AlFeSi at the same location.
- The  $\beta$ -AlFeSi  $\rightarrow$   $\alpha$ -AlFeSi starts at a certain distance from the boundary and the transformation front moves towards the boundary. As a result the profile of  $\alpha$ -AlFeSi spreads towards the grain interior
- The phase fraction profiles are steeper and the transformation is faster in the smaller grain.

The above results indicate that the  $\beta$ -AlFeSi  $\rightarrow$   $\alpha$ -AlFeSi transformation is a transformation which takes place at a region adjacent to the grain boundary by diffusion through the matrix. The transformation takes place at a faster rate in the smaller grain.



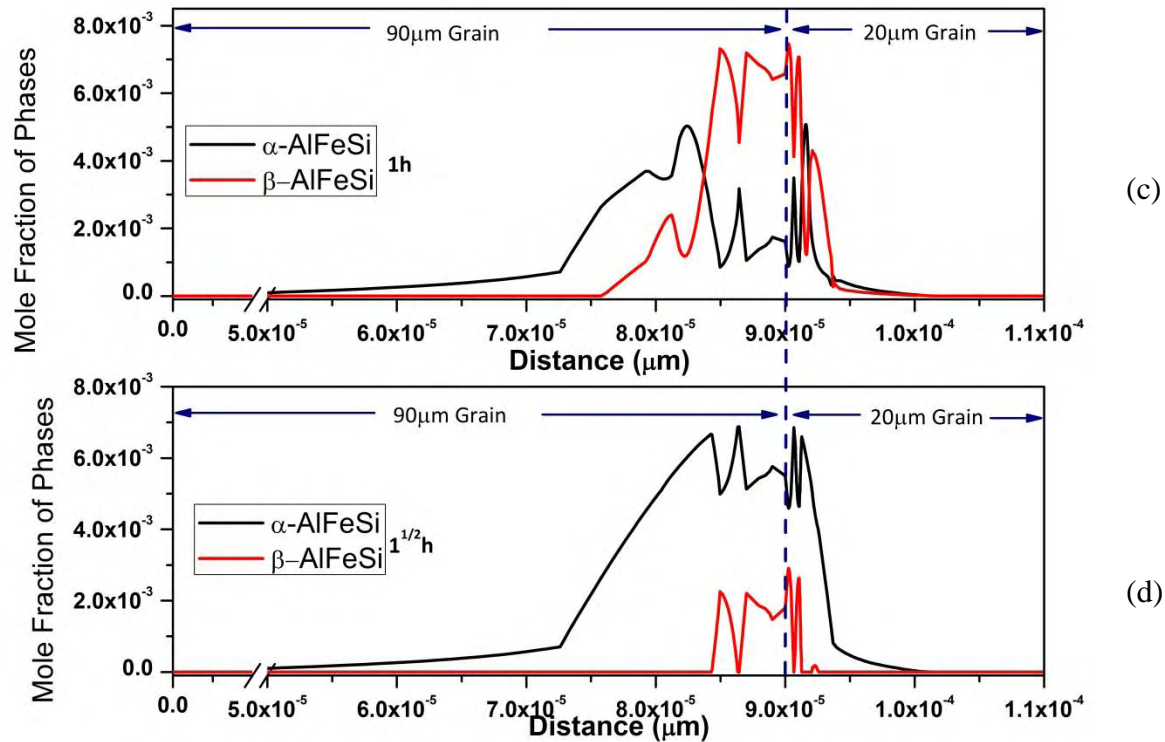
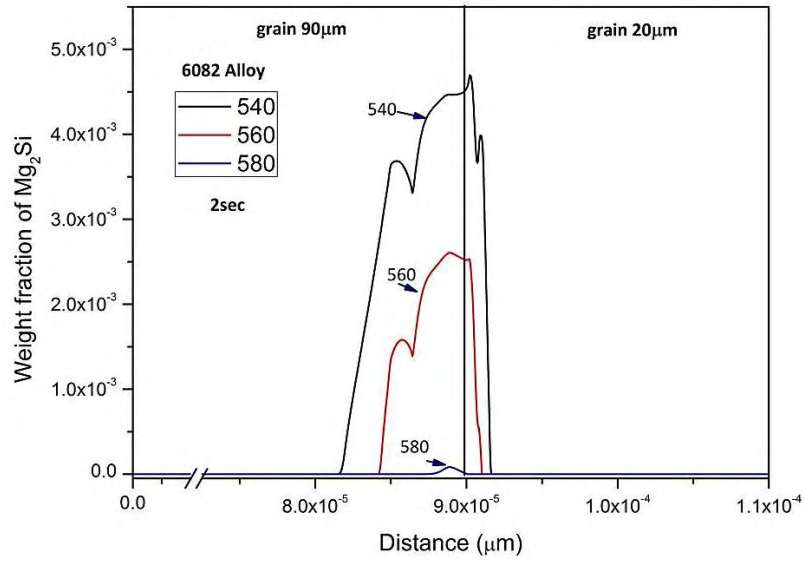


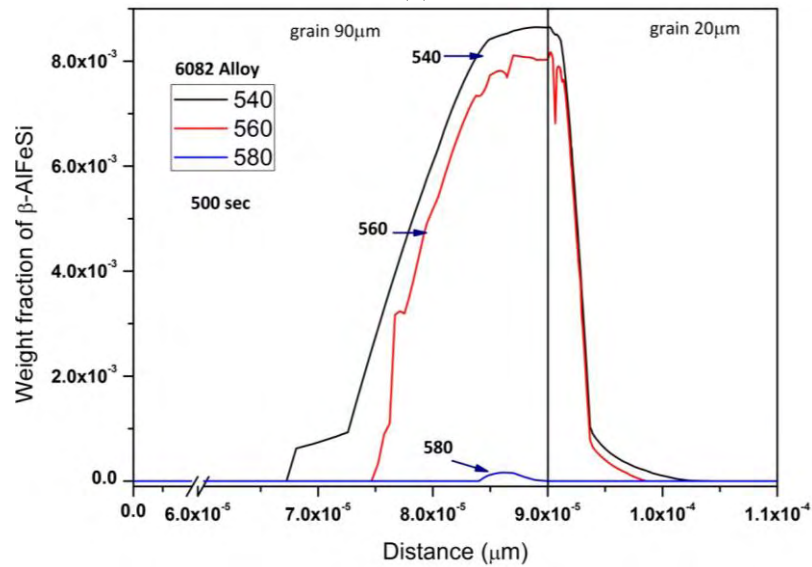
Figure 3.7: Spatial evolution of  $\beta \rightarrow \alpha$ -AlFeSi transformation during homogenization for times a) 15 b) 45min c) 1h d) 1 1/2 h

#### 3.4.4. The effect of temperature and grain size

The effect of homogenization temperature and grain size on the dissolution of the  $\text{Mg}_2\text{Si}$  and the transformation of  $\beta \rightarrow \alpha$ -AlFeSi has been studied. As stated above, grain size influences the transformation kinetics since it controls the distance over which diffusion of alloying elements takes place. Homogenization temperature influences the diffusion rate. For the 6082 alloy the weight fraction of  $\text{Mg}_2\text{Si}$  phase is depicted in Figure 3.8a for 3 different homogenization temperatures, 540, 560 and 580°C for homogenization time  $t=2\text{sec}$ . It is obvious that the  $\text{Mg}_2\text{Si}$  dissolution is much faster at the high homogenization temperature. Similarly the weight fraction of  $\beta$ -AlFeSi phase is depicted in Figure 3.8b for the same temperatures and for homogenization time  $t=500\text{sec}$ . It is also evident that the transformation rate increases with the homogenization temperature.



(a)



b)

Figure 3.8: The weight fraction of a)  $\text{Mg}_2\text{Si}$  phase and b)  $\beta\text{-AlFeSi}$  phase for 3 different homogenization temperatures, 540, 560 and 580°C for homogenization time  $t=2\text{sec}$  and 500sec respectively

Furthermore the dissolution of  $\text{Mg}_2\text{Si}$  and  $\beta\text{-AlFeSi}$  has a different transformation rate depending from the grain size. At 580°C and  $t=2\text{sec}$  the  $\text{Mg}_2\text{Si}$  dissolution has been completed only at the 20 $\mu\text{m}$  grain. The same stands the  $\beta\text{-AlFeSi}$  phase at  $t=500\text{sec}$ .



### 3.4.5. Removal of the microsegregation of the alloying elements

As stated in the introduction of this chapter, one of the aims of homogenization is the removal of microsegregation, which is present in the as-cast microstructure.

The evolution of the concentration profiles of Mg, Si, Fe and Mn in the FCC phase during homogenization at 540°C as predicted by the DGM model is given in Figure 3.9 a-d. The homogenization times considered are 0.5, 4, 8 and 32 hours. The  $t=0$  curve corresponds to the as-cast microsegregation profile (Scheil profile). The following remarks can be made:

- The concentration profiles for Mg, Si and Mn become more uniform with homogenization time. The profile for Fe does not change appreciably due to the very low diffusivity of Fe in Al.
- The average concentration of Mg and Si in the matrix interior (away from the boundary) increase with homogenization time. This explains the larger amount of  $Mg_2Si$  precipitated during cooling discussed in the previous section.
- The profiles homogenize faster in the smaller grain
- The compositional fluctuations close to the boundary are due to the dissolution of  $Mg_2Si$  and the  $\beta-AlFeSi \rightarrow \alpha-AlFeSi$  transformation. These fluctuations decay with homogenization time.
- The spatial evolution of the concentration profiles is consistent with the spatial evolution of the phase fractions.

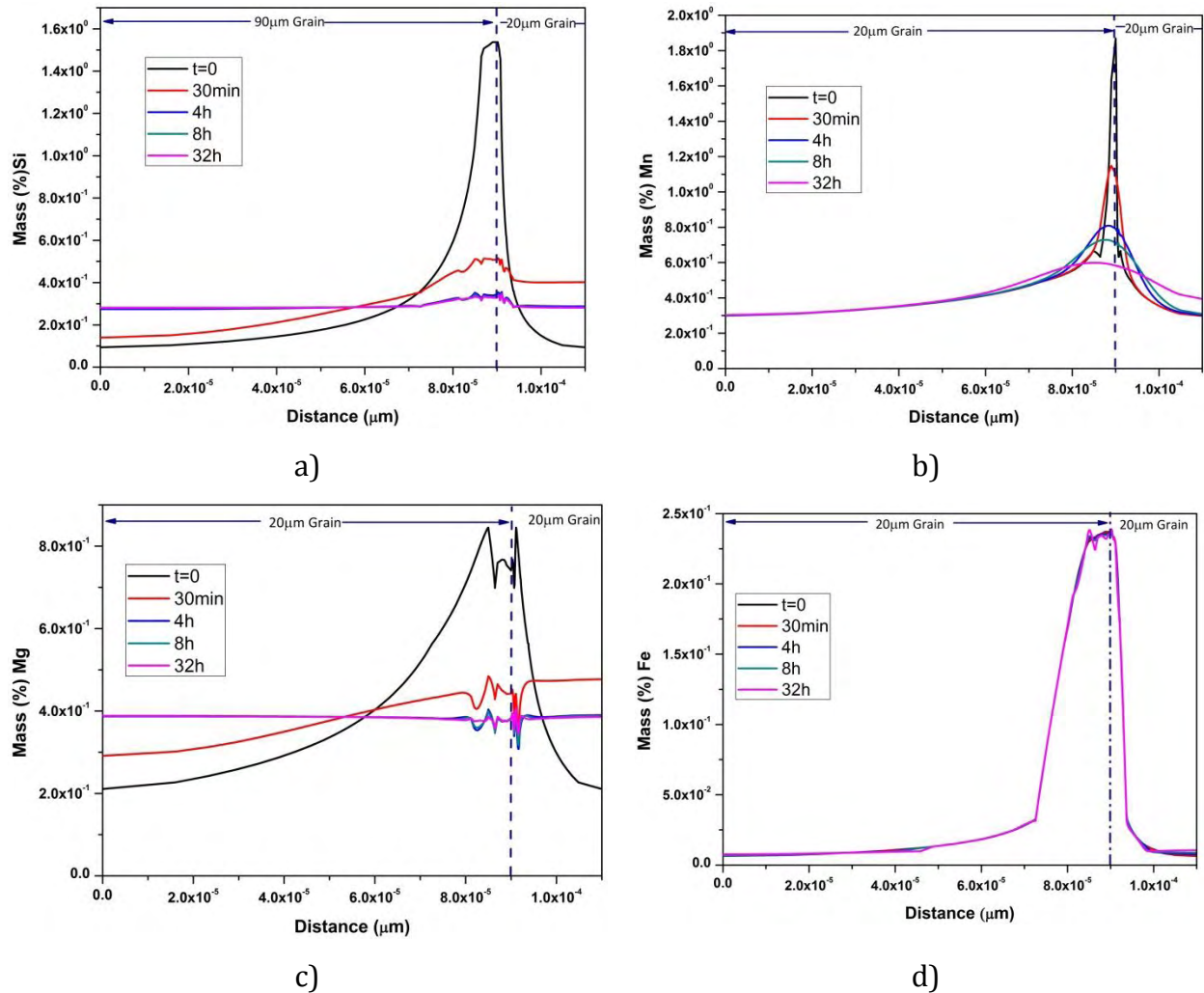


Figure 3.9: The evolution of the concentration profiles of Mg, Si, Fe and Mn in the FCC phase during homogenization at 540°C

### 3.4.6. Homogenization Process Map of extrudable 6xxx alloys

The main parameters of the homogenization process are the homogenization temperature and time. The selection of these parameters in industrial practice has been a matter of thorough investigation in the past. In line with the phase fraction mapping, presented in Chapter 2, a preliminary work is presented here as an initial effort to develop homogenization process map, which will aid the selection of process parameters. The map presented here regards the time for the  $\beta\text{-AlFeSi} \rightarrow \alpha\text{-AlFeSi}$  transformation. In order to develop the maps, the DGM model was employed, for a series of simulations. The results are presented as a function of the Mg:Si ratio in the alloy. The homogenization map based on



the  $\beta$ -AlFeSi $\rightarrow\alpha$ -AlFeSi transformation is shown in Figure 3.10. Three homogenization temperatures are considered, 540, 560 and 580°C. Except from the reduction of the  $\beta$ -AlFeSi $\rightarrow\alpha$ -AlFeSi transformation time with increasing the homogenization temperature, another interesting effect is indicated. It appears that the  $\beta$ -AlFeSi $\rightarrow\alpha$ -AlFeSi transformation time diminishes with the increase of the Mg:Si ratio in the alloy. This is consistent with the fact that Mg stabilizes the  $\alpha$ -AlFeSi phase and Si stabilizes the  $\beta$ -AlFeSi phase.

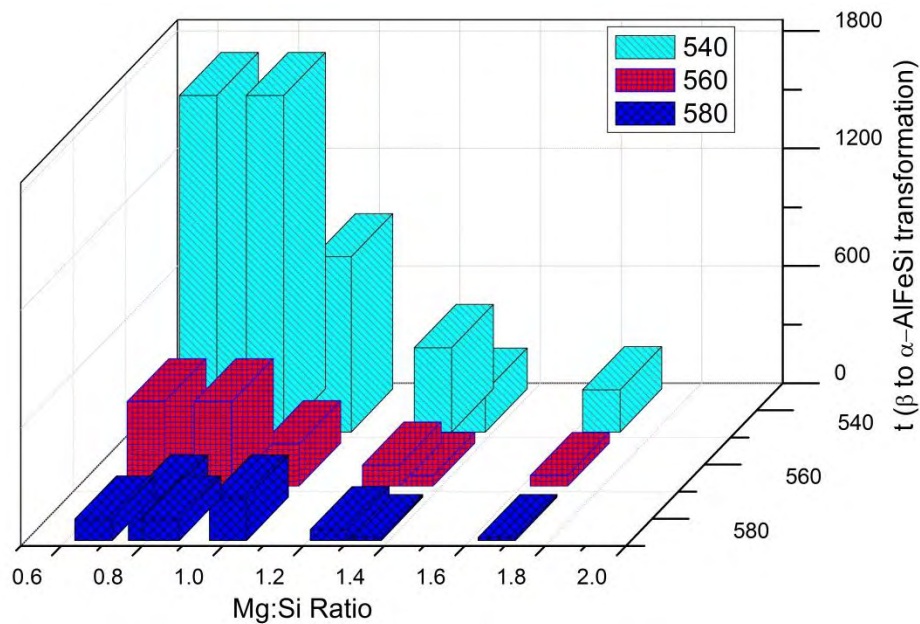


Figure 3.10: Homogenization process map of 6082 alloy based on the  $\beta$ -AlFeSi $\rightarrow\alpha$ -AlFeSi transformation

### 3.4.7. Experimental validation

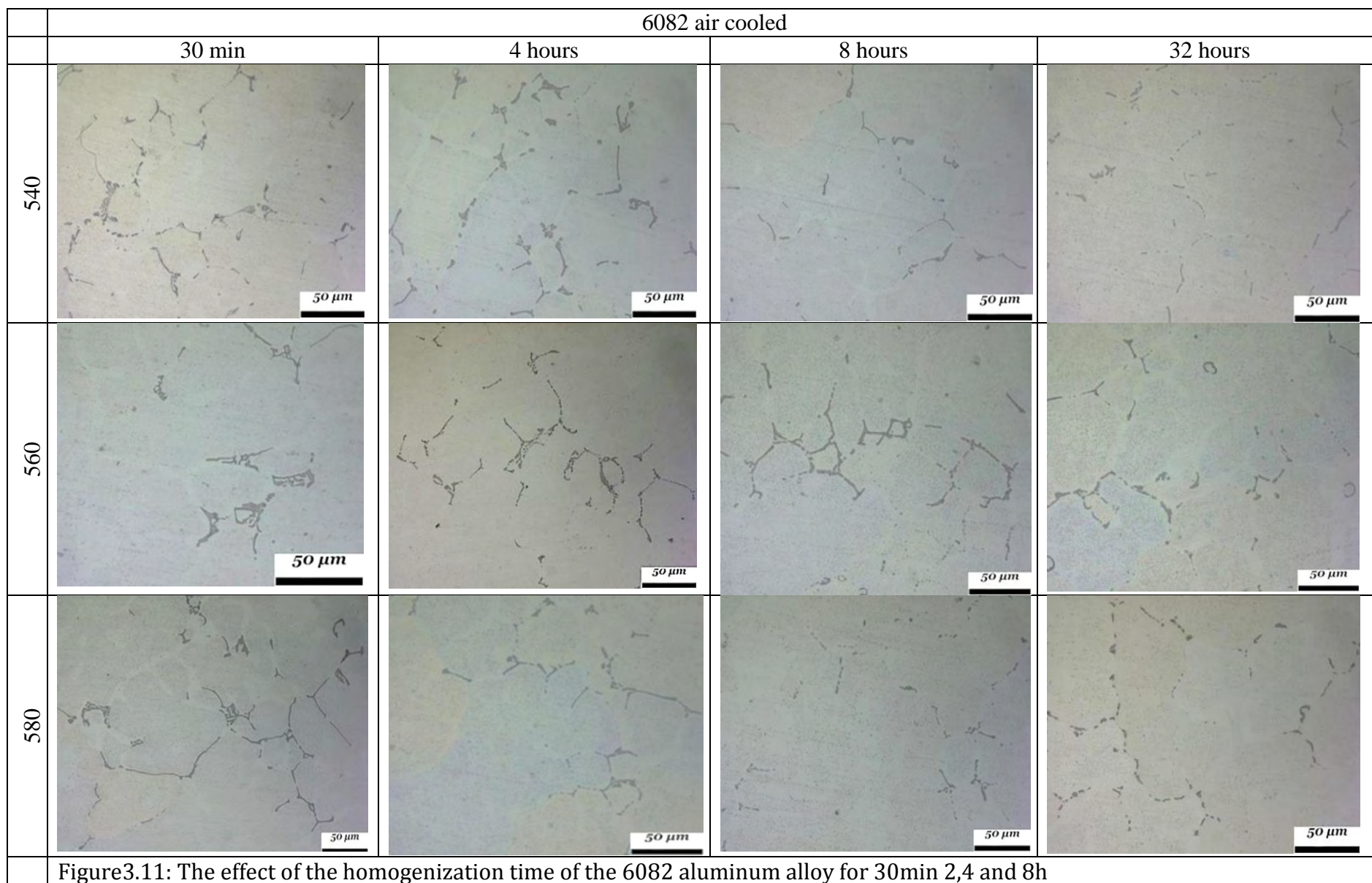
#### ❖ Homogenization 560°C AA6082 and AA6060

The purpose of this section is to provide the necessary experimental data, regarding the validation of the phase transformations take place during homogenization e.g Mg<sub>2</sub>Si dissolution,  $\beta\rightarrow\alpha$ -AlFeSi transformation and alloying element elimination.

As mention in previous chapter the validation was performed on alloys 6082 and on 2 6060 alloys. Homogenization heat treatments at 560°C for 30min, 4h, 8h and 32h have been applied. The microstructure was revealed using the procedure outlined above i.e. light

optical microscopy, SEM and EDS analysis and elemental area mapping. X-Ray Diffraction analysis was carried out in order to validate the evolution of intermetallic phases during homogenization treatment as predicted by the DGM model.

Regarding the evolution of the phases present in the microstructure of the 6082 aluminum alloy the effect of the homogenization time is depicted in Figure 3.11 for 30min, 2, 4 and 8h. The  $Mg_2Si$  strengthening phase has dissolved completely and reprecipitated in the grain interior during cooling from homogenization temperature.



SEM micrographs of 6082 alloy are shown in Figure 3.12 a-e. The sharp intermetallic phases of the as-cast microstructure become more rounded after homogenization. The reprecipitation of  $\text{Mg}_2\text{Si}$  in the grain interiors is evident in the micrographs.

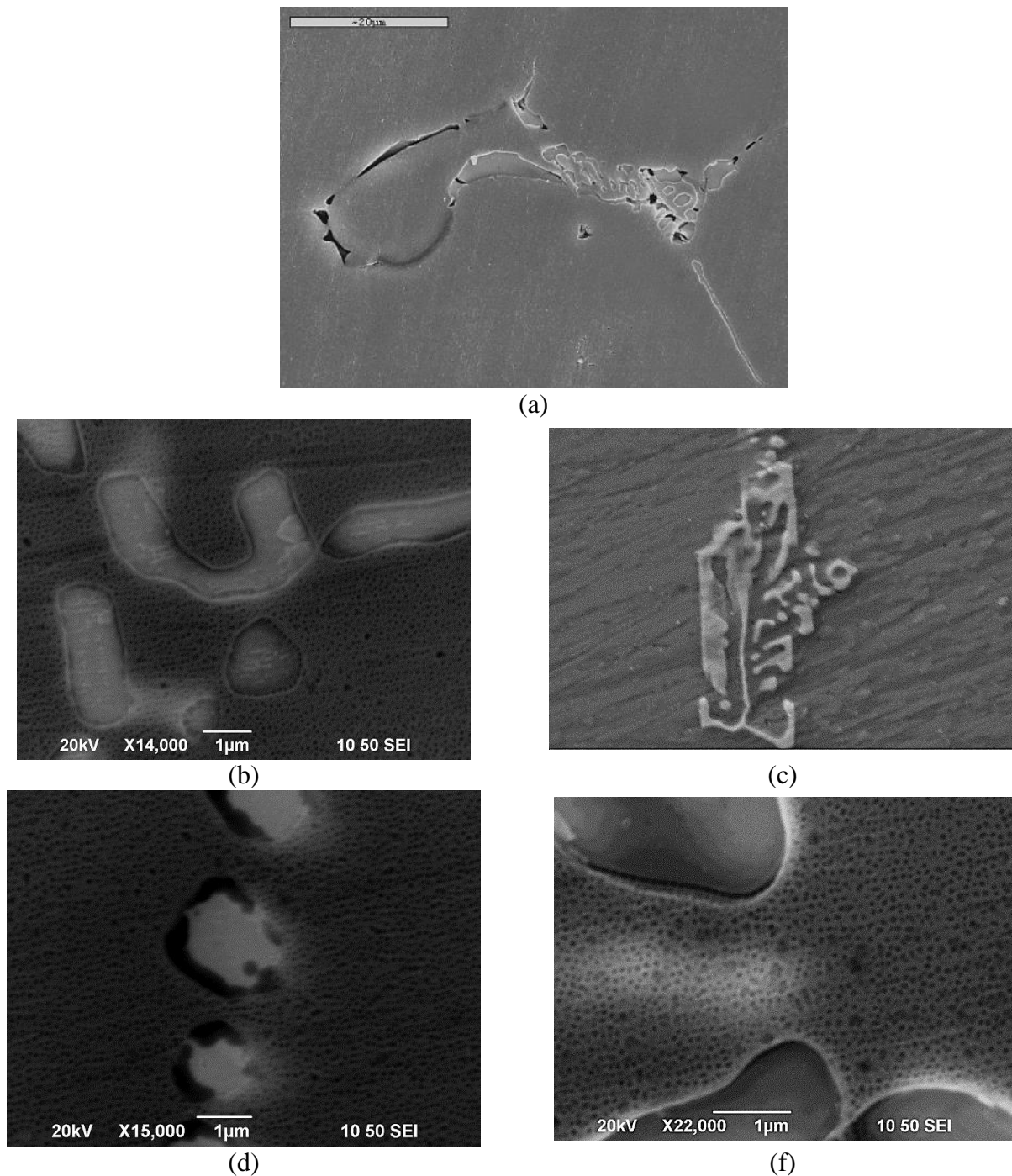


Figure 3.12: SEM micrographs of 6082 alloy a) as- cast condition b) 0.5, c) 4h, d)8h, e)32h



The homogenized microstructure of the 6060 aluminum alloy is depicted in Figure 3.13. After homogenization the transformation of the  $\beta$ -AlFeSi $\rightarrow\alpha$ -AlFeSi and dissolution of the Mg<sub>2</sub>Si phase has been completed.

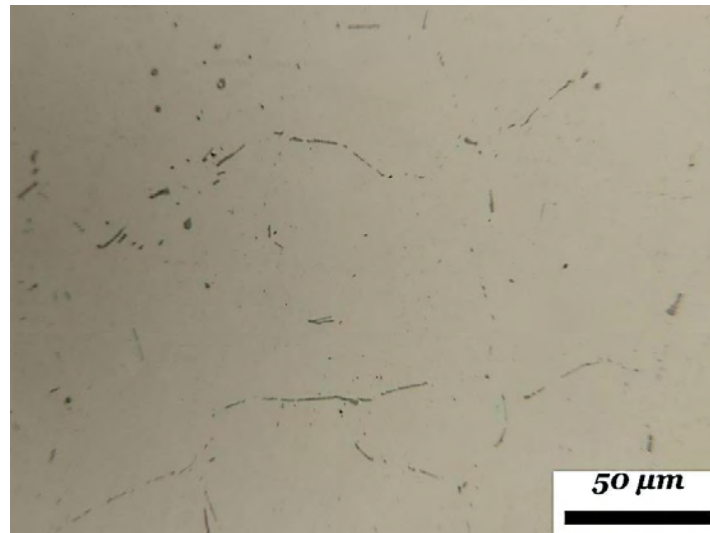


Figure 3.13: The homogenized microstructure of the 6060 aluminum

Furthermore more rounded  $\alpha$ -AlFeSi particles are evident as well as a neckless morphology depicted clearly in SEM micrograph in Figure 3.14a-b. The round-off or spheroidization as well as the development of a neckless morphology of the  $\alpha$ -AlFeSi phase are very important additional stages during homogenization and will be discussed extensively in Chapter 4.

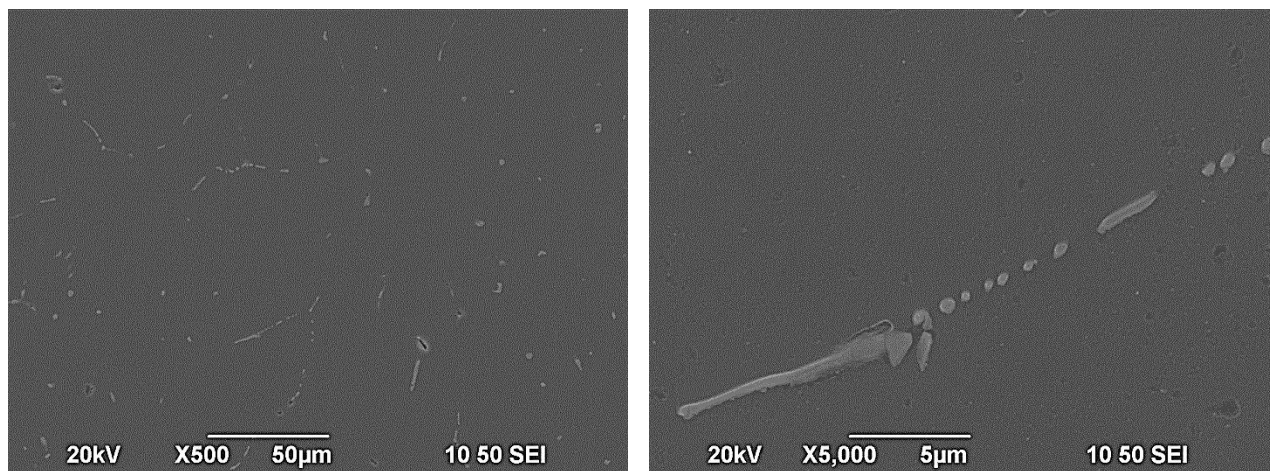


Figure 3.14: a) Rounded  $\alpha$ -AlFeSi particles and b) neckless morphology in SEM micrographs

### 3.4.8. Transformation $\beta$ -AlFeSi $\rightarrow$ $\alpha$ -AlFeSi

The  $\beta$ -AlFeSi $\rightarrow$  $\alpha$ -AlFeSi transformation was monitored experimentally with XRD. For the 6082 alloy an XRD spectrum was taken after 0.5, 4, 8 and 32h homogenization at 560°C and cooling to room temperature. The as-cast condition was also analyzed with XRD. The results appear in Figure 3.15. Diffraction peaks corresponding to the aluminum matrix, Mg<sub>2</sub>Si,  $\alpha$ -AlFeSi and  $\beta$ -AlFeSi are evident. The  $\beta$ -AlFeSi peaks are replaced by  $\alpha$ -AlFeSi peaks in the 0.5h spectrum. This does not mean that the transformation is completed in 0.5 hours. It is more probable that at 0.5 hours the fraction of the  $\beta$ -AlFeSi phase is small and beyond the detection limit of the XRD.

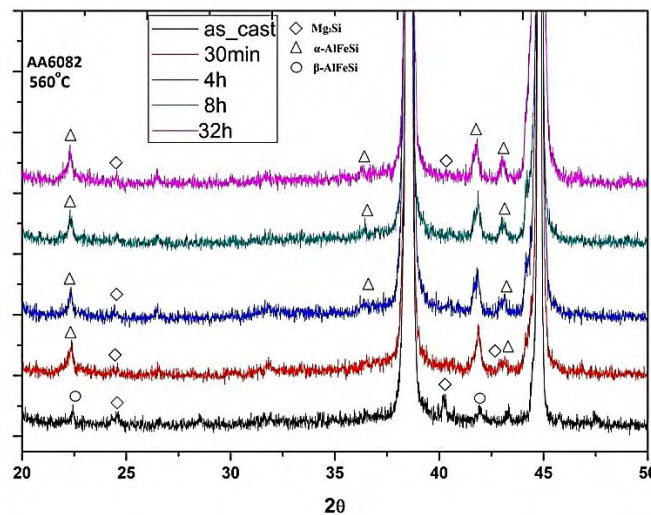


Figure 3.15: XRD spectrum of the  $\beta$ -AlFeSi $\rightarrow$  $\alpha$ -AlFeSi transformation of 6082 alloy

The XRD spectrum for the 6060 alloy homogenized at 560°C for 0.5h is depicted in Figure 3.16. The  $\beta$ -AlFeSi peaks have been replaced with  $\alpha$ -AlFeSi peaks, indicating that the transformation has been completed. The above results are in general agreement with the DGM simulation results.

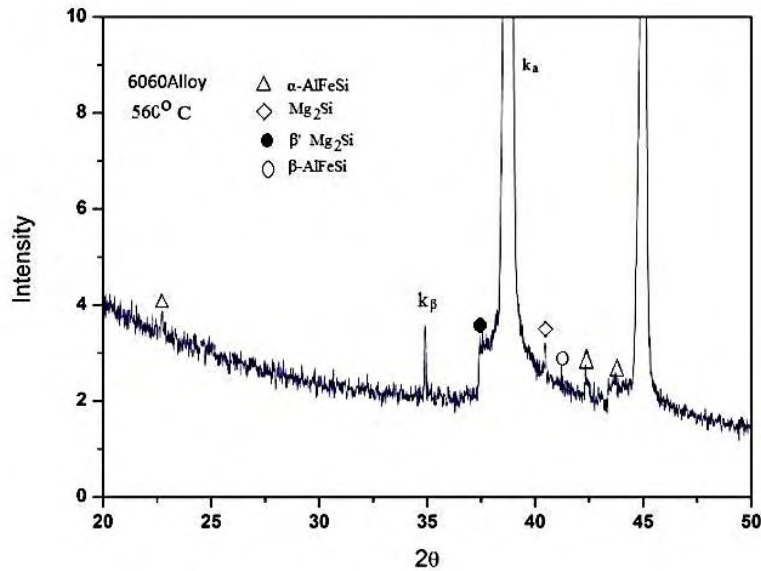


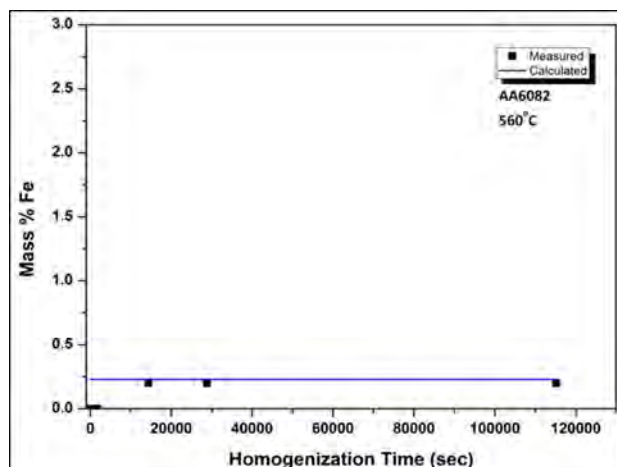
Figure 3.16: The XRD spectrum for the 6060 alloy homogenized at 560°C for 0.5h

### 3.4.9. Evolution of elemental profiles during homogenization

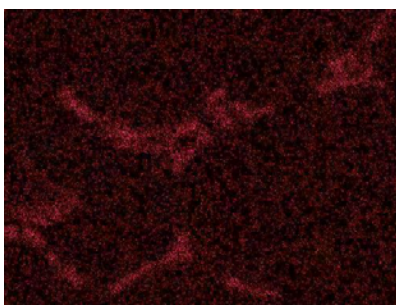
In order to experimentally validate the DGM predictions regarding the removal of microsegregation (presented in 3.4.5 above), area analysis vs homogenization time and elemental mapping were performed with EDS analysis. The area analysis was performed in the matrix close to the boundary. The results are presented for each element in Figures 3.17-20.

#### ❖ Profile and mapping for Fe

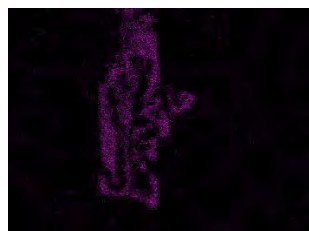
Due to the low diffusivity of Fe in Al, the Fe concentration does not change with homogenization time. The simulation results are in agreement with the experimental data as shown in Figure 3.17 a. The mapping depicted in Figure 3.17b-f indicates that Fe is mostly concentrated in the  $\alpha$ -AlFeSi phase.



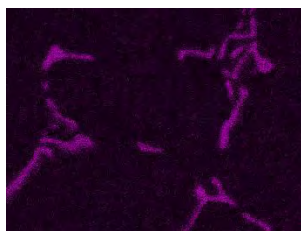
(a)



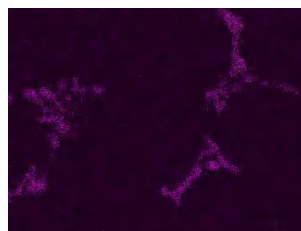
(b)



(c)



(d)



(e)



(f)

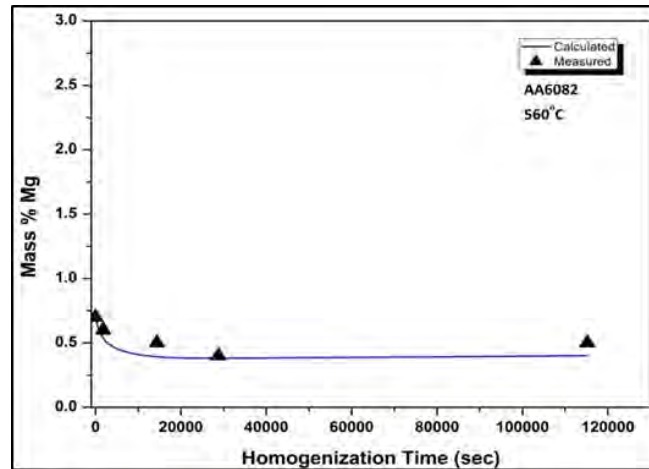
Figure 3.17: a) Simulation results and experimental for Fe element, b) profile mapping in as – cast condition, c) 0.5h, d) 4h, e) 8h, f) 32h homogenization time

### 3.4.10. Profile and mapping for Mg

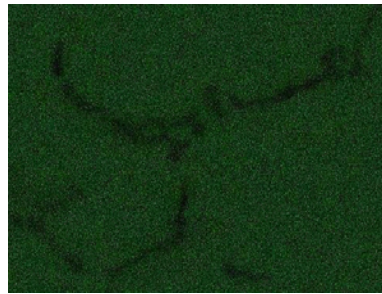
As indicated in Figure.3.18, the agreement between the simulation result and the experimental data regarding the evolution of the Mg concentration with homogenization time is good. The mapping for Mg indicates that Mg is absent from the boundary regions



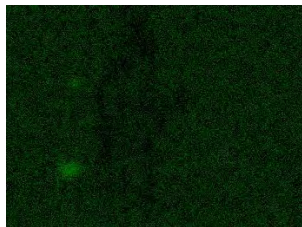
where the iron intermetallics form. The spread of Mg in the matrix with homogenization time is evident and is due to the diffusion of Mg to the grain interior.



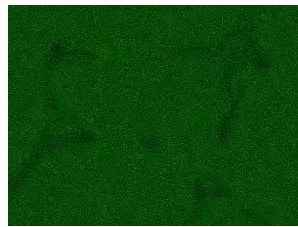
(a)



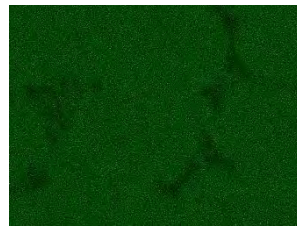
(b)



(c)



(d)



(e)



(f)

Figure 3.18: a) Simulation results and experimental for Mg element, b) profile mapping in as – cast condition, c) 0.5, d) 4h, e) 8h, f) 32h homogenization time

### 3.4.11. Profile and mapping for Si

As shown in Figure 3.19, the evolution of Si concentration with homogenization time follows a similar trend with Mg. Although the DGM model shows a similar trend with the

experimental values, i.e. a reduction with homogenization time, the DGM underestimates the Si at higher homogenization times. This discrepancy could be attributed to the Si coming from the dissolution of the Si-diamond phase, which is present in the as-cast microstructure.

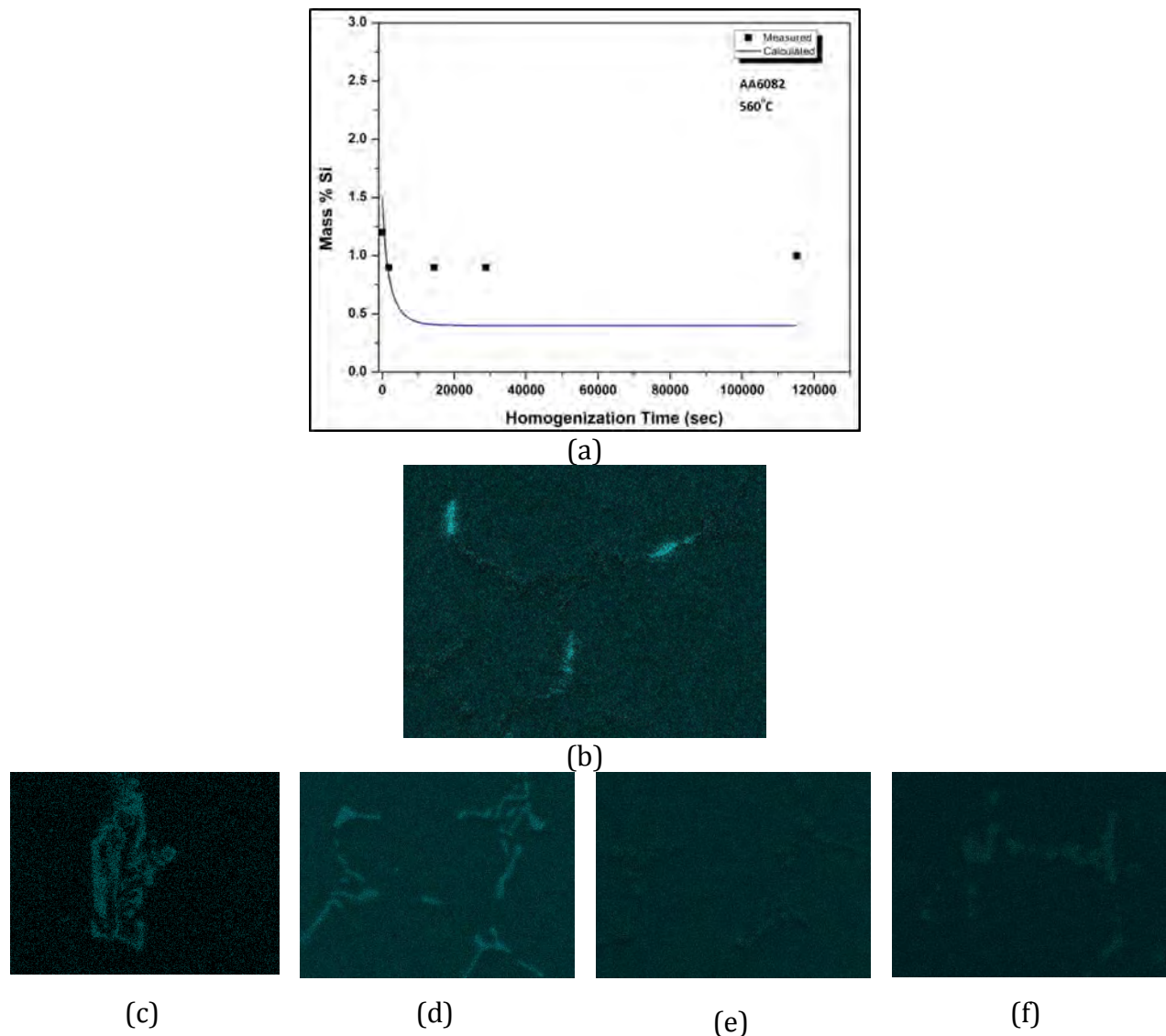
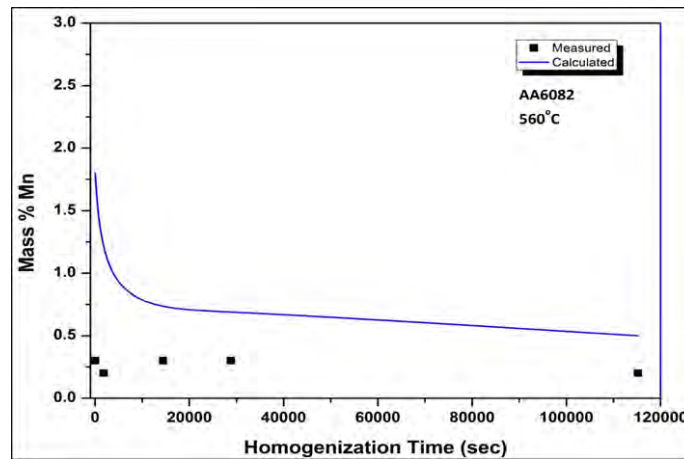


Figure 3.19: a) Simulation results and experimental for Si element, b) profile mapping in as-cast condition, c) 0.5h, d) 4h, e) 8h, f) 32h homogenization time

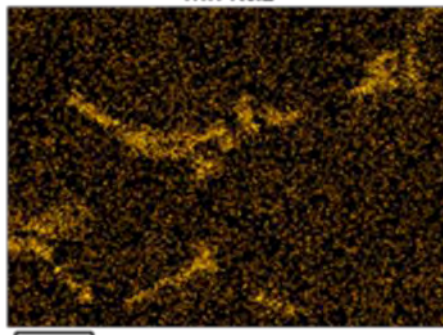
### 3.4.12. Profile and mapping for Mn

As shown in Figure 3.20, the DGM model overestimates the Mn concentration in the matrix especially at the short homogenization times, the difference decreases at longer

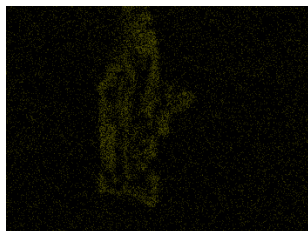
times. As indicated from the mapping, there is a strong Mn signal in the  $\alpha$ -AlFeSi phase. Therefore this discrepancy is due to the Mn retained in the  $\alpha$ -AlFeSi phase and to the fact that the thermodynamic description of the  $\alpha$ -Al(Fe,Mn)Si phase is not yet optimized.



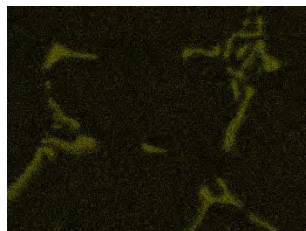
(a)



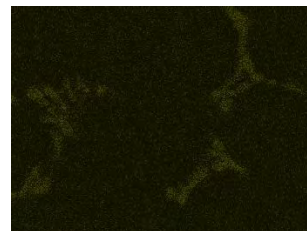
(b)



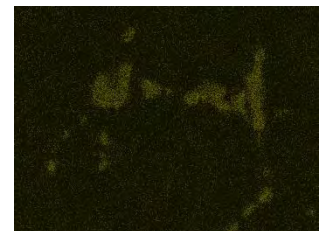
(c)



(d)



(e)



(f)

Figure 3.20: a) Simulation results and experimental for Mn element, b) profile mapping in as – cast condition, c) 0.5, d) 4h, e) 8h, f) 32h homogenization time

### 3.5. Conclusions

From the work presented above the following conclusions can be drawn:

The DGM model has been developed to treat the homogenization process in multicomponent and multiphase Al-alloys exhibiting a large variability of the as-cast grain size. With the model it is possible to simulate the temporal and spatial evolution of phase fractions and element concentration during homogenization.

Regarding the evolution of phase fractions during homogenization, the predictions of the DGM model have been validated experimentally with XRD analysis. The evolution of the  $\beta$ -AlFeSi $\rightarrow$  $\alpha$ -AlFeSi transformation is predicted by the DGM and is confirmed by XRD in the same time scale.

The DGM predictions regarding the evolution of Fe and Mg concentrations with homogenization time are in excellent agreement. There are only some discrepancies in the profiles of Si and Mn. The Si discrepancy is due to the Si-diamond phase not taken into account in the DGM. The Mn discrepancy is due to the Mn retention in the  $\alpha$ -AlFeSi phase. The DGM predicts the fast dissolution of Mg<sub>2</sub>Si during homogenization and its re-precipitation during cooling. It also predicts its dissolution during preheating prior to extrusion.

The DGM can describe the temporal and spatial evolution of the  $\beta$ -AlFeSi $\rightarrow$  $\alpha$ -AlFeSi transformation. The spatial evolution exhibits an exact spatial correspondence. In addition the starts at a certain distance from the boundary and the transformation front moves towards the boundary.

Both the Mg<sub>2</sub>Si dissolution and the  $\beta$ -AlFeSi $\rightarrow$  $\alpha$ -AlFeSi transformation are faster in the smaller grain as predicted by the DGM. In addition the concentration profiles of the elements homogenize faster in the smaller grain.

The DGM predicts correctly the effect of homogenization temperature, with the rate of both the Mg<sub>2</sub>Si dissolution and the  $\beta$ -AlFeSi $\rightarrow$  $\alpha$ -AlFeSi transformation to increase with the homogenization temperature.

A preliminary attempt to develop homogenization process maps has been performed using the DGM. These maps are, at present, based on Mg<sub>2</sub>Si dissolution and the  $\beta$ -AlFeSi $\rightarrow$  $\alpha$ -AlFeSi transformation and can be used for the design of the homogenization heat treatment.

### 3.6. References

- [1] B. Rinderer Mat Sc F. (2011) 264-275
- [2] A. L. Dons, Journal of Light Metals 1 (2001) 133-149.
- [3] G.Mrówka-Nowotnik, Mech. and Mater. Eng. (2005)
- [4] Li YJ, Arnberg L. Acta Mater (2003) 51-3415.
- [5] Li YJ, Arnberg L. Mater Sci Eng A (2003), 347-130.
- [6] Q. Du W.J. Poole, M.A.Wells, N.C. Parson, Acta Materialia 61 (2013) 4961-4973.
- [7] Yan, L.-Z., Zhang, Y.-A., Li, X.-W., Li, Z.-H., Wang, F., Liu, H.-W., Xiong, B.-Q, Trans., Nonf. Met. Soc. Of Ch. 24 (2014) 939-945.
- [8] Cieslar, M., Bajer, J., Hájek, M., Očenášek, V. TMS Light Metals (2014), 237-241.
- [9] P.K. Saha P.K., ASM International, (2000).
- [10] N. C. W. Kuijpers, Ph.D.Thesis, TUDelft (2004)
- [11] Sheppard, Kluwer Academic Publishers, (1999).
- [12] S. Zajac, B. Bengtsson, C. Jonsson, Mat. Sc. Forum, Trans Tech, Switzerland, (2002)
- [13] Kemal Deliji, Vanja Asanovi, Dragan Radonji, MTAEC9, 39 (4) (2005) 101
- [14] Polmear I.J., 'Light Alloys, Metallurgy of the Light Metals', Arnold, (1995).
- [15] J. V. Langkruis, Ph.D. Thesis, TUDelft, (2000).
- [16] O.Reiso, Ph.D. Thesis, Norwegian Institute of Technology, (1992).
- [17] Halfdan Kristoffer Småbråten, Master thesis, Norwegian University of Science and Technology, (2011)
- [18] G. M.-Nowotnik, J. Sieniawski, Jour. Mat. Proc. Tech., (2005) 367-372,
- [19] S.N Samaras, G.N Haidemenopoulos, Jour., Mat., Proc., Techn. 194 (2007), 63-73
- [20] Y. Birol, Jour., Mat., Proc. Tech. 148, (2004). 250-258
- [21] Y. Birol, Met., Mat., Int. 20 (2014), 727-732.
- [22] S.N. Samaras, PhD thesis, University of Thessaly Mech. Eng. (2006)
- [23] N.C.W Kuijpers, Mat., Sc., Eng. A (2005), 394, 9-19.
- [24] G.N Haidemenopoulos, H Kamoutsi, A.D Zervaki, Jour., Mat., Proc., Techn., 212, (2012), 2255-2260.
- [25] A. Borgenstam, L. Hoglund, J. Egren, A. Engstrom, Jour. Ph. Equil. 21, (2000) 269-280
- [26] Kinetics of materials, Book
- [27] G. Inden, V. Ghetta (ed), Spr. (2008), 113-139.
- [28] A. Engstrom, L. Hoglund, J. Agren, Met., Mat., Trans. 25A (1994) 1127-1134.





## 4. Quantification of Homogenization state

### 4.1. Introduction

As discussed in Chapter 3 the aim of homogenization is to reduce the microsegregation of elements and phases that are concentrated at grain boundaries and interdendritic areas. In 6xxx alloys the undesirable  $\beta$ -AlFeSi intermetallic phase, which limits extrudability, transforms to a more rounded  $\alpha$ -AlFeMnSi intermetallic phase during homogenization. After the transformation  $\beta \rightarrow \alpha$ -AlFeSi is complete, the  $\alpha$  phase undergoes coarsening and spheroidization, adopting a “necklace” morphology, which enhances the extrudability of the billet. This explains the fact that the actual homogenization times in industrial practice are longer than the times required for  $\text{Mg}_2\text{Si}$  dissolution and the completion of the  $\beta \rightarrow \alpha$ -AlFeSi transformation. The morphological changes of the  $\alpha$ -AlFeSi phase have only been described qualitatively in the published literature and a “quantification” of the homogenization state does not exist. In this chapter the homogenization state has been quantified by means of quantitative metallography in order to describe the morphology of the intermetallic phases. An index-based methodology has been developed. The aspect ratio and circularity are two indices, among others, that can be used to characterize the homogenization state. These parameters can be determined by quantitative metallography, involving image analysis. A fully homogenized billet, with the potential for high extrudability should have all  $\beta$ -AlFeSi transformed to  $\alpha$  with necklace morphology and appropriate values of aspect ratio and circularity.

### 4.2. Literature review

As discussed in previous chapters the presence of intermetallic phases with sharp edges can impair the deformability of 6xxx extrudable alloys especially when located in the grain boundary regions [1-4]. Extrudability is qualitatively defined by the maximum production speed attainable for a given press capacity while still obtaining the desired mechanical properties, surface quality and geometric tolerances of the extrudate. As

described earlier, the extrudability increases due to the  $\beta$  to  $\alpha$  transformation. The sharp tips of the  $\beta$  particles initiate micro-cracks during the deformation and, therefore, lead to surface cracking of the extrudate. The transformed  $\alpha$ -particles are more rounded and therefore cause less local cracking at the surface.

Although there have been a number of investigations on the homogenization treatment of 6xxx series aluminum alloys in recent years, most of the research has been focused on the evolution of microstructure as discussed extensively in Chapter 3 (see literature review Ch3). Moreover there has been no comprehensive quantitative study on the definition of homogenization state where the dependence of intermetallic phases and their morphology during the homogenization is investigated. The correlation of extrudability and intermetallic phase morphology has been investigated only qualitatively. Studies have been made on the microstructural evolution during the homogenization of AA7020 aluminum alloy concerning the dissolution of detrimental particles, which degrade the hot workability of the AA7020 alloy e.g phases and grain boundary (GB) particles during homogenization treatment [5-7]. It was found that the dominant process is the spheroidization of the GB particles; together with the decrease in the width of the GB particles, spheroidization was considered a key mechanism in the microstructural evolution during homogenization [1, 8, 9]. In the present thesis the state of homogenization has been quantified by determining specific indices by means of quantitative metallography. The study was performed for the 6060\_3 variant of a 6060 alloy. The methodology and results are described below.

### **4.3. Methodology**

The chemical composition of the 6060\_3 alloy investigated is shown in Table 2.2 (Chapter 2). Three homogenization heat treatments, in laboratory scale, were investigated, following the simulation conditions from Chapter 3, holding at 540°, 560°, and 580°C for 4h followed by air cooling (Table 4.1). These conditions ensured the complete transformation of  $\beta \rightarrow \alpha$ -AlFeSi.



Table 4.1 Homogenization heat treatments

| <b>Alloy</b> | <b>Condition</b> | <b>Homogenization Temperature (°C)</b> | <b>Homogenization Time (h)</b> |
|--------------|------------------|--|--------------------------------|
| 6060_3       | As-Cast          | -                                      | -                              |
| 6060_3A      | Homogenized      | 540                                    | 4                              |
| 6060_3B      | Homogenized      | 560                                    | 4                              |
| 6060_3C      | Homogenized      | 580                                    | 4                              |

#### 4.3.1. Quantitative metallography




After the homogenization heat treatment, the specimens were prepared for standard metallographic examination involving optical microscopy, SEM and image analysis as discussed in previous Chapters, in order to reveal the microstructure. The as-cast as well as the homogenized microstructures were characterized for intermetallic phases and the particles were categorized in three morphological types as rounded particles, pinched particles and particles exhibiting a neckless formation. It should be noted that pinched particles are those that are in the initial stage of separation in smaller rounded particles towards the formation of a neckless group. The number of images processed and the number of particles measured for each alloy appears in Table 4.2.

Table 4.2: Number of images analyzed and number of particles measured per billet for the quantification of the homogenization state

| <b>Alloy</b> | <b>Number of Images</b> | <b>Number of particles</b> |
|--------------|-------------------------|----------------------------|
| 6060_3       | 58                      | 106                        |
| 6060_3A      | 57                      | 161                        |
| 6060_3B      | 56                      | 150                        |
| 6060_3C      | 58                      | 133                        |

The quantification of the homogenization state was based on the measurement of indices that describe the size and shape of the intermetallics and indicate the state of homogenization. The indices employed were the following and are shown in Table 4.3:

Table 4.3: The indices employed for the quantification of the homogenization state

|                          |  |                                |   |
|--------------------------|--|--------------------------------|---|
| Aspect ratio             | A ratio of the major to the minor diameter of a particle, which can be used when the major axis does not cross a particle outline.                         | $AR = \frac{d_{max}}{d_{min}}$ |  |
| Ferret                   | The longest caliper length   |                                |  |
| Circularity              | Circularity is a measure of how closely a particle resembles a circle. It varies from zero to one in magnitude with a perfect circle having a value of one | $C = \frac{p^2}{4\pi A}$       |  |
| Circularity of the edges | Same as circularity but more sensitive on the edges when the length of a particle does not change  | $C = \frac{p^2}{4\pi A}$       |   |

### 4.3.2. Image analysis

After the standard metallographic observation, a higher magnification and resolution of the particles, through the use of SEM analysis, have been applied and shown in Figure 4.1a for a group of particles. It is important to use the appropriate magnification with a suitable numerical aperture [10] Fig4.1b. The Image J software display is depicted in Fig4.1c while Table 4.4 shows the respective measurements for each particle in the group.

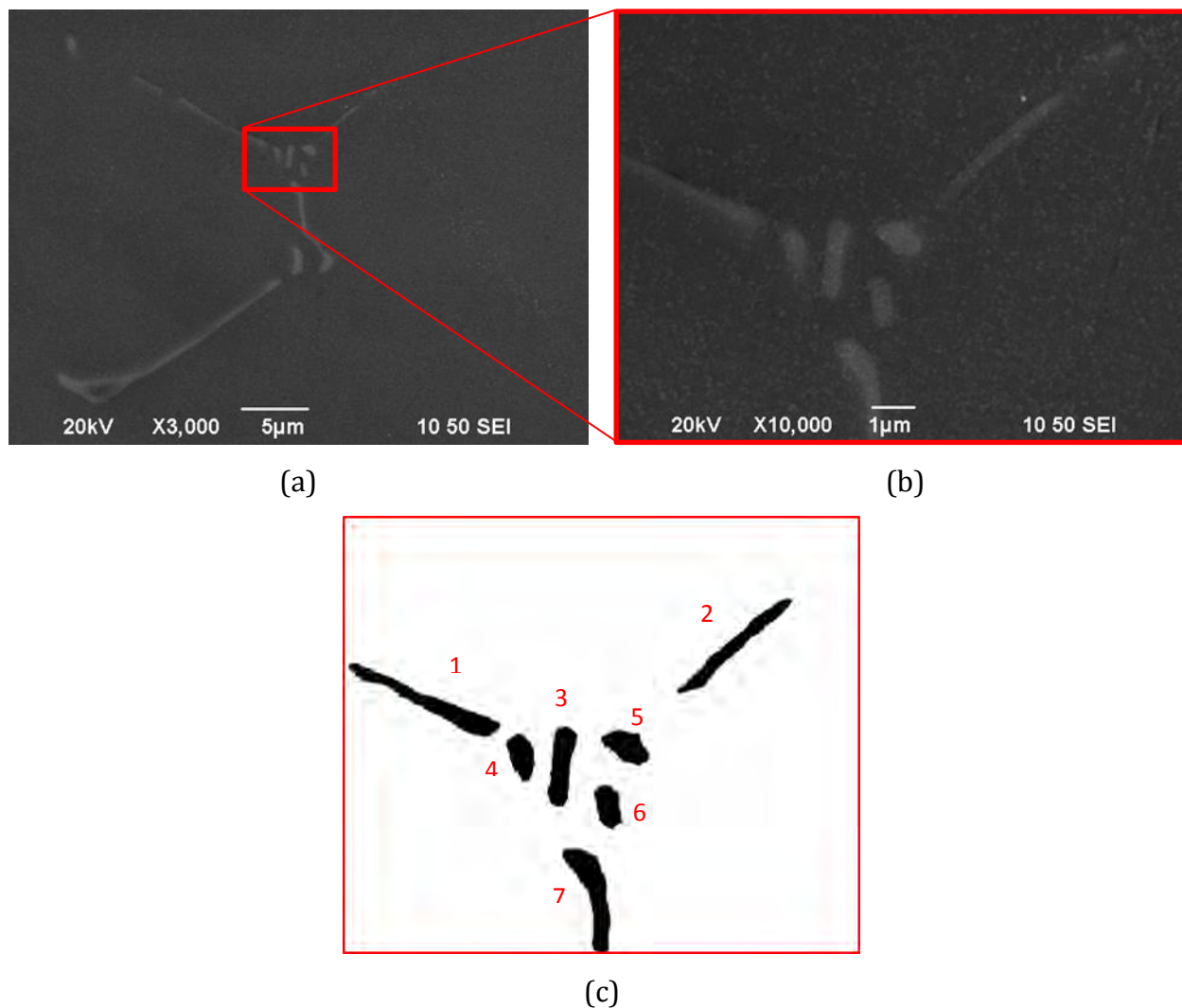


Figure 4.1: SEM image used for the measurement of indices: (a) Low magnification image, (b) high magnification isolation of the group of particles, (c) image J display used for the measurement of the indices

Table 4.4: Respective measurements for each particle referring to Figure 4.1

| No | Diam(max) | Diam(min) | Circularity | Perimeter | Area<br>(polygon) | Feret(max) |
|----|-----------|-----------|-------------|-----------|-------------------|------------|
| 1  | 3.289     | 0.574     | 5.200       | 7.427     | 0.844             | 3.308      |
| 2  | 3.655     | 0.376     | 5.190       | 8.405     | 1.083             | 3.656      |
| 3  | 1.792     | 0.389     | 2.103       | 4.395     | 0.735             | 1.793      |
| 4  | 1.123     | 0.632     | 1.439       | 3.080     | 0.524             | 1.160      |
| 5  | 1.069     | 0.534     | 1.433       | 2.820     | 0.441             | 1.068      |
| 6  | 0.976     | 0.489     | 1.384       | 2.712     | 0.423             | 1.000      |
| 7  | 2.369     | 0.526     | 2.764       | 6.027     | 1.045             | 2.482      |

#### 4.3.3. Statistical Analysis

In order to have credible results that could allow comparison between homogenization treatments, a large number of particles were measured. The area of measurement (scanned area) was kept constant for all homogenization treatments. In order to get credible results the data were processed statistically. In order to decide if the samples were comparable, the Kruskal-Wallis test was used. The Kruskal-Wallis test [11] is a non-parametric method for testing whether samples originate from the same distribution and it is used to compare two or more independent samples of equal or different sample size. With a confidence level of 99% it was proved that the samples derive from different distributions. As a result the samples are not comparable without further processing. In order to compare between the dissimilar samples, the “Bootstrapped Mean” [12] method was used. Bootstrapping is a non-parametric statistical technique that allows accurate estimations about the characteristics of a population to be made, when the examined sample size is limited. As it is non-parametric, the method can be used to compare between samples derived from different distributions, such as Normal and LogNormal distributions. It works by recursively calculating the preferred parameter, like the mean or the median, for a part of the sample and then combining the results to make robust estimates of standard errors and confidence intervals of the population parameter. In this case a 95% confidence interval was used, while the standard error was kept to a minimum by using a

large number of iterations. This process leads to comparable statistical parameters for each measurement.

## **4.4. Results and Discussion**

The results of the quantification of homogenization heat treatment are presented in this section. Regarding the homogenization state of the alloys studied the effect of temperature is depicted in Fig.4.2a-d in the as cast condition, homogenized at 540°, 560° and 580°C respectively.

### **4.4.1. Metallographic Investigation**

The as-cast microstructure depicted in Fig. 4.2a and consists of characteristic “Chinese – script” morphology of intermetallic  $\alpha$ -AlFeSi phase. After homogenization treatment at 540°C and 560°C this morphology still remains in the microstructure. In the contrary, in the 580°C temperature the  $\alpha$ -phase seems to have reached a state of satisfactory spheroidization.

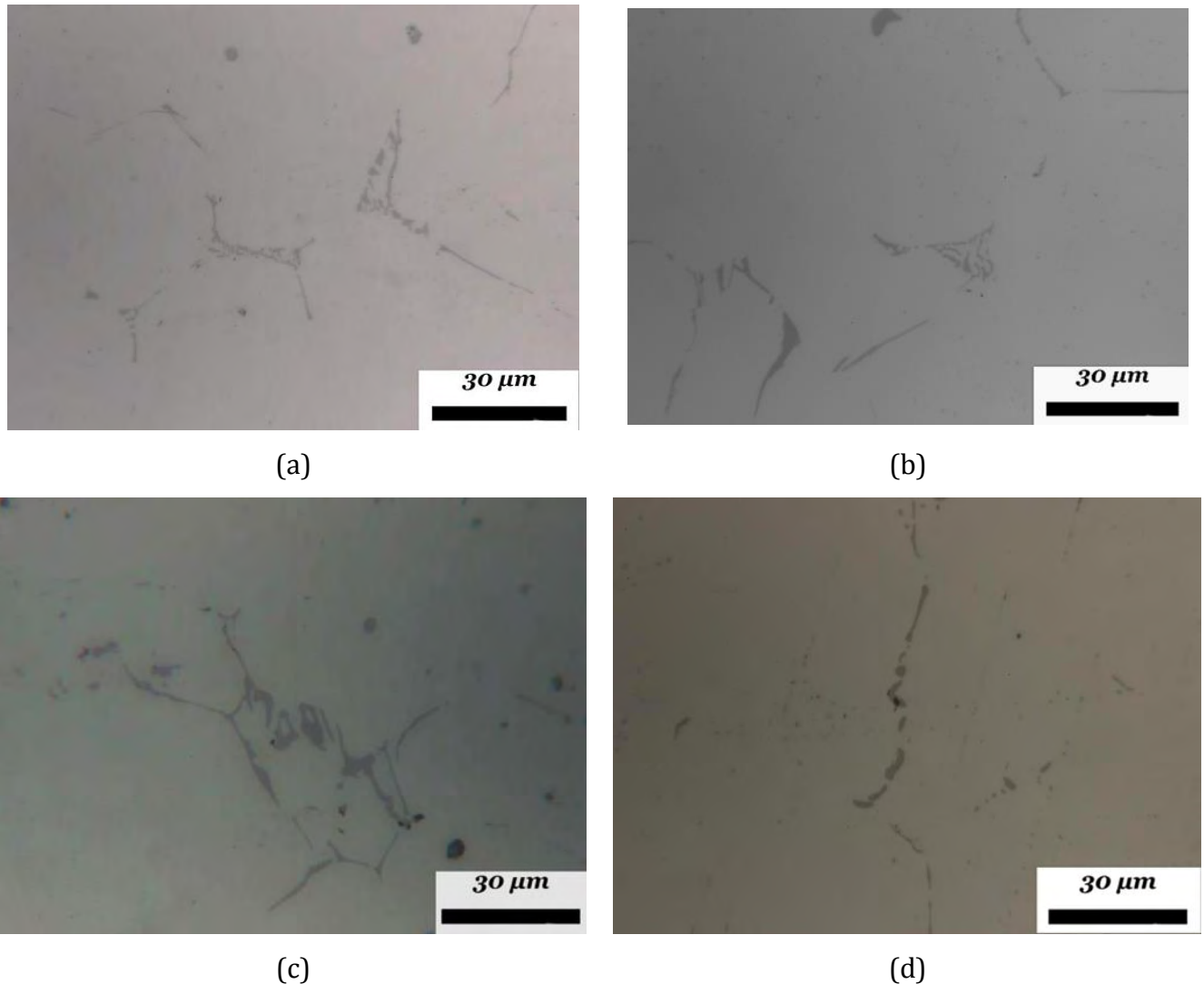


Figure 4.2: Metallographic images, (a) as-cast, (b) homogenized at 540°C, (c) 560°C and (d) 580°C

#### 4.4.2. Characterization of the particles

##### Three stages of morphological changes during homogenization

- 1st stage/ Rounded particles

As discussed in the previous section following the  $\beta$  to  $\alpha$ -AlFeSi transformation the intermetallic  $\alpha$ -phase undergoes spheroidization. In the first stage of this process the plate-like particles exhibit a slight decrease in their width. Although they do not exhibit complete

spheroidization the particles become more rounded at the edges Figure 4.3. It was found that this stage is more frequent for temperatures 540° and 560° C.

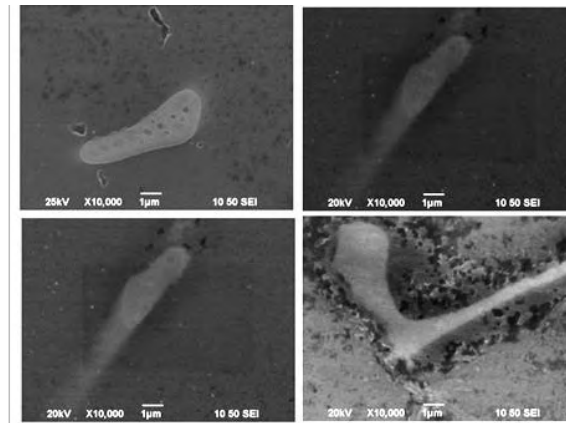


Figure 4.3: Images indicating the rounding of the edges of the particles during homogenization

- **2nd stage/ Pinched Particles**

At the second stage an initial perturbation can be observed in the particles. Particles take an ellipse shape with more rounded edges. This stage characterized by the trend of the particles to be separated into smaller rounded particles. These discontinuities are depicted in Figure.4.4. The driving force for this behavior is reduction of strain energy associated with large particles.

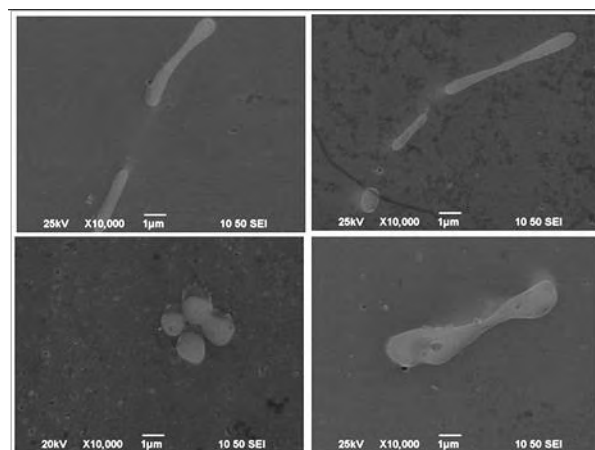


Figure 4.4: Imaged revealing the pinching process during homogenization

### 3rd Stage/ Neckless Particles

The reduction of surface energy of the  $\alpha$ -phase is the driving force for spheroidization. With this process, the total interface area between the matrix and the  $\alpha$ -AlFeSi phase is reduced. The particles finally adopt a spherical shape at the third stage as depicted in Figure. 4.5

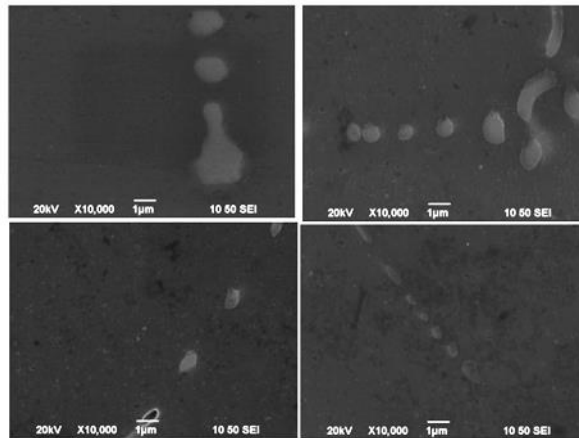


Figure 4.5: Images revealing the spherical shape at the third stage

It was found that for the two homogenization temperatures 540° and 560° C, although the morphological changes towards spheroidization were activated; only the first stage was completed. On the other hand for the homogenization at 580°C the  $\alpha$ -particles reached the third stage of spheroidization involving the neckless formation.

### 4.5. Results and discussion

The mean values of microstructural indices, Aspect ratio, Feret, Circularity and Circularity of Edges have been measured for all conditions investigated. The mean value reported possesses a 95% confidence while the upper and lower points are the 97.5% and 2.5% cut-offs to exclude extreme values. From these data, which are shown in Figure 4.6 a-d some general remarks can be made.

Regarding the Aspect Ratio (Figure 4.6a) the heat treatments of 6060\_3B and 6060\_3C alloys (560° and 580° C respectively) have a lower value compared to 6060\_3A alloy (540°C). However 3C alloy, has a lower Feret value (Figure 4.6b) and almost equal with 3A



alloy. This means that although the size of the particles is small for 3A and 3C alloys, the 3C alloy had more spheroidized particles.

The effect of homogenization temperature on the circularity of the particles is depicted in Fig 4.6c. Again 3C alloy has the lowest value. This is in a good agreement with the fact that 3C alloy reached the 3rd stage of spheroidization while alloy 3B reached the 2nd stage. Alloy 3A reached only the 1st stage, which explains the low value of circularity of edges (Figure 4.6d) as in that stage, particles exhibited an initial spheroidization at their edges. From the above analysis it is concluded that the treatment possessing homogenization indices for better extrudability is 580°C for 6060\_3C.

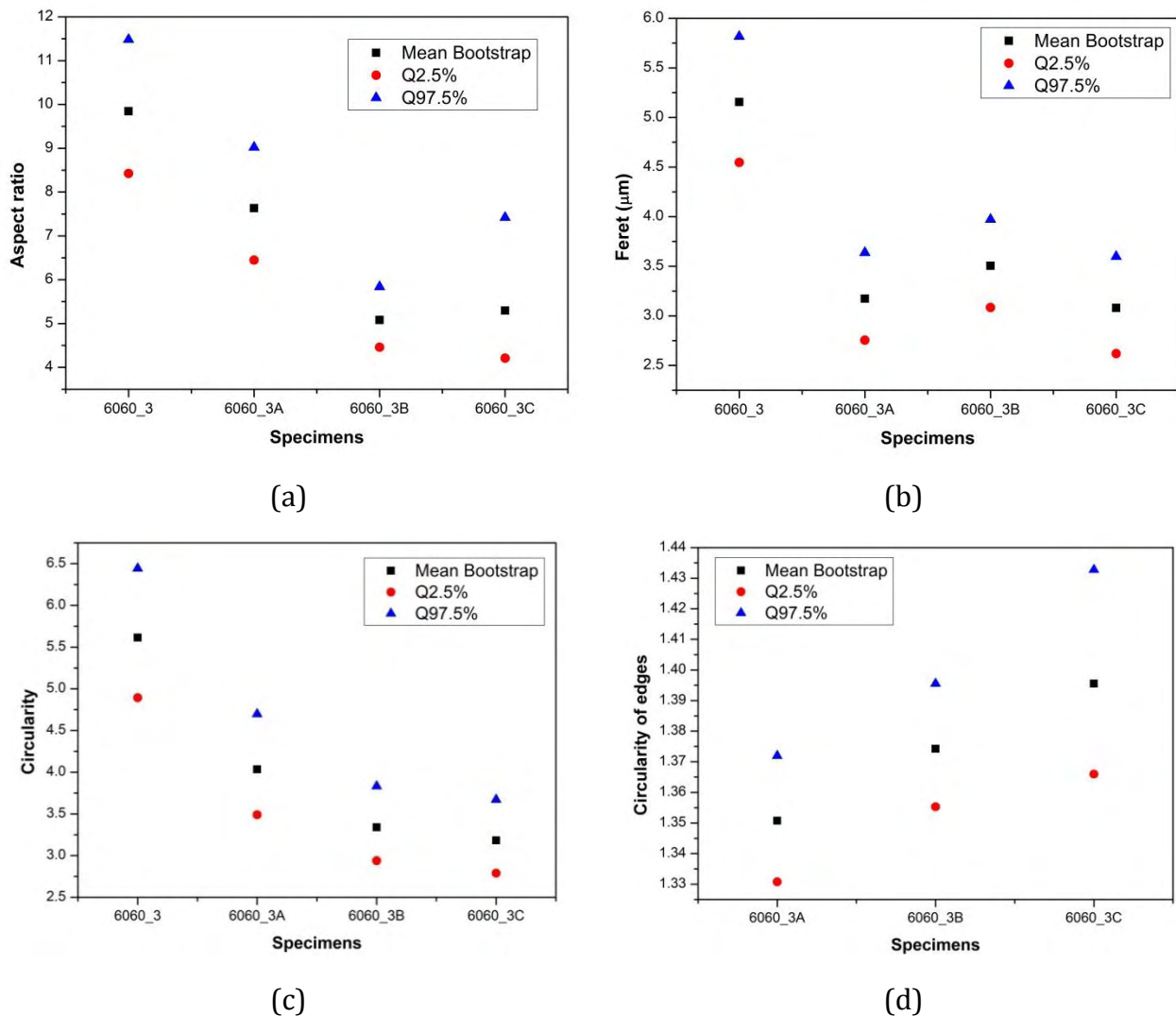


Figure 4.6: The values of indices for the as-cast and homogenized alloys: (a) aspect ratio, (b) feret, (c) circularity and (d) circularity of edges

## 4.6. Conclusions

An index-based method to quantify the homogenization state has been developed. Indices such as the aspect ratio, feret, circularity and circularity of edges have been determined in order to characterize the stage of spheroidization of the  $\alpha$ -AlFeSi phase, following the  $\beta$  to  $\alpha$ -AlFeSi transformation. The effect of the homogenization temperature was studied in a 6060 alloy. The major conclusions are the following:

- The  $\alpha$ -AlFeSi particles, after the completion of the  $\beta$  to  $\alpha$ -AlFeSi transformation undergo morphological changes leading to spheroidization. This process can be divided in three stages: (1) rounding of edges, (2) pinching and (3) neckless formation.
- The evolution of the morphological changes can be described quantitatively by the use of indices, which are sensitive to homogenization process parameters, such as the homogenization temperature or time.
- Through the use of these indices, it was found that the 580°C homogenization temperature leads to a complete spheroidization of the  $\alpha$ -AlFeSi phase, involving a neckless formation. The lower homogenization treatments resulted in intermediate stages involving rounding of edges or particle pinching.
- The method requires the measurement of a large number of particles and the implementation of a statistical analysis in order to be credible.

## 4.7. References

- [1] Sheppard, Kluwer Academic Publishers, (1999).
- [2] F.Y. Xie, T. Kraft, Y. Zuo, C.H. Moon, Y.A. Chang, *Acta Mater.*, 47 (1999) 489-500.
- [3] J.S. Robinson, *Mater. Sci. Technol.*, 19 (2003) 1697-1701.
- [4] L.L. Rokhlin, T.V. Dobatkina, N.R. Bochvar, E.V. Lysova, *J. Al., Compd.*, 367 (2004) 10-16.
- [5] A.R. Eivani, H. Ahmed, J. Zhou, J. Duszczek, *Met., Mat., Trans., A*, 40 (2009) 717-728.
- [6] A.R. Eivani, H. Ahmed, J. Zhou, J. Duszczek, *Met., Mat., Trans., A*, 40 (2009) 2435-2446.
- [7] A.R. Eivani, H. Ahmed, J. Zhou, J. Duszczek, *Cr and Mn*, *Mat., Sc., Tech.*, (2010)
- [8] J.D. Robson, P.B. Prangnell, *Acta Mater.*, 49 (2001) 599-613.
- [9] X. Fan, D. Jiang, Q. Meng, L. Zhong, *Mater. Lett.*, 60 (2006) 1475-1479.
- [10] ASTM Specification, F1877 (1998)
- [11] D. Wayne App. Nonpar. Stat. (2<sup>nd</sup> edition) (1990), 226-234
- [12] B. Efron Boca Raton, FL: Chapman & Hall/CRC (1993)

## 5. Precipitation during Cooling from the Homogenization Temperature

### 5.1. Introduction

An important step in the process chain of extrudable Al-alloys is the cooling from the homogenization temperature. As discussed in the previous chapters of this thesis, homogenization involves holding the material at a high temperature for a certain time period (holding time). During this time several transformations of the as-cast microstructure take place, including the dissolution of  $\text{Mg}_2\text{Si}$ , the transformation of  $\beta\text{-AlFeSi}$  to  $\alpha\text{-AlFeSi}$ , the spherodization of the  $\alpha\text{-AlFeSi}$  and the reduction of elemental microsegregation. During cooling from the homogenization temperature, new transformations are activated, the most important being the re-precipitation of  $\text{Mg}_2\text{Si}$ . The assumption is made here that although the  $\beta\text{-AlFeSi}$  is the thermodynamically stable phase at low temperatures, the transformation of  $\alpha\text{-AlFeSi}$  to  $\beta\text{-AlFeSi}$  does not take place at any appreciable rate. This is true, especially for the cooling rates encountered in the current industrial homogenization practices and is due to the very low diffusivity of Fe in the Al matrix. A DICTRA calculation in Chapter 3 indicated that there is actually no transformation of  $\alpha$  to  $\beta\text{-AlFeSi}$  during cooling of the cast billet. Therefore, the only transformation to be studied is the precipitation of the strengthening  $\text{Mg}_2\text{Si}$  phase. This chapter deals with three issues:

1. Precipitation of  $\text{Mg}_2\text{Si}$  and hardening of the homogenized billet
2. Hardening potential of homogenized billets
3. Effect of excess-Si on the Continuous Cooling Precipitation (CCP) diagrams

Regarding the first issue, a simulation is developed to describe precipitation of  $\text{Mg}_2\text{Si}$  during continuous cooling from the homogenization temperature. The KWN model, previously employed for isothermal aging of aluminum alloys [1], will be used in the present case, under non-isothermal conditions (continuous cooling). The results of the KWN model are the fraction and size of precipitates. A suitable strength model is then

employed to determine the strength (hardness) of the material at the end of the cooling period. A new Matlab code has been developed [2] to handle the calculations under both isothermal and non-isothermal conditions encountered in welding and the modification to the non-isothermal conditions prevailing during cooling from the homogenization temperature has been performed [3] at LoM. The results of the combined KWN and strength models are experimentally validated.

Regarding the second issue, the hardening potential of the homogenized billets is investigated experimentally for three alloys 6063, 6005 and 6082 as a function of homogenization temperature and cooling rate. The aim here is to identify possible effects of homogenization parameters on the ability of the material to age harden (hardening potential) during subsequent aging treatments.

The third issue is related to the extrudability of the homogenized billet. It is of major concern to the development of high extrudability. After homogenization the billets are transferred to the extrusion press. Before extrusion, a preheating of the billets is performed. The selection of the preheating temperature is crucial, since during extrusion the temperature of the material rises due to the high deformation rate. Furthermore the exit temperature from the extrusion press should not exceed a certain limit (e.g the solidus) in order to avoid hot tearing resulting from local melting of low-melting temperature eutectics. For high extrudability (high extrusion speeds) the preheating temperature should be as low as possible. The equilibrium  $\beta$ -Mg<sub>2</sub>Si phase has a high solvus temperature and will not dissolve during preheating. Therefore the cooling from the homogenization temperature should aim at the precipitation of the metastable  $\beta'$ -Mg<sub>2</sub>Si, which exhibited a lower solvus. The precipitation of this metastable phase is influenced by the presence of the so-called excess Si in the alloy. The KWN model was employed in order to quantify the effect of excess Si on the precipitation of the metastable  $\beta'$ -Mg<sub>2</sub>Si, in an effort to quantify the effect of new alloy compositions on the CCP diagram. The approach was applied for the 6060 alloy.

Taking into account the three issues stated above as well as the results presented in the previous chapters of this thesis, design rules are formulated for the achievement of high extrudability.

## **5.2. Precipitation and hardening during cooling from the homogenization state**

### **5.2.1. Simulations with the KWN and Strength models**

The majority of phase transformations, which take place in alloys, are diffusional and proceed by thermally activated movements of atoms across a concentration gradient. Of significant importance in relation to thermal industrial processing, are phase transformations involving precipitation reactions resulting to a second phase in the form of a particle population. During these transformations three basic physical mechanisms are taking place, the nucleation of new particles the growth of the nucleated particles and the coarsening of the particles resulting to a particle population which can be described by a particle size distribution (PSD). The material final mechanical properties depend on the particles volume fraction and radius and consequently on the shape of the PSD. Since the original works of Lifshitz & Slyozov [4] and Wagner [5] only a few of the published precipitation models are comprehensive to deal with non-isothermal transformations treating nucleation, growth and coarsening taking place concurrently. The two main works in this area were performed by Langer & Schwartz [6] who studied nucleation and growth of droplets in near-critical fluids and Kampmann et al. [7,8] who proposed a numerical procedure (KWN model) for the calculation of the particle size distribution in solid-state transformations treating the concurrent nucleation, growth and coarsening of precipitates. As mentioned above the KWN model was modified to handle precipitation of  $\text{Mg}_2\text{Si}$  during cooling from the homogenization temperature. The results of the model were introduced to the strength model for the calculation of the final strength of the cooled billet, after homogenization. The strengthening mechanisms considered were lattice resistance, solid solution strengthening and precipitation strengthening. The details of the models are discussed in [1-3]. Results will be presented for alloy 6063, where the experimental validation was performed.

Three homogenization temperatures were considered 540, 560 and 580°C. Homogenization time is not a parameter in these simulations, since it is considered that the time is enough for complete dissolution of the  $\text{Mg}_2\text{Si}$  phase during holding at the homogenization temperature. Therefore all Mg and Si are in solid solution at the end of the homogenization holding period. A critical parameter is the cooling rate. Two cooling

profiles were considered, since it was possible to accomplish only natural cooling and forced cooling (with forced air circulation) in a laboratory scale. The cooling profiles are shown in Figure 5.1 a, b. With natural cooling, cooling at 100°C is accomplished in 700 sec, while with forced cooling the same temperature is reached in only 220 sec. In addition the difference in homogenization temperature is evident only at the initial stages of cooling, and then the three curves coincide.

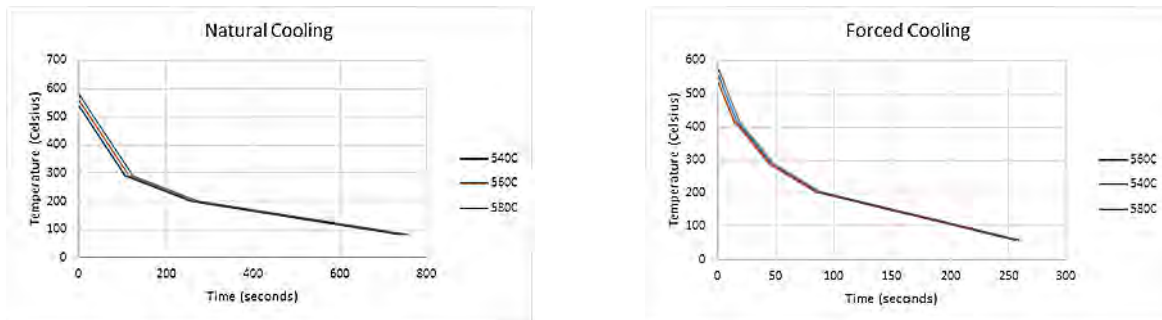


Figure 5.1: Measured cooling profiles used in simulations and in the experimental validation, (a) natural cooling, (b) forced cooling

The simulation results from the KWN model regarding the evolution of the volume fraction and particle size of the  $Mg_2Si$  phase as a function of time during cooling from the homogenization temperature are shown in Figure 5.2. Regarding the volume fraction, it appears that the homogenization temperature influences the initial stages of the precipitation. Towards the end of cooling the curves corresponding to the three homogenization temperatures coincide. The amount of  $Mg_2Si$  formed under forced cooling is slightly lower than the respective amount formed under natural cooling conditions, 0.79 and 0.82% respectively. However the final particle size at the end of cooling is lower in the forced cooling condition, about 6.9nm, compared to 7.8nm for the natural cooling condition.

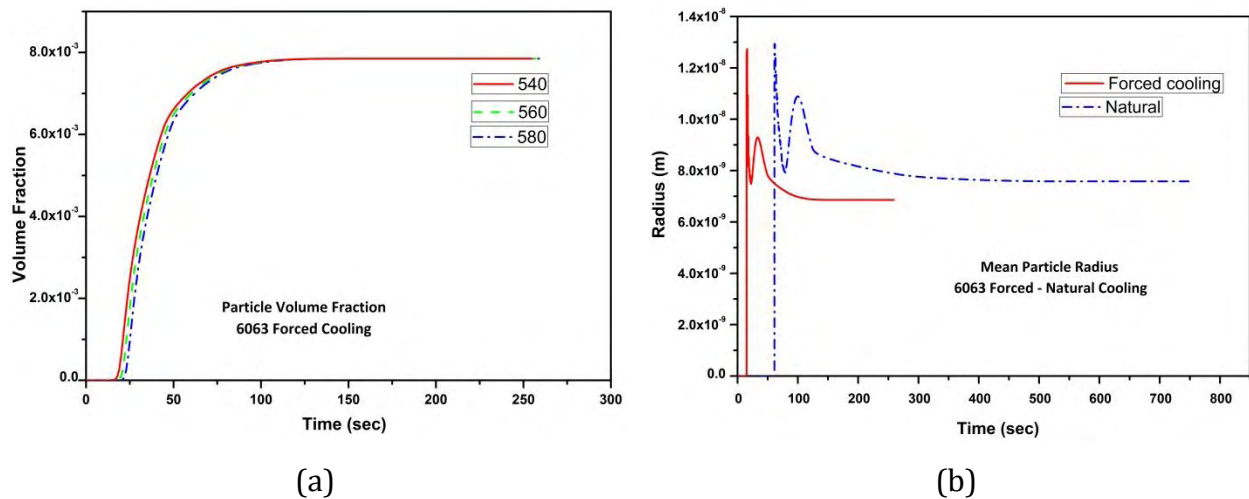


Figure 5.2: Simulation results for the 6063 alloy: (a) evolution of  $\text{Mg}_2\text{Si}$  volume fraction during cooling for three homogenization temperatures 540, 560 and 580°C and (b) evolution of particle size during cooling for natural and forced cooling from 580°C homogenization temperature

Regarding the shape of the curves describing the size evolution during cooling, is evident from Figure 5.2b that there is a competition between nucleation and growth processes, which as mentioned in the Introduction of this chapter, take place simultaneously. Three stages can be described. Following initial nucleation the mean size drops due to the increase of the nucleation driving force with the decrease in temperature. The rise of the mean size is followed by growth of the already nucleated particles. However the further decrease of temperature during cooling induces a substantially higher driving force for nucleation and the mean size is again reduced to its final value at the end of cooling.

The respective particle size distributions (PSD) are given in Figure 5.3 for the 580°C homogenization temperature and the two cooling profiles. The KWN simulation predicts similar peak sizes for the two cooling profiles, but it also predicts a second peak and larger particles for the natural cooling profile. This is due to the longer time available for the precipitation process in the case of natural cooling.

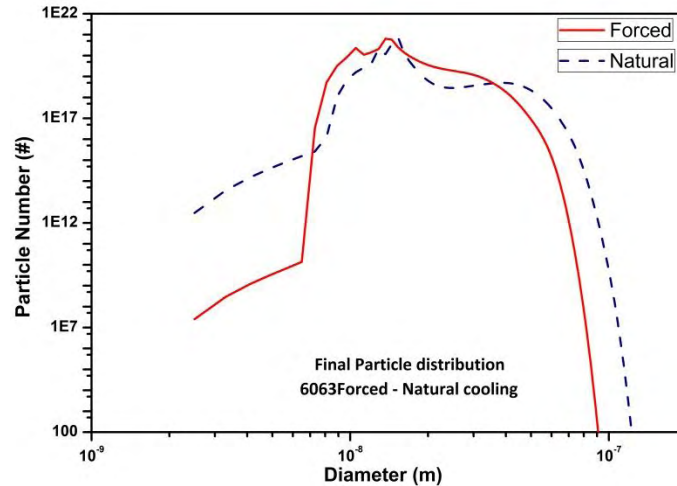


Figure 5.3: Particle size distribution (PSD) predicted by the KWN model for the 6063 alloy for the two cooling profiles, natural and forced cooling for the 580°C homogenization temperature

The volume fraction of  $\text{Mg}_2\text{Si}$  and the size evolution are used as input to the strength model. The resulting hardness evolution is shown in Figure 5.4 for the two cooling profiles and the three homogenization temperatures. The results indicate that forced cooling results in slightly higher hardness 69 relative to 64.9  $\text{HV}_{0.3}$  for natural cooling. This hardness difference is attributed to the slightly finer dispersion of  $\text{Mg}_2\text{Si}$  formed after forced cooling.

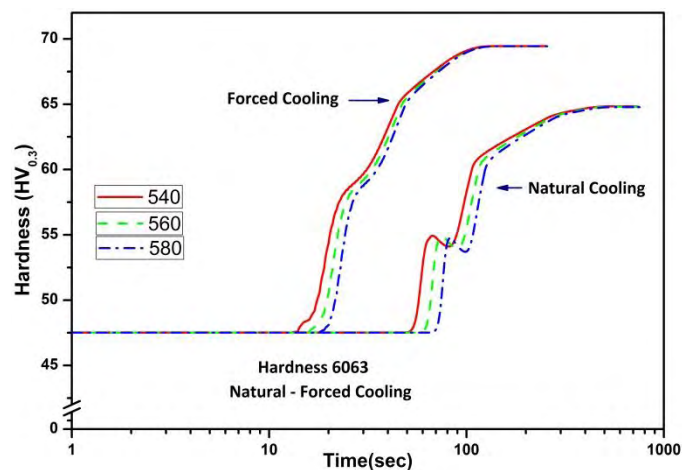


Figure 5.4: Evolution of hardness during cooling of the 6063 alloy for natural and forced cooling and for three homogenization temperatures 540, 560 and 580°C.



### 5.2.2. Experimental validation

In order to validate the simulation predictions presented above, homogenization experiments were performed in as-cast alloy 6063. Homogenization was performed in a laboratory furnace at temperatures 540, 560 and 580°C for 8 hours. According to the results presented in Chapter 3, this time is more than sufficient in order to dissolve all  $Mg_2Si$  present in the as cast microstructure. Two cooling methods were followed, natural and forced air cooling, following the profiles depicted in Figure 5.1. The specimens were then polished to a flat surface and microhardness measurements were taken with a Vickers indenter and a load of 0.3 Kg. The hardness measurements appear in Table 5.1.

Table 5.1: Microhardness ( $HV_{0.3}$ ) as a function of cooling profile

| <b>Homogenization temperature (°C)</b> | <b>Forced Cooling</b>        | <b>Natural Cooling</b>       |
|--|------------------------------|------------------------------|
| 540                                    | 60.1, 59.2, 63.6, 64.1, 63.9 | 61.7, 61.8, 61.0, 61.2, 61.6 |
| 560                                    | 63.0, 63.8, 67.4, 64.3, 63.7 | 62.3, 60.0, 58.6, 61, 61.8   |
| 580                                    | 66.3, 66.4, 70.0, 65, 63.2.  | 64, 62.8, 61.0, 61.6, 61.2   |
| <b>Mean hardness</b>                   | 64.1                         | 61.4                         |

The hardness resulting from forced cooling is slightly higher than the one resulting from natural cooling as predicted by the simulation. Regarding absolute values, the simulation overestimates the hardness by 3-4 Vickers units in both cases, as shown in Figure 5.4. Taking into account the approximations used in the KWN precipitation model as well as the strength model, the agreement is considered satisfactory.

## 5.3. Hardening potential of homogenized billets

### 5.3.1. Introduction

An experimental study has been undertaken to identify the effect of homogenization temperature and time on the hardening potential of the alloys during subsequent aging. It is realized that a significant amount of  $Mg_2Si$  is precipitated during cooling from the

homogenization temperature and, depending on the cooling rate, an amount of Mg and Si still remains into solution. Under conditions of natural aging, the hardness of the material could be further increased due to precipitation. Such conditions are encountered in industrial practice in the time between billet homogenization and billet extrusion. These two operations are usually performed in different industrial sites and, therefore, several days could elapse between these two operations, during which natural aging is at play. Referring to the hardening potential, it is defined as the hardness increase between the homogenized state and the state after natural aging. The effect of homogenization temperature, homogenization time, cooling rate and alloy composition on the hardening potential was investigated experimentally [9]. The experimental procedures and the results of this study are presented in the next sections.

### **5.3.2. Experimental procedures**

Three alloys were investigated, 6082, 6005 and 6063, the chemical composition of which is given in Table 2.2. The billets were sectioned and specimens were prepared and homogenized according to the procedures described in Chapter 3. Three homogenization temperatures 540, 560 and 580°C as well as four homogenization times 0.5, 4, 8 and 32 hours were selected. Similar homogenization parameters have been studied by other researchers [10-13]. Three conditions regarding the cooling rate were studied: Water Quenching (Q), air cooling (AC) and forced cooling (FC). A K-type thermocouple was attached at the specimens in order to monitor the cooling profile. The cooling profiles are depicted in Figure 5.5. The AC and FC specimens reach 150°C in 6 and 2.5 min respectively.

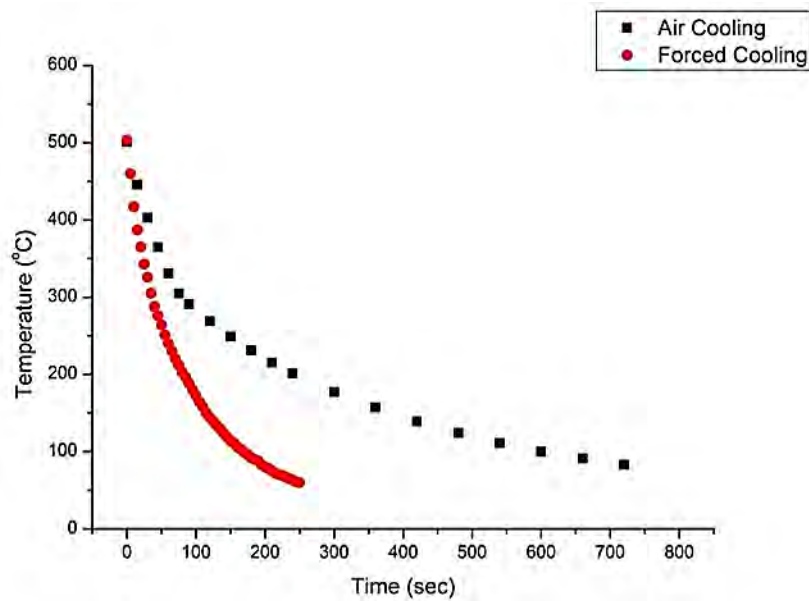


Figure 5.5: Homogenization cooling profiles

Brinell hardness testing was performed in all specimens with a 5mm ball indenter diameter and a load of 250Kg for 15 sec. The indentation diameter was measured by microscopy. In order to determine the hardening potential, the hardness measurements were performed immediately after cooling and also after 5 days of natural aging at room temperature. The 5 day period has been also suggested in [12,14].

### 5.3.3. Results

Brinell hardness is depicted as a function of homogenization temperature and cooling rate in Fig. 6, 7 and 8 for alloys 6082, 6005 and 6063 respectively. Regarding the data for the 6082 alloy in Figure 5.6, it appears that for the short homogenization times (0.5 and 4 hours) the quenched specimens possess higher hardness followed by the forced cooled and air cooled specimens. This is due to the higher amount of Mg and Si into solution (solution strengthening).

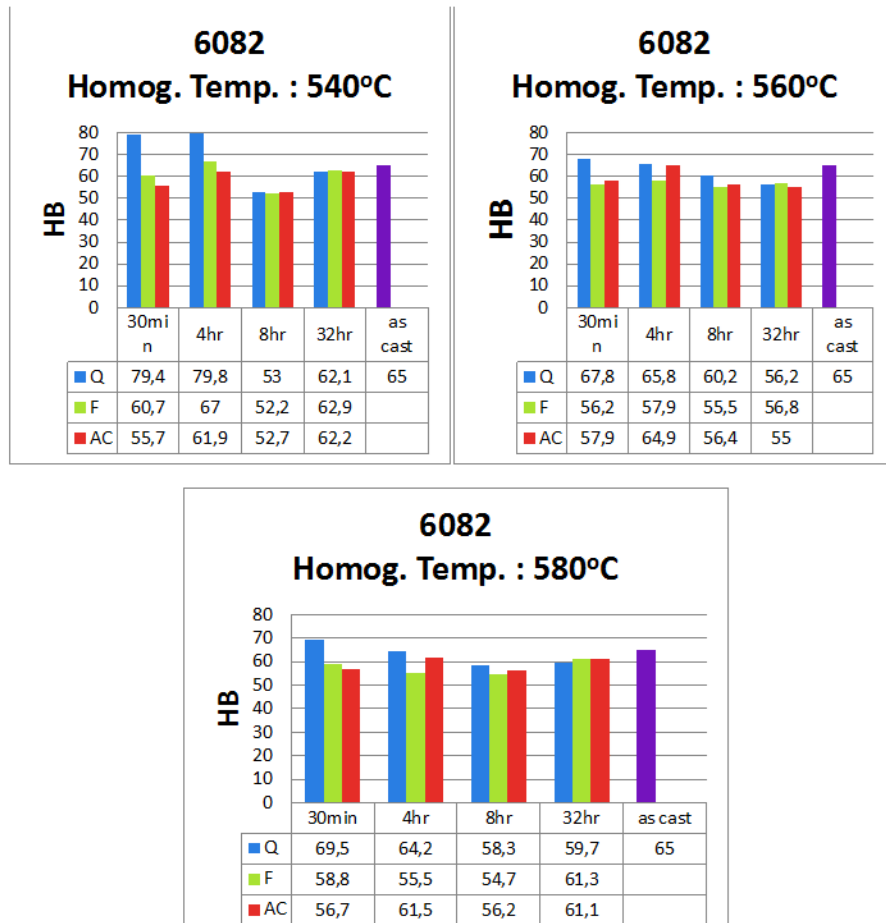


Figure 5.6: Brinell hardness of alloy 6082 immediately after cooling from the homogenization temperature

This hardness difference increases with alloying (6063→6005→6082). At longer homogenization times the difference between the three cooling conditions diminished. Similar situations can be described for the other two alloys as depicted in Figures 5.7 and 5.8 for 6005 and 6063 alloys respectively.

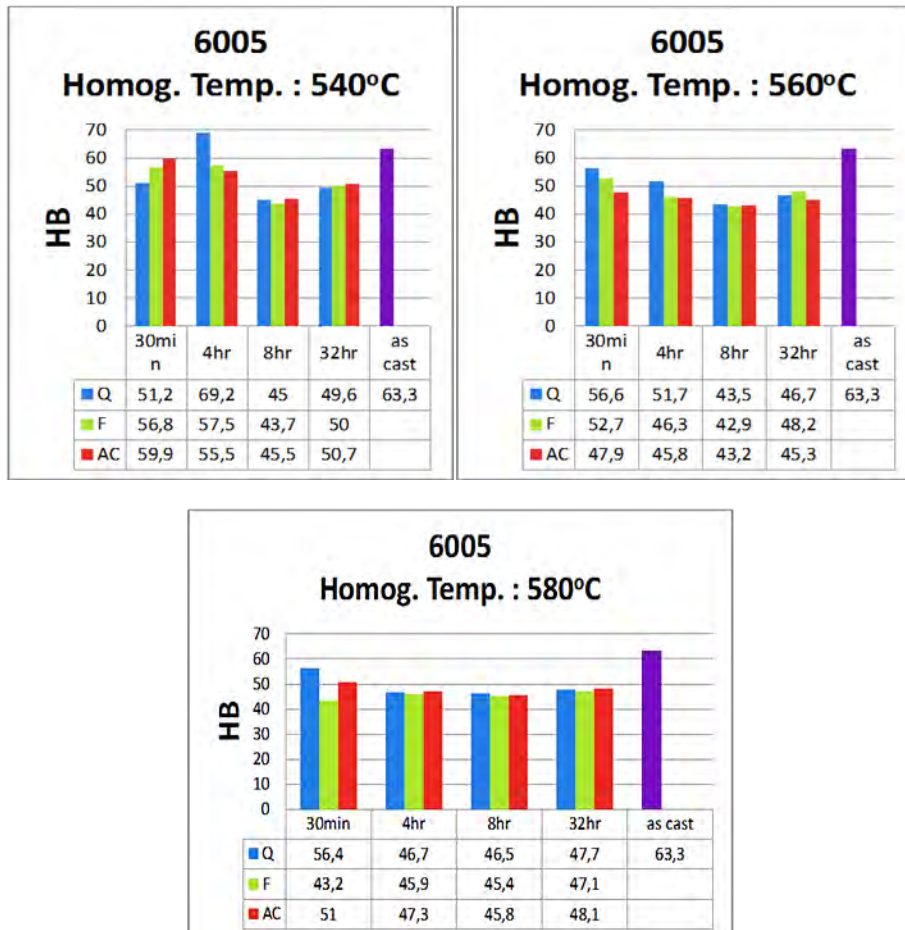


Figure 5.7: Brinell hardness of alloy 6005 immediately after cooling from the homogenization temperature

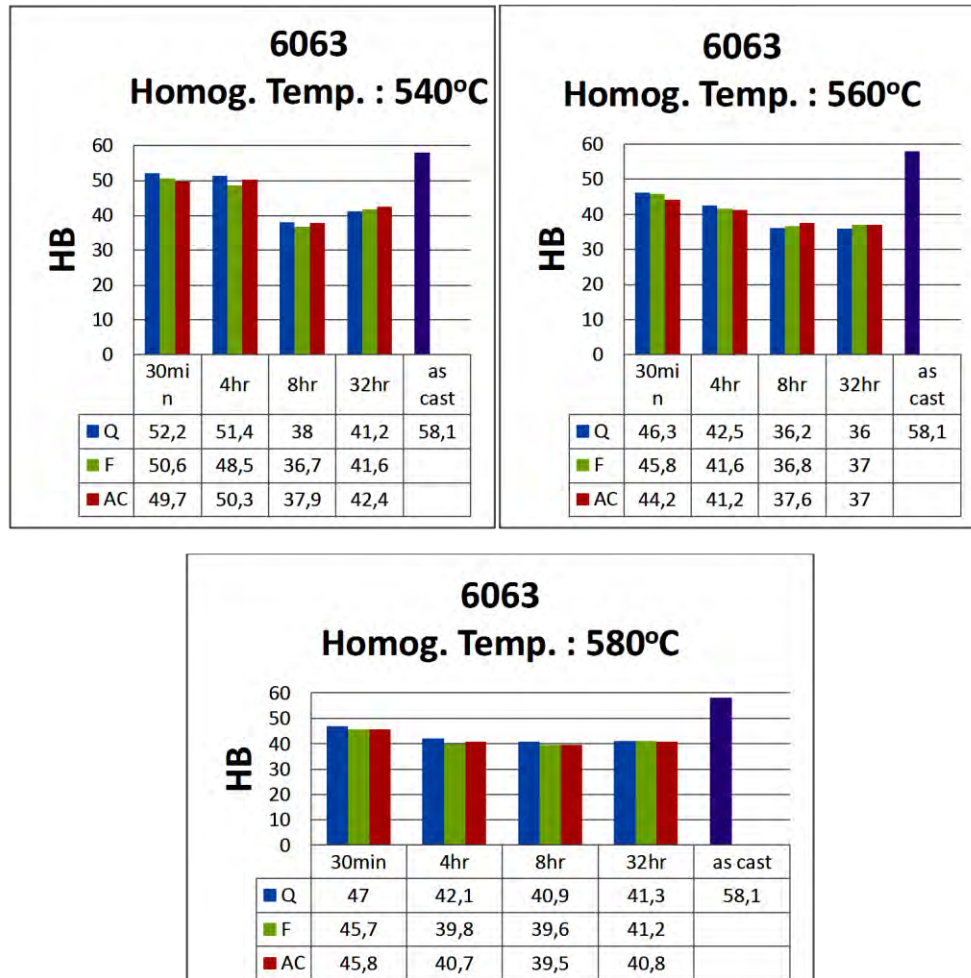


Figure 5.8: Brinell hardness of alloy 6063 immediately after cooling from the homogenization temperature

In all three alloys, the 8h homogenization treatment appears softer in almost all homogenization temperatures and cooling rates. Moreover with increasing the Mg and Si alloying elements the hardness increases for each specific cooling rate. This effect can be seen more easily in Figures 5.9, 5.10 and 5.11, which depict the comparison between the three alloys for a 4h homogenization time and for the 540, 560 and 580°C homogenization temperature respectively.

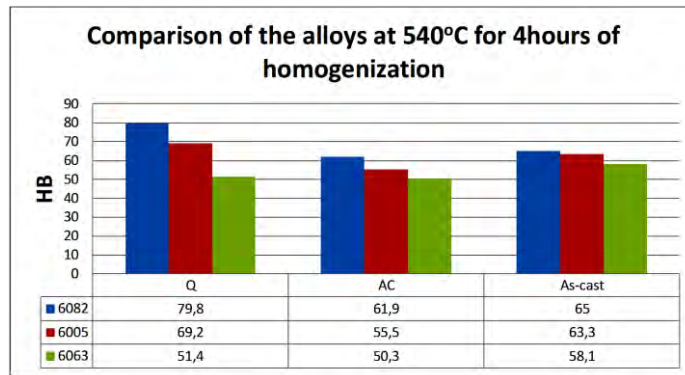


Figure 5.9 Brinell hardness immediately after cooling from 540°C homogenization temperature

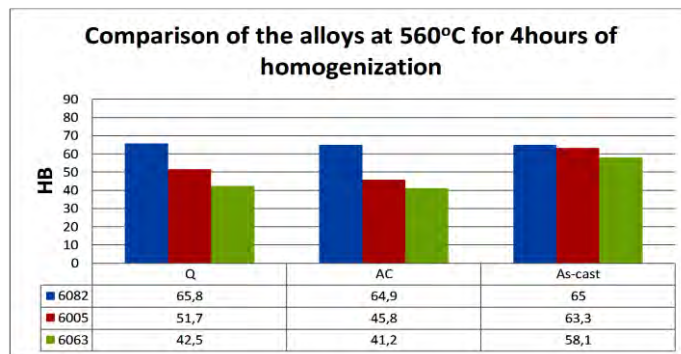


Fig. 4.17 Comparison of the 6082, 6005 and 6063 alloys at 560°C for 4hours of homogenization

Figure 5.10: Brinell hardness immediately after cooling from 560°C homogenization temperature

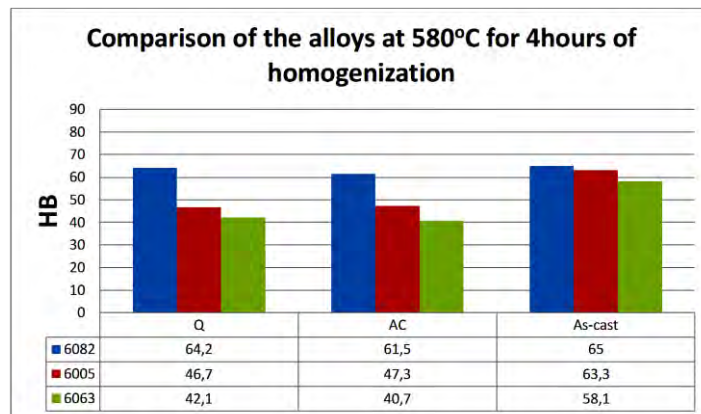


Fig. 4.18 Comparison of the 6082, 6005 and 6063 alloys at 580°C for 4hours of homogenization

Figure 5.11: Brinell hardness immediately after cooling from 580°C homogenization temperature

In all cases the homogenized alloys exhibited higher hardness differences between them in the homogenized state in relation to the as-cast state. The quenched specimens exhibit higher hardness relative to the air-cooled state only for the 540°C homogenization temperature. These differences diminish at higher homogenization temperatures.

As mentioned above, the hardening potential of the homogenized billets was investigated. The hardness of the homogenized billets after 5 days of natural aging is depicted in Figures 5.12, 5.13 and 5.14 for the 6082, 6005 and 6063 alloys respectively.



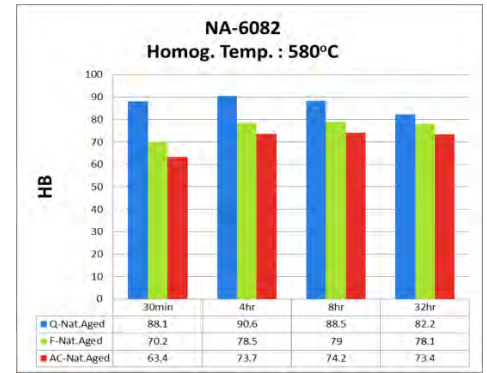
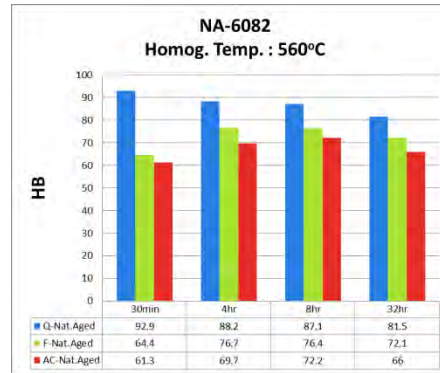
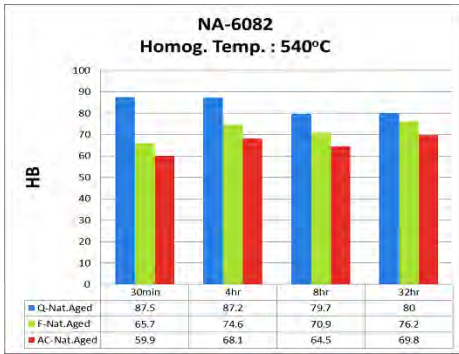


Figure 5.12: Brinell hardness after homogenization and natural aging for the 6082 alloy

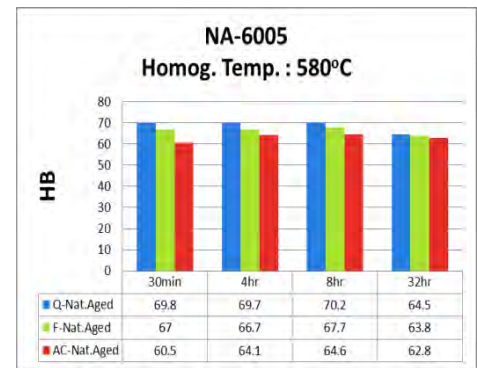
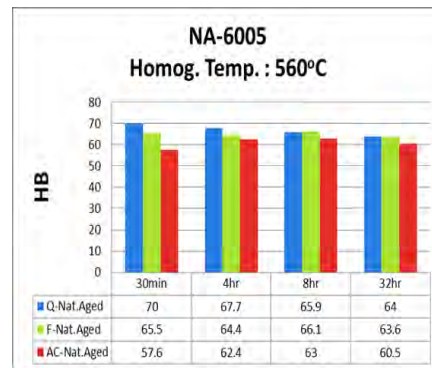
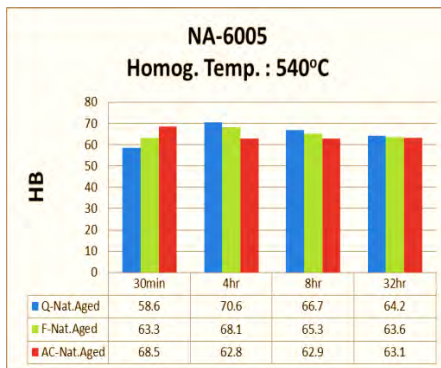


Figure 5.13: Brinell hardness after homogenization and natural aging for the 6005 alloy

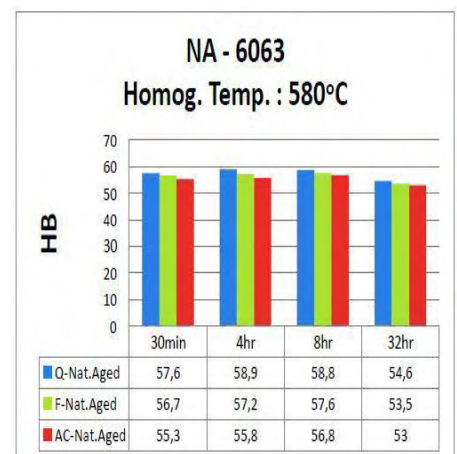
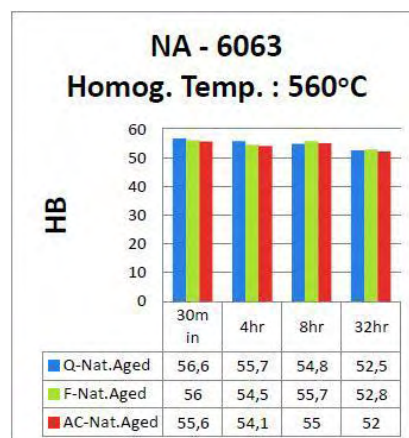
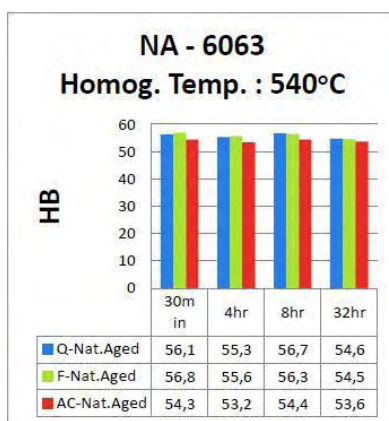


Figure 5.14: Brinell hardness after homogenization and natural aging for the 6063 alloy

It is evident that the quenching state (Q) exhibits higher hardening relative to the air cooling (AC) and forced cooling (FC) states. In addition, the 8 h homogenization time, after natural aging, does not correspond any more to the softer state. These effects can be better examined directly by plotting the hardening potential of the alloys. The hardening potential  $H_p$  can be expressed as

$$H_p = \frac{H_{NA} - H_{AH}}{H_{AH}} \times 100$$

where,  $H_{AA}$  is the hardness after 5 days of natural aging and  $H_{AH}$  is the hardness immediately after homogenization. The results are shown in Figures 5.15, 5.16 and 5.17 for the 6082, 6005 and 6063 alloys.

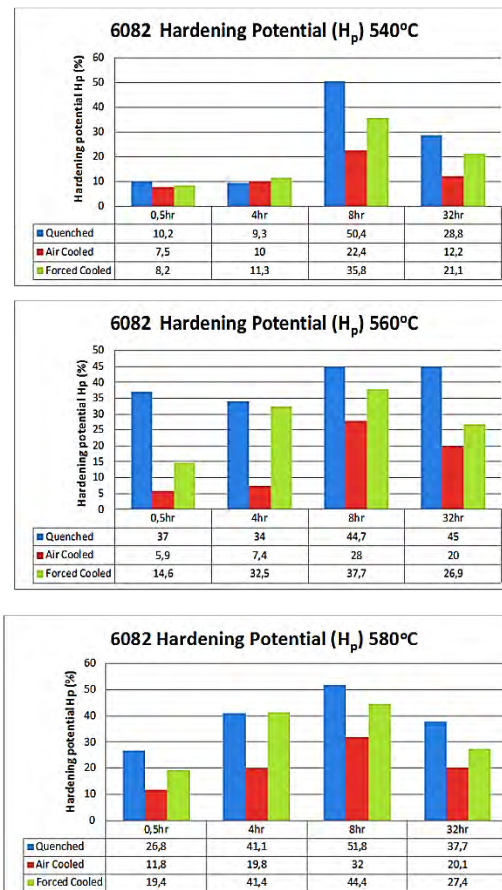


Figure 5.15: Hardening potential  $H_p$  for the 6082 alloy at (a) 540, (b) 560 and (c) 580°C homogenization temperatures

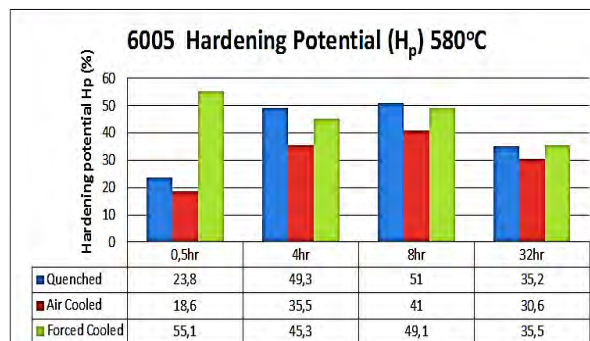
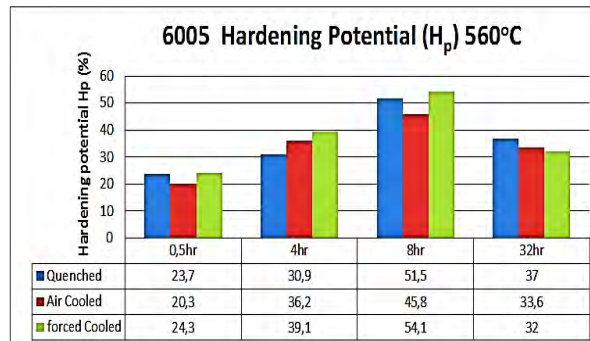
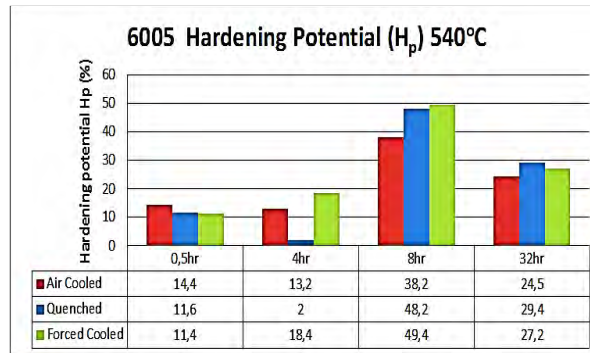


Figure 5.16: Hardening potential  $H_p$  for the 6005 alloy at (a) 540, (b) 560 and (c) 580°C homogenization temperatures

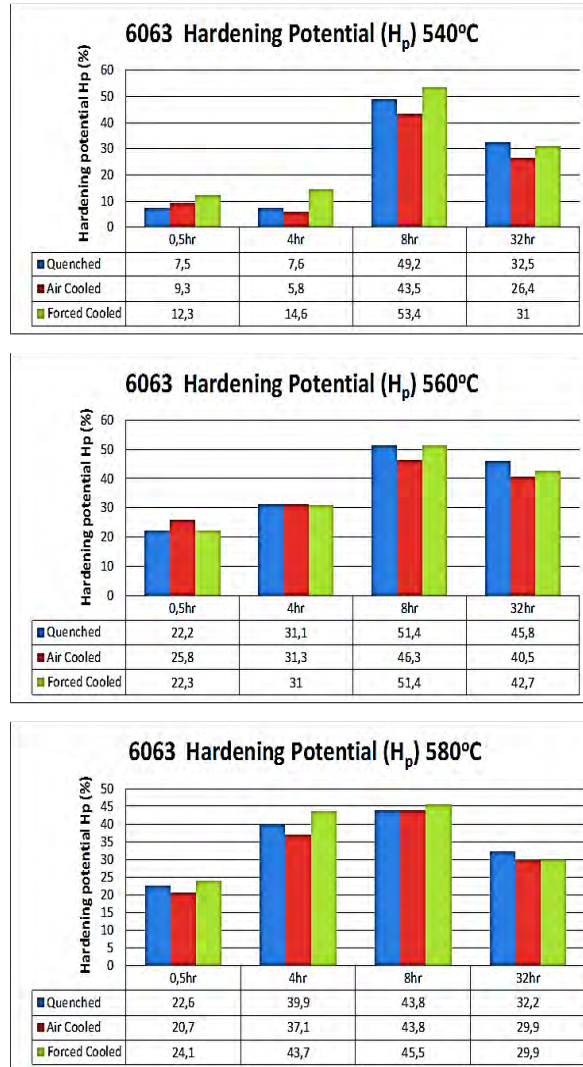


Figure 5.17: Hardening potential  $H_p$  for the 6063 alloy at (a) 540, (b) 560 and (c) 580°C homogenization temperatures.

For the 6082 alloy, the Q state exhibits the highest hardening potential followed by the FC and AC states, this is due to the higher amount of Mg and Si retained in solid solution after quenching from the homogenization temperature. The same effect is observed for the 6005 and 6063 alloys. Regarding the effect of homogenization time, the hardening potential for the Q, FC and AC states increases with homogenization time, reaches a maximum at 8h and then decreases. This is in line with the results presented above, indicating that the softer state following homogenization is the one corresponding to the 8 h homogenization time. It appears from these results that transformations other than the  $Mg_2Si$  dissolution during homogenization influence the Mg and Si in the matrix. The most probable influence is from the  $\beta-AlFeSi \rightarrow \alpha-AlFeSi$  transformation, studied in Chapter 3, which liberates Si in

the Al matrix. This Si is combined with the Mg coming from the dissolution of eutectic constituents and forms additional  $\text{Mg}_2\text{Si}$ . For the 6005 alloy, the maximum hardening potential also appears for the 8h homogenization time. However the difference between the 8h treatment and the other homogenization times diminishes with the homogenization temperature. The same arguments hold for the 6063 alloy. Additionally in this case the hardening potential at 0.5 and 4h homogenization times, increase with the homogenization temperature. At 580°C homogenization temperature, the hardening potential of the 4 and 8h are practically the same. Finally for the lower alloyed 6063 and 6005 billets, the hardening potential at shorter homogenization times (0.5 and 4h) increase with the homogenization temperature.

The above results illustrate the complex interactions between alloying elements, homogenization temperature, time and cooling rate on the strengthening mechanisms at play and especially on solid solution and precipitation strengthening. More work is required in this area, possibly involving a more rigorous approach, e.g an extended KWN model in multicomponent systems, to quantify the observed behavior.

## **5.4. Effect of excess-Si on the CCP diagram**

### **5.4.1. Introduction**

Extrudability depends on the state of iron intermetallics and removal of microsegregation during homogenization. However, extrudability also depends on the strength of the billet prior to extrusion, i.e. the state of  $\text{Mg}_2\text{Si}$  precipitation.  $\text{Mg}_2\text{Si}$  precipitation takes place during cooling from the homogenization temperature and also during billet preheating. These  $\text{Mg}_2\text{Si}$  precipitates should dissolve completely during extrusion in order to develop a good response to the aging treatment. The rate of cooling is important. It appears that a cooling cycle that produces a fine dispersion of  $\beta\text{-Mg}_2\text{Si}$  is the optimum for extrudability [15,16]. The reasons are: (a) finer particle dispersion, which dissolves faster, (b) a lower dissolution temperatures because it possesses a lower solvus temperature. Therefore during preheating, the  $\beta'$  will dissolve at a lower temperature, be substituted by a fine dispersion of  $\beta\text{-Mg}_2\text{Si}$ , which will dissolve readily during extrusion. This enables the use of a lower preheating temperature, providing a larger window for



temperature rise up to the exit temperature. This means that a higher extrusion speed can be applied. Precipitation of  $\beta$  takes place below 400°C. A CCP diagram for 6060 alloys can be used to design the relevant cooling cycle. As far as alloying is concerned, it appears that the amount of the so-called excess Si ( $Si_{ex}$ ) is important as it affects the precipitation kinetics in Al-Mg-Si alloys.  $Si_{ex}$  leads to finer and denser precipitates by enhancing the nucleation kinetics of GP zones. It has been reported [17] that the excess Si in the alloy enhances the nucleation of the hexagonal  $\beta$ -  $Mg_2Si$  on Si atom grids, which are composed of hexagonal sub cells with lattice parameters  $a=b=4.05\text{\AA}$  and  $c=4.05\text{\AA}$  (Angstroms). For a given Mg and Fe content, the amount of  $Si_{ex}$  depends on which intermetallic ( $\alpha$ -AlFeSi or  $\beta$ -AlFeSi) is present. During homogenization, the transformation  $\beta \rightarrow \alpha$  leads to an increase of  $Si_{ex}$  since the  $\beta$ -AlFeSi contains more Si than the  $\alpha$ -AlFeSi phase. The aim of this section is to determine the shift of the Continuous Cooling Precipitation diagram due to the amount of the excess Si in the alloy. The methodology was applied for the 6060\_3 alloy. The chemical composition of the alloy was given in Table 2.2 in Chapter 2.

### 5.4.2. Methodology

Construction of CCP diagrams can be accomplished experimentally by applying Differential Scanning Calorimetry (DSC). A sample is cooled continuously from the homogenization temperature and the endothermic or exothermic peaks arising from particle dissolution or precipitation are recorded. Such a DSC spectrum is given in Figure 5.18 taken from [18], for a 6005 alloy for several cooling rates.

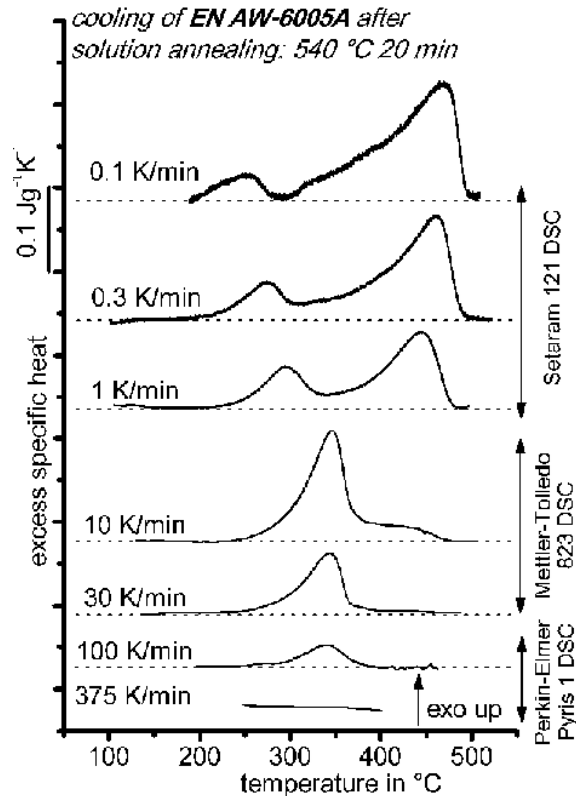


Figure 5.18: DSC spectra for 6005 alloy (0.57Mg-0.68Si) for cooling rates from 0.1 to 375 K/min [18]

The first peak during cooling is attributed to  $\beta$ -Mg<sub>2</sub>Si, while the second peak at lower temperatures is attributed to  $\beta'$ -Mg<sub>2</sub>Si precipitation. It is clear that the application of a higher cooling rate suppresses the precipitation of the  $\beta$ -Mg<sub>2</sub>Si, leaving only the precipitation of the  $\beta'$ -Mg<sub>2</sub>Si. Literature studies regarding the effect of cooling rate on the precipitation of Mg<sub>2</sub>Si are limited. Only one publication regarding the development of Continuous Cooling Precipitation (CCP) diagram was found [18] and one publication regarding the isothermal TTP diagram of 6082 [19]. The work presented in this section is based on the work presented in [18] where the CCP diagrams for five alloys 6060, 6063, 6005, 6082(L) and 6082(H) were determined. The composition of the 6060 alloy studied in the above work is 0.43 Mg-0.40Si. The aim is to quantify the shift of the CCP with the new alloy composition of 6060\_3. It is evident from the above work that the position of CCP is influenced by mainly the Mg content and secondly by the excess Si in the alloy. Mg influences directly the amount of Mg<sub>2</sub>Si while the excess Si influences the heterogeneous nucleation sites of the  $\beta'$ -Mg<sub>2</sub>Si. The methodology followed is the following:

- Non linear fitting of the  $\beta$ -nose and the  $\beta'$ -nose of the CCP with the Mg content using the data of the CCPs from the work [18].
- Use of the equations derived in step (a) to calculate the nose position for a model alloy.
- Displacement of the  $\beta$  and  $\beta'$  noses due to the excess Si in the alloy. Final position of the CCP curve of the 6060\_3 alloy.

### 5.4.3. Results

The CCP diagrams for the alloys investigated in [18] are depicted in Figure 5.19.

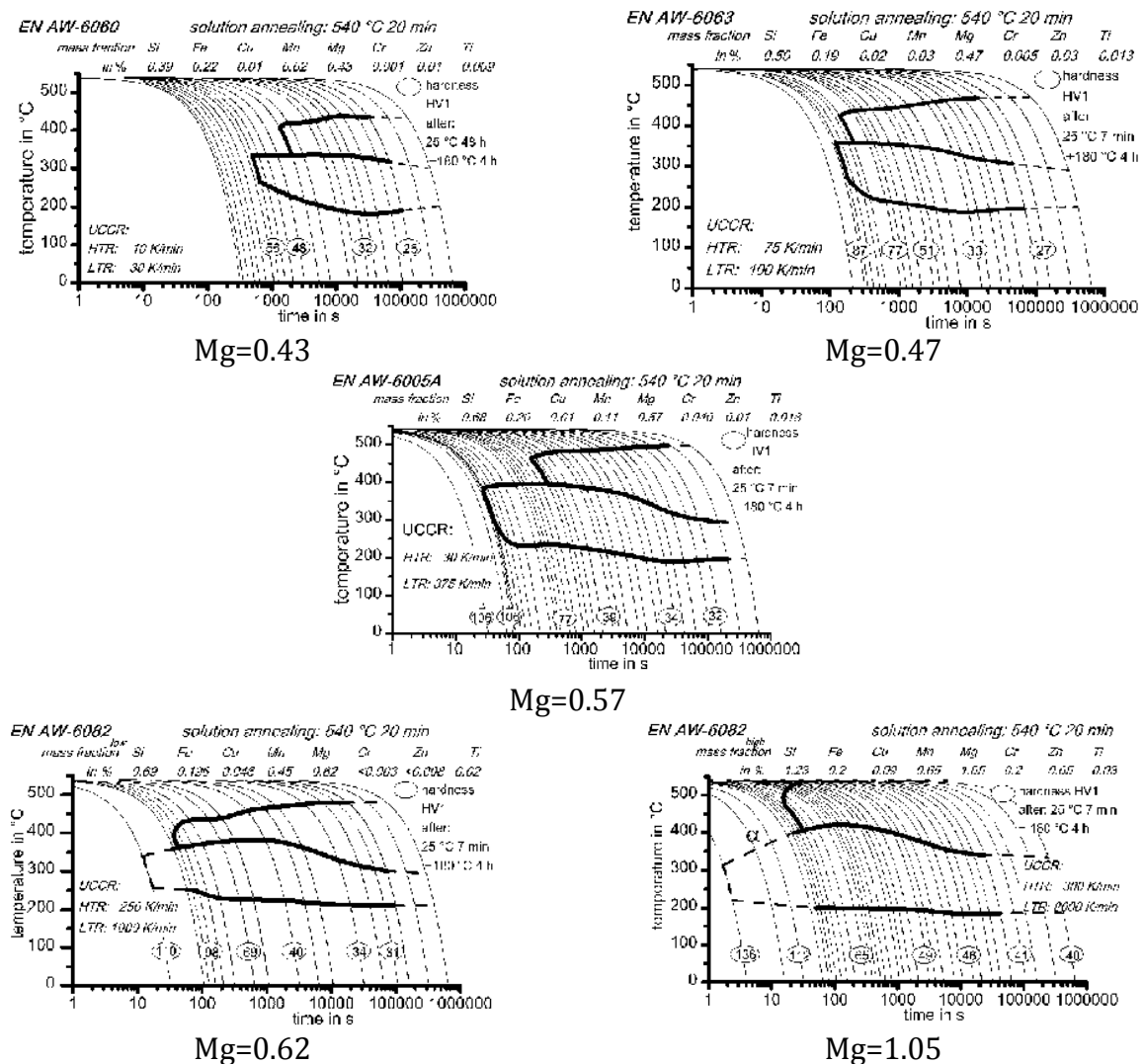


Figure 5.19: CCP diagram for 6060, 6063, 6005 and 6082 alloys [18]



The times for the  $\beta$  and  $\beta'$  noses of the CCP diagrams are given in Table 5.2 as a function of Mg content

| Table 5.2 Position of $\beta$ and $\beta'$ noses from the CCP diagrams of Fig.2 |                                |                                 |                          |                           |
|---|--------------------------------|---------------------------------|--------------------------|---------------------------|
| Mg(wt%)   | Time (sec)<br>( $\beta$ -nose) | Time (sec)<br>( $\beta'$ -nose) | Logt<br>( $\beta$ -nose) | Logt<br>( $\beta'$ -nose) |
| 0.43  | 1200                           | 450                             | 3.07                     | 2.65                      |
| 0.47  | 180                            | 100                             | 2.25                     | 2.00                      |
| 0.57  | 170                            | 25                              | 2.23                     | 1.39                      |
| 0.61  | 40                             | 10                              | 1.60                     | 1.00                      |
| 1.05  | 15                             | 1.8                             | 1.17                     | 0.255                     |

Nonlinear curve fitting has applied to the data of Table 5.3 in order to get an expression for the position of the noses as a function of Mg content. An Arrhenius expression was selected for the fitting. The fitting results are displayed in Figure 5.20

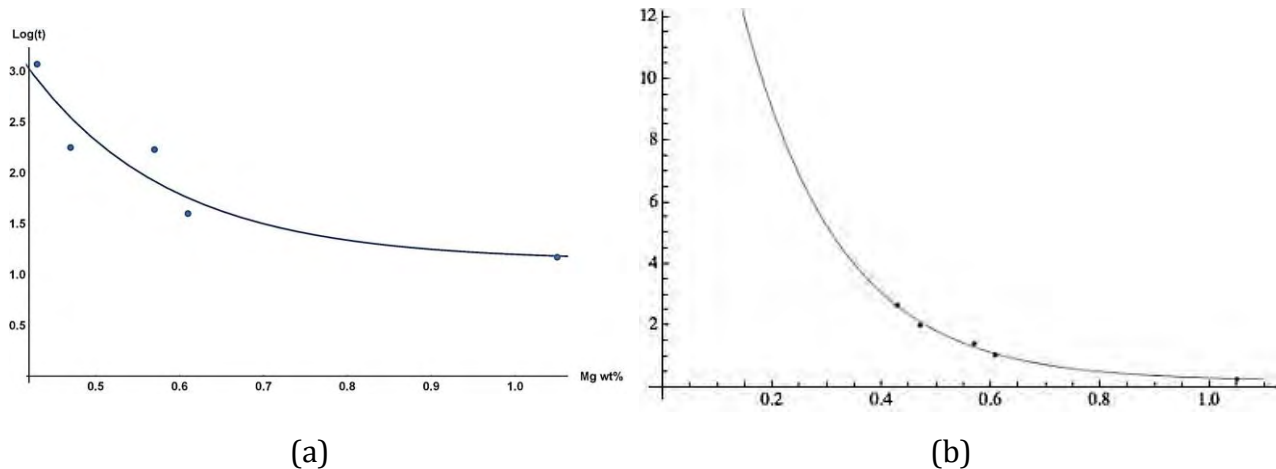


Figure 5.20: Arrhenius fitting of the data of Table 2 a) Fitting the  $\beta$ -nose, b) fitting  $\beta'$  - nose

The expression for the  $\beta$ -nose is

$$\log t = 1.13665 + 22.4678e^{-5.89242 \text{ Mg}} \quad (1)$$

The expression for the  $\beta'$ -nose is

$$\log t = 0.186353 + 27.3091e^{-5.64495 \text{ Mg}} \quad (2)$$

For Mg=0.38 for 6060\_3 alloy the position of the noses are

$\beta$ -nose at t=4750 sec

$\beta'$ -nose at t=3750 sec

Thus the  $\beta$  and  $\beta'$  noses are displaced by 1000 sec based only on the Mg content of the alloy. The next step is to find the displacement of the  $\beta'$ -nose due to the excess Si in the alloy. The excess Si is the Si remaining in the alloy after subtracting the Si necessary for the formation of  $\text{Mg}_2\text{Si}$  and the Si present in the  $\alpha\text{-AlFeMnSi}$  phase after the  $\beta\text{-AlFeSi} \rightarrow \alpha\text{-AlFeMnSi}$  transformation during homogenization.

The relevant equations are [20]:

$$[\text{Si}]_{\text{xs}} = [\text{Si}]_{\text{alloy}} - [\text{Si}]_{\alpha\text{-AlFeMnSi}} - [\text{Si}]_{\text{Mg}_2\text{Si}} \quad (3)$$

$$[\text{Si}]_{\text{Mg}_2\text{Si}} = [\text{Mg}]_{\text{alloy}} \{A_{\text{Si}}/2A_{\text{Mg}}\} = 0.577 [\text{Mg}]_{\text{alloy}} \quad (4)$$

$$[\text{Si}]_{\alpha\text{-AlFeMnSi}} = [\text{Fe}+\text{Mn}]_{\text{alloy}} \{A_{\text{Si}}/3(A_{\text{Fe}}+A_{\text{Mn}})\} = 0.0664 [\text{Fe}+\text{Mn}]_{\text{alloy}} \quad (5)$$

where A is the atomic weight of the alloying element.

The results are displayed in Table 5.3

| Alloy   | Mg   | Si   | Fe    | Mn   | [Si] <sub>xs</sub> |
|---------|------|------|-------|------|--------------------|
| 6060    | 0.43 | 0.39 | 0.22  | 0.02 | 0.126              |
| 6063    | 0.47 | 0.50 | 0.19  | 0.03 | 0.214              |
| 6005    | 0.57 | 0.68 | 0.20  | 0.11 | 0.330              |
| 6082(L) | 0.61 | 0.69 | 0.196 | 0.45 | 0.295              |
| 6082(H) | 1.05 | 1.23 | 0.20  | 0.65 | 0.567              |
| 6060_3  | 0.38 | 0.47 | 0.2   | 0.03 | 0.288              |

A continuous cooling precipitation model is applied in order to calculate the start time for the precipitation of  $\beta'$ -Mg<sub>2</sub>Si phase. In this work the KWN model was employed.

In order to calculate the shift of the  $\beta'$ -nose the following parameters were considered:

The  $\beta'$ -solvus curve in the phase diagram was displaced by 70°C to lower temperatures relative to the equilibrium  $\beta$  solvus curve.

Because the  $\beta'$ -phase is semicoherent with the Al matrix, the interfacial energy was reduced to  $\gamma=0.3$  J/m<sup>2</sup> relative to  $\gamma=0.5$  J/m<sup>2</sup> for the equilibrium  $\beta$ -phase, which is incoherent.

The effect of excess Si was taken into account with two adjustable parameters in the KWN model. The first parameter, the total number of nucleation sites  $N_0$ , was increased in proportionality with the excess Si in the alloy. For the 6060\_3 model alloy, a value  $2N_0$  was selected, where  $N_0$  is the value considered for the 6060 alloy in Table 5.3. The second parameter, the activation energy, was reduced exponentially with the amount of excess Si. In this way the activation energy for the 6060\_3 model alloy was reduced to the value  $\Delta G_0/7$  relative to the value of  $\Delta G_0$  for 6060 in Table 5.3.

The results are shown in Figure 5.21. The  $\beta'$  'nose' is displaced by 1530 sec and is located at about 2220 sec.

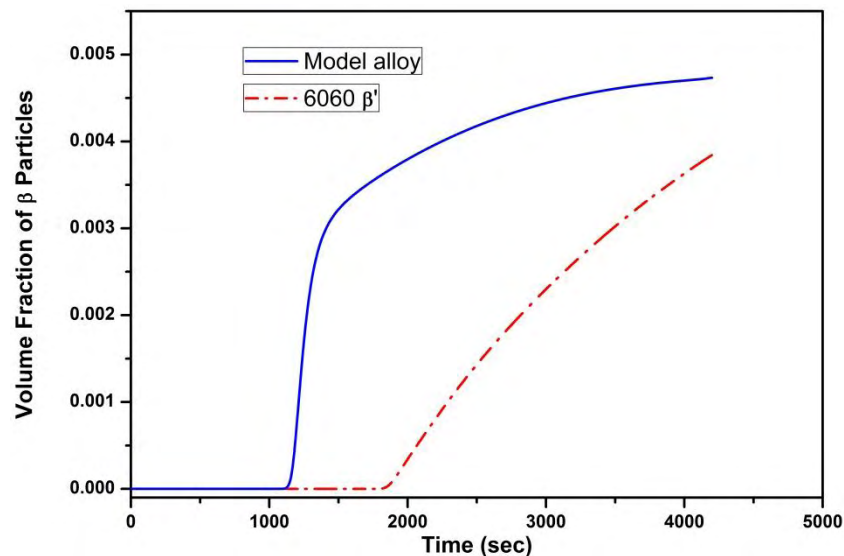


Figure 5.21: Effect of excess Si on the precipitation of  $\beta'$ -Mg<sub>2</sub>Si

The shift in the CCP diagram of the 6060\_3 alloy is shown in Figure 5.22. The dotted  $\beta'$  line is shifted by taking into account only the Mg effect as per equation (2). The full line corresponds to the  $\beta'$ -nose, taking into account the effect of excess Si in the alloy.

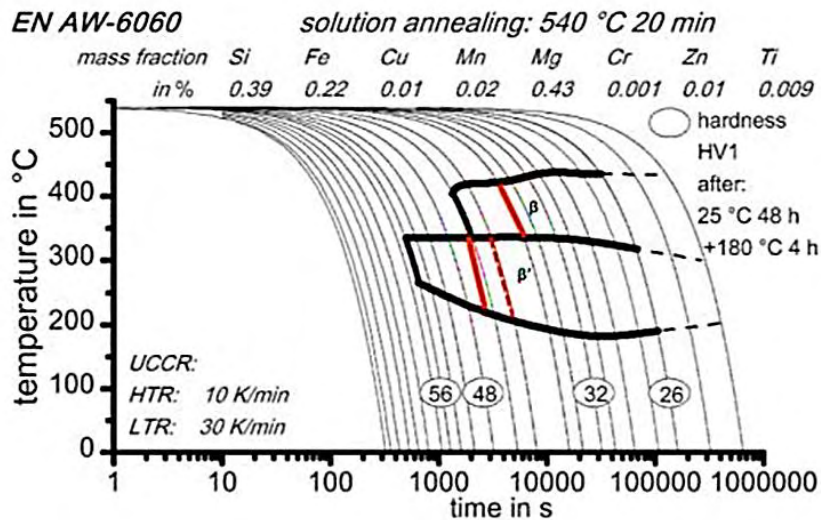


Figure 5.22: CCP diagram of the 6060\_3 alloy (red lines). The dotted  $\beta'$  line is shifted by taking into account only the Mg effect. The  $\beta'$  nose (full line) is shifted by taking into account the effect of excess Si in the 6060\_3 alloy

The resulting CCP diagram can be used for the design of a homogenization cooling program, in order to achieve precipitation of the metastable phase  $\beta'$ -Mg<sub>2</sub>Si.

## 5.5. Design rules for high extrudability

The aim of the present section is to formulate design rules regarding the homogenization practice in order to obtain high extrudability. From the literature and from the results of this thesis, regarding the simulation of solidification and homogenization of 6xxx alloys, the following preliminary remarks can be made:

Extrudability is a complex property, not measurable directly. Extrudability is usually determined at the extrusion shop with several ways, like the maximum extrusion speed accomplished without surface defects or the maximum pressure, or even the contact time in the press. However, since extrudability is a property, it depends on the microstructure, which in turn depends on the composition and the process chain from melt treatment and

alloying down to the extrusion press. All elements of the process chain have an effect on extrudability:

1. melt conditioning, cleaning and alloying,
2. DC casting – development of the as cast microstructure,
3. billet homogenization, involving heating and holding
4. cooling from the homogenization temperature
5. billet preheating at the extrusion shop.

The rest of the process chain is also important because it affects extrudability indirectly. So billet preheating is followed by

6. extrusion,
7. cooling from the extrusion temperature (also solution temperature) and
8. aging for precipitation strengthening.

It appears that from the above list, the most important design rules regarding high extrudability are:

**Melt purity:** It is an important and usually overlooked variable, which influences extrudability and yield in the press shop. It is influenced by the melt conditioning, cleaning and alloying practice for the control of inclusions, hydrogen, alkali metal salts and the desired alloying level.

**As-cast microstructure:** The microstructure developed during DC casting is affected by the solidification conditions. Grain size and DAS are the most important factors. They can be controlled by the casting speed (solidification rate) and seeding for grain refining. A smaller grain size and DAS improves the strength and also shortens the diffusion distances, leading to a more efficient homogenization for a given homogenization cycle. In terms of phase fractions, the results presented in Chapter 2 allowed the mapping of the Mg-Si space for given Fe and Mn contents. Compositions can be selected to minimize the undesirable  $\beta$ -AlFeSi intermetallic in the as-cast microstructure, in order to achieve a good starting point for the homogenization to follow. It was shown that Mn reduces the amount of  $\beta$ -AlFeSi for a given Mg-Si-Fe combination.

**Homogenization process:** The aim of homogenization is to reduce the microsegregation of elements and phases that are concentrated at grain boundaries and interdendritic areas. In 6xxx alloys the undesirable  $\beta$ -AlFesi intermetallic phase, which limits extrudability,

transforms to a more rounded  $\alpha$ -AlFeMnSi intermetallic phase. With the simulations presented in Chapter 3, it is possible to determine the required time for  $\text{Mg}_2\text{Si}$  dissolution and the transformation  $\beta \rightarrow \alpha$ -AlFeSi as a function of homogenization temperature and alloy composition. It was shown that Mn has a beneficial effect on the kinetics of the  $\beta$  to  $\alpha$  transformation. After the transformation  $\beta \rightarrow \alpha$  is complete, the homogenization process continues since the  $\alpha$  phase undergoes coarsening and spheroidization, adopting a necklace morphology. Microstructural indices, such as the aspect ratio and the circularity, were determined in Chapter 4 and can be used to characterize the homogenization stage quantitatively. These parameters can be determined by quantitative metallography (image analysis). A fully homogenized billet, with the potential for high extrudability should have all  $\beta$ -AlFeSi transformed to  $\alpha$ -AlFeSi, with necklace morphology and as aspect ratio and circularity approaching unity. In addition all  $\text{Mg}_2\text{Si}$  should be dissolved and Mg and Si should be distributed as uniformly as possible in the grain interiors.

***Cooling from the homogenization temperature:*** The rate of cooling is important. It appears that a cooling cycle that produces a fine dispersion of  $\beta'$ - $\text{Mg}_2\text{Si}$  is the optimum, because it possesses a lower solvus temperature. Therefore during preheating, the  $\beta'$  will dissolve at a lower temperature, be substituted by a fine dispersion of  $\beta$ - $\text{Mg}_2\text{Si}$ , which will dissolve readily during extrusion. This enables the use of a lower preheating temperature, providing a larger window for temperature rise up to the exit temperature. This means that a higher extrusion speed can be obtained. The cooling program should be designed so that precipitation of  $\beta$ - $\text{Mg}_2\text{Si}$  is avoided and only precipitation of  $\beta'$ - $\text{Mg}_2\text{Si}$  takes place. A CCP diagram like the one developed for the 6060\_alloy in this Chapter can be used to design the cooling cycle.

***Preheating of billet prior to extrusion:*** It is important to match the preheating conditions to the homogenization cooling conditions in order to get the most benefit of homogenization.  $\beta$ - $\text{Mg}_2\text{Si}$  precipitates require higher temperatures to dissolve (higher solvus) and have a detrimental effect on hot ductility. On the other hand the  $\beta'$ - $\text{Mg}_2\text{Si}$  ppts, are finer, semicoherent with the matrix and have a lower solvus temperature. Thus a lower preheating temperature can be employed in combination with a high extrusion speed. This will raise the exit temperature to a value sufficient for complete dissolution of  $\text{Mg}_2\text{Si}$ .

## 5.6. Conclusions

From the results presented in this chapter the following conclusions can be drawn:

- Precipitation during cooling from the homogenization temperature was simulated with the KWN precipitation model. The relevant particle size distribution (PSD), evolution of volume fraction and particle size during cooling were calculated. The results were introduced in a suitable strength model to calculate the resulting hardness. The simulation results are in satisfactory agreement with experimental data. Forced air cooling results in higher hardness in relation to natural cooling for the alloy 6063 investigated.
- The hardening of the homogenized billets was investigated experimentally. Regarding the effect of the homogenization cooling rate, water quenching results in higher hardness relative to air cooling and forced air cooling. The hardness difference increases with alloying in the order 6063→6005→6082. The effect is attributed to the higher amounts of Mg and Si retained in solid solution during cooling.
- Regarding the effect of alloy composition, homogenization temperature, homogenization time and homogenization cooling rate on the hardening potential of the homogenized billets, the alloys water that were quenched from the homogenization temperature exhibited the higher hardening potential relative to the air and forced cooling. In addition, the maximum hardening potential is exhibited for the 8h homogenization time, irrespective of the homogenization temperature.
- For the lower alloyed 6063 and 6005 billets, the hardening potential at shorter homogenization time increase with the homogenization temperature.
- The effect of excess Si on the precipitation of  $\beta'$ -Mg<sub>2</sub>Si was determined using the KWN precipitation model. The resulting shift in the continuous cooling precipitation (CCP) diagram was calculated. This allows the design of a suitable cooling program in order to avoid the precipitation of  $\beta$ -Mg<sub>2</sub>Si and promote the precipitation of  $\beta'$ -Mg<sub>2</sub>Si. This allows the use of a lower preheating temperature prior to extrusion and leads to the use of higher press loads in order to obtain higher extrusion speeds.
- Specific design rules were formulated, regarding the as-cast microstructure, the homogenization temperature and time as well as the cooling from the homogenization temperature in order to obtain high extrudability.

## 5.7. References

- [1].S. Samaras Ph.D Thesis, University of Thessaly, Mech. Eng (2006)
- [2].A. Serafeim, Diploma Thesis, University of Thessaly, Mech. Eng. (2013)
- [3].J.Fanikos, Diploma Thesis, University of Thessaly, Mech. Eng. (*in progress*)
- [4].I. M. Lifshitz, V.V. Slyozov, J.Phys.Chem.Solids, (1961)19:35.
- [5].C. Wagner, Z. Elektrochem., 65 (1961) 581.
- [6].J. S. Langer, A. Schwartz, Physical Review A 21 (1980) 948.
- [7].R. Wagner, R. Kampmann, In Mater. Sci. Techn. Weinheim 5 (1991) 21.
- [8].R. Kampmann, H. Eckerlebe, R. Wagner, Mater. Res. Soc. Symp. Proc., 57 (1987) 52
- [9].A.Tousias, Diploma Thesis, University of Thessaly, Mech. Eng. (2014)
- [10]. O. Reiso, Marter. Forum, 28 (2004) 32-46
- [11].A. Jackson, T. Sheppard, Alum., Assoc., 1 (1998) 1-20.
- [12].Y. Birol, Trans., Nonferrous Met. Soc. China, 23 (2013) 1875-1881
- [13].G. Mrowks-Nowotnik, J. Sieniawski, J. Mater. Proc. Techn. 162-163 (2005) 367-372
- [14].M.A. Abdel-Rahman, Def., Dif., For., 303-304 (2010) 107-112
- [15].S. Zajac, B. Bengtsson, C. Jonsson, Mater. Sci. Forum 396-402 (2002) 399-404
- [16]. H. Zhu, M. Couper, A. Dahle, Jour., Met., 63, No.11 (2011) 66-71.
- [17]. Marioara C.D., Andersen S.J., Stene T.N., Hasting H., Walmsley J., Vanhelvoort A.J., Holmestad R., Philos. Mag. 87 (2007) 3385-341
- [18]. Milkereit B., Wanderka N., Schick C., Kessler O., Mat., Sc., Eng. A 550 (2012) 87-96.
- [19]. Shang B.C., Yin Z.M., Wang G., Liu B., Huang Z.Q., Mat. Des. 32 (2011) 3818-3822
- [20]. Asensio-Lozano J., Suarez-Pena B., Vander Voort G.F., Mat. 7 (2014) 4224-4242



## 6. Conclusions

The results presented in this thesis lead to the following conclusions:

### **Regarding the as-cast microstructures**

- Computational alloy thermodynamics, based on the CALPHAD approach, has been applied to perform Scheil-Gulliver solidification simulations. The resulting microsegregation of elements and phases in the as-cast microstructure were calculated as a function of alloy composition.
- The results of the simulations were confirmed experimentally by quantitative image analysis for the measurement of phase fractions.
- The variation of the mole fractions of the extrudability-limiting  $\beta$ -AlFeSi phase and the strengthening  $\text{Mg}_2\text{Si}$  phase with alloying elements has been mapped over the useful range (0-1.2 mass%) in the Mg-Si composition space.
- The constructed maps indicate that low mole fractions of  $\beta$ -AlFeSi are associated with lower Si and higher Mg compositions. On the other hand, high mole fractions of  $\text{Mg}_2\text{Si}$  are associated with both higher Si and Mg compositions, with Mg possessing a stronger effect.
- Construction of maps for different levels of Mn has shown that addition of Mn could allow for higher alloying with Mg and Si, in order to obtain higher amount of  $\text{Mg}_2\text{Si}$ , without at the same time increasing the  $\beta$ -AlFeSi intermetallic phase in the as-cast microstructure.

### **Regarding the homogenization process**

- The Dual grain model (DGM) has been developed to treat the homogenization process in multicomponent and multiphase Al-alloys exhibiting a large variability of the as-cast grain size. With the model it is possible to simulate the temporal and spatial evolution of phase fractions and element concentration during homogenization.

- Regarding the evolution of phase fractions during homogenization, the predictions of the DGM model have been validated experimentally with XRD analysis. The evolution of the  $\beta\text{-AlFeSi} \rightarrow \alpha\text{-AlFeSi}$  transformation is predicted by the DGM and is confirmed by XRD in the same time scale.
- The DGM predictions regarding the evolution of Fe and Mg concentrations with homogenization time are in excellent agreement. There are only some discrepancies in the profiles of Si and Mn. The Si discrepancy is due to the Si-diamond phase not taken into account in the DGM. The Mn discrepancy is due to the Mn retention in the  $\alpha\text{-AlFeSi}$  phase.
- The DGM predicts the fast dissolution of  $\text{Mg}_2\text{Si}$  during homogenization and its re-precipitation during cooling. It also predicts its dissolution during preheating prior to extrusion.
- The DGM can describe the temporal and spatial evolution of the  $\beta\text{-AlFeSi} \rightarrow \alpha\text{-AlFeSi}$  transformation. The spatial evolution exhibits an exact spatial correspondence. In addition the transformation starts at a certain distance from the boundary and the transformation front moves towards the boundary.
- Both the  $\text{Mg}_2\text{Si}$  dissolution and the  $\beta\text{-AlFeSi} \rightarrow \alpha\text{-AlFeSi}$  transformation are faster in the smaller grain as predicted by the DGM. In addition the concentration profiles of the elements homogenize faster in the smaller grain, indicating that a fine grain size in the as-cast microstructure accelerates the homogenization process.
- The DGM predicts correctly the effect of homogenization temperature. The rate of both the  $\text{Mg}_2\text{Si}$  dissolution and the  $\beta\text{-AlFeSi} \rightarrow \alpha\text{-AlFeSi}$  transformation increase with the homogenization temperature.
- A preliminary attempt to develop homogenization process maps has been performed using the DGM. These maps are, at present, based on  $\text{Mg}_2\text{Si}$  dissolution and the  $\beta\text{-AlFeSi} \rightarrow \alpha\text{-AlFeSi}$  transformation and can be used for the design of the homogenization heat treatment.
- The quantification of the homogenization state was achieved by determine specific microstructural indices, such as the aspect ratio and the circularity of the intermetallic phases. In this way it was possible to quantify the shape evolution of the intermetallic compounds during homogenization.

## Regarding the homogenization cooling

- Precipitation during cooling from the homogenization temperature was simulated with the Kampman-Wagner Numerical (KWN) precipitation model. The relevant particle size distribution (PSD), the evolution of volume fraction and the particle size during cooling were calculated. The results were introduced in a suitable strength model to calculate the resulting hardness. The simulation results are in satisfactory agreement with experimental data. Forced air-cooling resulted in higher hardness in relation to natural cooling for the alloy 6063 investigated.
- The hardness of the homogenized billets was investigated experimentally. Regarding the effect of homogenization cooling rate, water quenching results in higher hardness relative to air cooling and forced air cooling. The hardness difference increases with alloying in the order 6063→6005→6082. The effect is attributed to the higher amounts of Mg and Si retained in solid solution during cooling.
- Regarding the effect of alloy composition, homogenization temperature, homogenization time and homogenization cooling rate on the hardening potential of the homogenized billets, the alloys that were water-quenched from the homogenization temperature exhibited the higher hardening potential relative to the air and forced cooling. In addition, the maximum hardening potential was exhibited for the 8h homogenization time, irrespective of the homogenization temperature.
- The effect of excess Si on the precipitation of  $\beta'$ -Mg<sub>2</sub>Si was determined using the KWN precipitation model. The resulting shift in the continuous cooling precipitation (CCP) diagram was calculated. This allows the design of a suitable cooling program in order to avoid the precipitation of  $\beta$ -Mg<sub>2</sub>Si and allow the precipitation of  $\beta'$ -Mg<sub>2</sub>Si. This allows the use of a lower preheating prior to extrusion and leads to the use of higher press loads in order to obtain higher extrusion speeds.

## Regarding the design rules

- Specific design rules were formulated, regarding the as-cast microstructure, the homogenization temperature and time as well as the cooling from the homogenization temperature in order to obtain high extrudability.
- The microstructure developed during DC casting is affected by the solidification conditions. Grain size and dendrite arm spacing (DAS) are the most important factors. They can be controlled by the casting speed (solidification rate) and seeding for grain refining. A smaller grain size and DAS improves the strength and also shortens the diffusion distances, leading to a more efficient homogenization for a given homogenization cycle.
- Phase fraction mapping, developed in Chapter 2, can be used for the selection of alloy compositions to minimize the undesirable  $\beta$ -AlFeSi intermetallic in the as-cast microstructure, in order to achieve a good starting point for the homogenization to follow. In addition, it has been shown that Mn reduces the amount of  $\beta$ -AlFeSi for a given Mg-Si-Fe combination.
- With the DGM model presented in Chapter 3, it is possible to determine the required time for  $\text{Mg}_2\text{Si}$  dissolution and the transformation  $\beta \rightarrow \alpha$ -AlFeSi as a function of homogenization temperature and alloy composition. It has also been shown that Mn has a beneficial effect on the kinetics of the  $\beta$  to  $\alpha$  transformation. The DGM model also indicated that a small as-cast grain size accelerates the kinetics of homogenization, a point that was indicated above.
- Microstructural indices, such as the aspect ratio and the circularity, were determined in Chapter 4 and can be used to characterize the homogenization stage quantitatively. A fully homogenized billet, with the potential for high extrudability should have all  $\beta$ -AlFeSi transformed to  $\alpha$ -AlFeSi, with necklace morphology and with aspect ratio and circularity approaching unity. In addition all  $\text{Mg}_2\text{Si}$  should be dissolved and Mg and Si should be distributed as uniformly as possible in the grain interiors.

- The cooling from the homogenization temperature should be designed so that precipitation of  $\beta$ -Mg<sub>2</sub>Si is avoided and only precipitation of  $\beta'$ -Mg<sub>2</sub>Si takes place. A CCP diagram like the one developed for a 6060 alloy in this Chapter 5 can be used to design the cooling cycle.
- It is important to match the preheating conditions to the homogenization cooling conditions in order to get the most benefit of homogenization.  $\beta$ -Mg<sub>2</sub>Si precipitates require higher temperatures to dissolve (higher solvus) and have a detrimental effect on hot ductility. On the other hand the  $\beta'$ -Mg<sub>2</sub>Si ppts, are finer, semi – coherent with the matrix and have a lower solvus temperature. Thus a lower preheating temperature can be employed in combination with a high extrusion speed. This will raise the exit temperature to a value sufficient for complete dissolution of Mg<sub>2</sub>Si.



## 7. Proposal for further research

The present thesis provided answers to specific questions and methodologies towards the computationally-based design of extrudable Al-alloys. However, as it was expected, new questions and new research topics were generated. Some of these topics are outlined below:

### **Model integration**

While the simulation of microsegregation has been linked to the DGM, the precipitation during homogenization cooling is an independent simulation based on the KWN model. It is proposed to link this model to the DGM in the sense that the results of the DGM can be used as a direct input to the KWN model. A Matlab code could be written to perform this task. In this way it would be possible to link also the preheating prior to extrusion; so that all parts of the process chain prior to extrusion can be integrated. This will increase the level of model integration and provide an easier-to-handle computational tool for design purposes.

### **Homogenization cooling**

In this thesis the KWN model was used to simulate the precipitation during homogenization cooling. The current version of the model handles only one set of precipitates in binary systems (matrix-precipitate) as in the Al-Mg<sub>2</sub>Si system. Furthermore only equilibrium phases are considered. It is proposed to investigate the application of the new software TC-Prisma, which is based on the KWN model, but additionally relies on the thermodynamic and kinetic databases of Thermo-Calc and Dictra. The new versions of Thermo-Calc provide values for the interfacial energies and contain data for metastable phases, making it possible in the near future to simulate precipitation of metastable or transition phases, such as the  $\beta'$ -Mg<sub>2</sub>Si.

## DGM model

The DGM for homogenization can be further refined through parametric simulation studies such as (a) looking at different geometries (spherical or cylindrical), (b) simulating different grain sizes, (c) taking into account increased diffusivities due to high dislocation density. In addition the effect of composition such as the effect of Mn or other alloying elements on the  $\alpha$ -AlFeSi $\rightarrow\beta$ -AlFeSi transformation could be investigated.

## Homogenization Process Maps

A preliminary attempt to generate a homogenization process map was presented in this thesis based on the time for the completion of the  $\alpha$ -AlFeSi $\rightarrow\beta$ -AlFeSi transformation. These maps should be extended for other alloy compositions (with different Fe and Mn contents), in order to generate a master process map for the homogenization of 6xxx alloys.

## Shape change during homogenization

It appears that in addition to the Mg<sub>2</sub>Si dissolution and the  $\alpha$ -AlFeSi $\rightarrow\beta$ -AlFeSi transformation, a third transformation regarding the shape change of the  $\alpha$ -AlFeSi phase takes place during homogenization. This transformation has three stages (a) edge rounding, (b) particle pinching and (c) neckless formation and spheroidization.

A model describing the shape evolution of the  $\alpha$ -AlFeSi should be developed and linked to the DGM in order to generate a complete homogenization model for 6xxx alloys.

## Extrusion and aging

A next step to process integration is the link of the homogenization model with available or to-be-developed models for hot extrusion based on the finite element method. Extrusion is a deformation process carried out under high deformation rates at high temperatures. Several metallurgical phenomena, such as recovery, recrystallization, phase



dissolution and reprecipitation take place concurrently during the extrusion process. The material after extrusion is subjected to the final aging treatment for precipitation strengthening. The simulation of extrusion and aging combining mechanics and metallurgy seems to be a good research topic, which will allow the complete process integration and, therefore, the full scale computational design of extrudable Al-alloys.



## Publications by the author

---

1. P.I. Sarafoglou and G.N. Haidemenopoulos, *Phase Fraction Mapping in the As-Cast Microstructure of Extrudable 6xxx Aluminum Alloys*, Int. Journal of Materials Research 105, No.12, pp. 1202-1208 (2014).
2. G.N. Haidemenopoulos and P.I. Sarafoglou, Extrudable Al-alloys: microsegregation and homogenization, to appear in the Encyclopedia of Aluminum Alloys, Taylor and Francis, NY, (*invited paper, under preparation*)
3. P.I. Sarafoglou, I. Aristeidakis, M. Tzini and G.N. Haidemenopoulos, *Index-based quantification of the homogenization state in extrudable Al-alloys*, To be submitted in Metals, 2016 (*under preparation*)
4. P.I. Sarafoglou and G.N. Haidemenopoulos, *Simulation of the microsegregation and homogenization, including hardening during homogenization cooling, of the 6082 Al-alloy*, to be submitted in Materials Science and Engineering A, 2016 (*under preparation*)
5. P.I. Sarafoglou and G.N. Haidemenopoulos, *On the computational-based design of 6xxx series extrudable Al-alloys*, MSE Conference, Darmstadt, Germany, 23-25 September 2014.
6. P.I. Sarafoglou and G.N. Haidemenopoulos, Design of 6xxx alloys: Control of intermetallic phases in the as-cast microstructure, 5<sup>th</sup> Hellenic Conference on Metallic Materials, Volos, 2013
7. Maria-Ioanna Tzini, Panagiota Sarafoglou, Andreas Stieben, Gregory Haidemenopoulos, Wolfgang Bleck, *Austenite evolution and solute partitioning during thermal cycling in the intercritical range of a medium-Mn steel*, Junior Euromat, 10-16 July, 2016, Lausanne, Switzerland

In addition to the publications based on the thesis the following publications were concluded:

1. L.A. Spyrou, P.I. Sarafoglou, N. Aravas and G.N. Haidemenopoulos, *Evaluation of Creep Damage of INCOLOY 800HT Pigtailes in a Refinery Steam Reformer Unit*, Engineering Failure Analysis 45, pp. 456-469 (2014).
2. P.I. Sarafoglou, M.I.T. Tzini and G.N. Haidemenopoulos, *Simulation of cyclic transformations in the intercritical range of a 5Mn steel*, Int. Journal of Materials and Metallurgical Engineering, 1 (104) 2015 DOI:18:15344/IJMME/2015/104
3. G.N. Haidemenopoulos, P. I. Sarafoglou, P. Christopoulos and A.D. Zervaki, *Metallurgical Study of Initiation and Propagation of RCF cracks in Rails*, ICEAF IV, Skiathos 24-26 June, 2015
4. P.I. Sarafoglou, M.I.T. Tzini and G.N. Haidemenopoulos, *Simulation of cyclic transformations on a 0.2C-5Mn steel*, ICEAF IV, Skiathos 24-26 June, 2015
5. G.N. Haidemenopoulos, P.I. Sarafoglou, P. Christopoulos, A. Zervaki, *Rolling Contact fatigue cracking in rails subjected to in-service loading*, Fatigue and Fracture of Engineering Materials and Structures, 2016